



Durham E-Theses

Long-term observations of terminus position change, structural glaciology and velocity at Ninnis Glacier, George V Land, East Antarctica (1963-2021)

CLAYTON, Harry, Alexander-Bartlett

How to cite:

CLAYTON, Harry, Alexander-Bartlett (2022) *Long-term observations of terminus position change, structural glaciology and velocity at Ninnis Glacier, George V Land, East Antarctica (1963-2021)*, Durham theses, Durham University. Available at Durham E-Theses Online: <http://etheses.dur.ac.uk/14622/>

Use policy

The full-text may be used and/or reproduced, and given to third parties in any format or medium, without prior permission or charge, for personal research or study, educational, or not-for-profit purposes provided that:

- a full bibliographic reference is made to the original source
- a [link](#) is made to the metadata record in Durham E-Theses
- the full-text is not changed in any way

The full-text must not be sold in any format or medium without the formal permission of the copyright holders.

Please consult the [full Durham E-Theses policy](#) for further details.

Harry Alexander Bartlett Clayton

Long-term observations of terminus position change, structural glaciology and velocity at Ninnis Glacier, George V Land, East Antarctica (1963-2021)

Over the last four decades, some major East Antarctic outlet glaciers have undergone rates of retreat, thinning and acceleration in response to ocean-climatic forcing. However, some major East Antarctic outlet glaciers remain unstudied in the recent past. Ninnis Glacier is one East Antarctic outlet glacier that is potentially vulnerable to future ocean-climate change and requires monitoring. This thesis quantifies and analyses long-term (1963-2021) changes in terminus position, structural glaciology and velocity at Ninnis Glacier. The results of this study show that Ninnis underwent three major calving events (in 1972-1974, 1998 and 2018), characterised by a 20–25-year periodicity and indicative of a naturally occurring cycle. Each respective calving event created a large-scale tabular iceberg and formed a new terminus position at similar locations up-ice relative to Ninnis' 1992 grounding line position. The major calving events in 1998 and 2018 were controlled by the development of a central rift system that appears in the same location on Ninnis' tongue, reinforcing the notion of a predictable calving cycle. Ice flow velocity trends before the 2018 calving event (2017-2018) revealed no discernible change in velocity immediately up-ice (+0.2 %) and down-ice (>0 %) of the 1992 grounding line, suggesting that rifting took place within a 'passive' sector of Ninnis' ice tongue. Between 2018 and 2021, Ninnis underwent a pervasive deceleration up-ice (-2.1 %) and down-ice (-1.4 %) of the 1992 grounding line and on the distal ice tongue (-18.7 %). This indicated that the 2018 calving event did not result in the loss of dynamically important ice. Although Ninnis has previously been deemed a sector at risk of retreat, it is concluded that Ninnis is not currently undergoing Marine Ice Sheet Instability and is not currently sensitive to external forcing. This is consistent with low basal melt rates, negligible grounding line retreat and low thermal forcing temperatures in the coastal waters observed at Ninnis.

**LONG-TERM OBSERVATIONS OF
TERMINUS POSITION CHANGE,
STRUCTURAL GLACIOLOGY
AND VELOCITY AT NINNIS GLACIER,
GEORGE V LAND, EAST ANTARCTICA
(1963-2021)**

Harry Alexander Bartlett Clayton

Thesis submitted for MSc by Research degree

Department of Geography

Durham University

April 2022

Table of Contents

List of Tables.....	vi
List of Figures	vii
Statement of Copyright	x
Acknowledgments.....	xi
Chapter 1: Introduction.....	1
1.1. Recent changes of the Antarctic Ice Sheet.....	1
1.2. Introduction to the East Antarctic Ice Sheet (EAIS)	2
1.3. Past glaciological changes of the East Antarctic Ice Sheet (EAIS)	3
1.4. Instability of East Antarctic outlet glaciers.....	4
1.5. Aims and objectives	5
1.5.1 Aim.....	5
1.5.2. Objectives	5
1.6. Study site: Ninnis Glacier.....	6
1.7. Thesis structure	10
Chapter 2: A review of recent East Antarctic Ice Sheet change	11
2.1. Current estimates of Antarctic mass balance	11
2.2. Mass balance of the East Antarctic Ice Sheet (EAIS) since 1992	13
2.3. Regional changes in the East Antarctic mass budget	17
2.4. Elucidating the drivers of East Antarctic outlet glacier change	19
2.4.1. Introduction	19
2.4.2. Ocean drivers of Antarctic glacier change	19
2.4.3. Decadal observations of widespread EAIS outlet glacier change.....	20
2.4.5. Observations of potentially unstable East Antarctic Outlet Glaciers	25
2.5. A review of previous work on Ninnis Glacier.....	30
Chapter 3: Methods	35
3.1. Introduction	35
3.2. Image acquisition	35
3.2.1. Satellite data sources.....	35
3.2.2. Satellite data processing and geocorrection	38
3.2.3. Error quantification for geocorrected images	38
3.3. Terminus position change at Ninnis Glacier	39

3.3.1. Terminus digitisation	39
3.3.2. Sub-annual terminus position change.....	41
3.3.3. Terminus digitisation error quantification	42
3.4. Structural glaciological mapping	42
3.5. Velocity mapping.....	48
3.6. Bed topography, ice surface elevation and grounding line datasets	51
Chapter 4: Results	52
4.1. Introduction	52
4.2. Terminus position change.....	52
4.2.1 Terminus position change (1963-1998)	56
4.2.2 Terminus position change (2000-2018)	58
4.2.3 Sub-annual terminus position change (2018-2021)	62
4.3. Structural Glaciology	64
4.3.1. Structural evolution of Ninnis Glacier (pre-1998 calving event).....	64
4.3.2. Structural evolution of Ninnis Glacier (pre and post 2018 calving event)	66
4.3.3. Extent and distribution of sea ice offshore of Ninnis Glacier (2016-2020).....	72
4.4. Ice velocity measurements	73
4.4.1. MEaSURES annual velocity changes (2006-2011).....	73
4.4.2. ITS_LIVE annual velocity changes (2013-2018).....	77
4.4.3. Sentinel-2 sub-annual velocity mosaics (2018-2021)	79
Chapter 5: Discussion.....	84
5.1. The timing of major calving events at Ninnis Glacier.....	84
5.1.1. Revising the purported 1980-1982 calving event.....	84
5.1.2. Extrapolating Ninnis' maximum position prior to the early 1970s calving event ..	86
5.1.3. Revising the purported January 2000 calving event	86
5.2. A periodic calving cycle at Ninnis.....	87
5.3. The significance of structural glaciological changes at Ninnis Glacier	92
5.3.1. Linking structural glaciology to the 1998 and 2018 calving events	92
5.3.2. Causes of rifting and calving at Ninnis Glacier	94
5.3.3. Controls on the timing of rifting and calving at Ninnis Glacier.....	95
5.4. Linking velocity fluctuations to calving at Ninnis	95

5.4.1. The 2008 minor break-up event.....	95
5.4.2. Velocities before (2013-2018) and after (2018-2021) the 2018 calving event	97
5.5. A review of recent observations of Ninnis Glacier by Cheng et al. (2021).....	98
5.6. Limitations.....	102
5.6.1. Availability of satellite imagery (1963-1984).	102
5.6.2. Structural glaciological analysis of the second calving cycle.	102
5.6.3. Secondary datasets.	103
5.7. Further research.	103
5.7.1. Strain rates.....	103
5.7.2. Grounding line data.....	103
5.7.3. Sea ice	104
5.7.4. Ocean circulation	104
5.7.5. Numerical Modelling	104
Chapter 6: Conclusions	105
References	107
Appendix A: Satellite Image IDs.....	119

List of Tables

2.1	Review of selected multi-method/year estimates of EAIS mass balance (Gt a^{-1})	15
3.1	Overview of satellite and aerial image sources of Ninnis Glacier	36
3.2	Displacement errors (m) for geocorrected images of Ninnis Glacier	39
3.3	Structural glaciology and spatial mapping criteria	44
4.1	Cumulative ice front (re-)advance rates (km a^{-1}) (1963-2021)	55
4.2	Sub-annual cumulative ice front (re-)advance rates (km a^{-1}) (2018-2021)	62
4.3	Summary of mean velocities (m a^{-1}) (2006-2011) (Flowline 1)	76
4.4	Summary of mean velocities (m a^{-1}) (2006-2011) (Flowline 2)	76
4.5	Summary of mean velocities (m a^{-1}) (2013-2018)	78
4.6	Summary of mean monthly velocities (m a^{-1}) (Jan 2018-Jun 2021)	82
4.7	Summary of mean velocities (m a^{-1}) (2018-2021)	82

List of Figures

1.1	Antarctic ice shelf thickness changes (2003-2008) (from Pritchard et al., 2012)	1
1.2	Schematic diagram of Marine Ice Sheet Instability (MISI) (from Pattyn and Morlighem, 2020)	4
1.3	Map of George V Land coastline and Ninnis Glacier	7
1.4	Bathymetric map of the George V Land coastline (from Miles et al. (2018)	8
1.5	Bedrock topography, surface elevation and ice thickness at Ninnis Glacier	9
2.1	Antarctic ice sheet cumulative mass change (Gt) and sea-level contribution (mm) (1992 and 2016) (from the IMBIE Team, 2018)	11
2.2	Outlet glacier grounding line retreat in the Amundsen Sea sector of the WAIS (a) (from Rignot et al., 2014) and glacier area changes across the western Antarctic Peninsula Ice Sheet (b) (from Cook et al., 2016)	12
2.3	Review of pre-2012 (a) and 2012 (b) Antarctic mass balance estimates (Gt a^{-1}) (from Hanna et al., 2013)	14
2.4	Time-series of Antarctic mass balance (1992 and 2016) (from Bamber et al. 2018)	14
2.5	Time series of Antarctic mass balance (1979 and 2017) (from Rignot et al., 2019)	16
2.6	Time series of West Antarctic and East Antarctic mass balance (1979 and 2017) (from Rignot et al., 2019)	17
2.7	Magnitudes of Antarctic mass loss (2003 and 2019) (from Smith et al., 2020)	18
2.8	Temporal variations in terminus position change across the EAIS (1974-2010) (from Miles et al., 2013)	21
2.9	Calving cycle reconstructions across Porpoise Bay (from Miles et al. 2017)	23
2.10	Sea-ice concentrations near the Voyeykov Ice Shelf (from Arthur et al., 2021)	24
2.11	Bed Machine map of Antarctic bed elevation (from Morlighem et al., 2020)	25
2.12	Bathymetric profile for the newly discovered cavity below the Totten Shelf (from Greenbaum et al., 2015)	26
2.13	Mapped changes in terminus position for the Cook East Ice Shelf (a) and Cook West Ice Shelf (b) (1947-2016) (from Miles et al., 2018)	28
2.14	Ice flow model experiments on the Denman Ice Tongue (from Miles et al., 2021)	29
2.15	Topographical map of the Wilkes Subglacial Basin (WSB) (from Mengel and Levermann, 2014)	30

2.16	Terminus position change and Mertz and Ninnis Glacier tongues (1912-1993) (from Wendler et al., 1996)	31
2.17	Terminus position change and iceberg variations at Mertz and Ninnis Glacier (from Frezzotti et al., 1998)	32
2.18	Bathymetric map of George V Land (from Massom, 2003)	33
3.1	Satellite and aerial images used for delineating terminus position change	37
3.2	Terminus position digitised in GEEDiT	40
3.3	Mapped example of the single centreline method	41
3.4	Mapped example of digitised flowlines used for velocity extraction	50
4.1	Terminus position change for Ninnis Glacier (1963 and 1998) (a) and Terminus position change for Ninnis Glacier (2000-2021)	53
4.2	Time series of cumulative terminus position change (km) for Ninnis Glacier (1963 and 2021)	52
4.3	1974 Landsat MSS image depicting the Western Shear Zone and delineated Terminus position in 1974	56
4.4	Extrapolated early 1970s (1973) terminus position from the 1974 Landsat image	57
4.5	Map visualising the June 1998 calving event	58
4.6	Map visualising the small-scale 2004-2008 calving event	60
4.7	Map visualising the January 27 th 2018 calving event	59
4.8	Visualised terminus re-advance at Ninnis Glacier (2018-2021)	63
4.9	Cumulative terminus position change (m) for Ninnis Glacier (2018-2021)	64
4.10	Maps depicting Ninnis Glacier's central rift system (1989-1997)	65
4.11	Structural Glaciology and spatial maps of Ninnis Glacier (2016-2020)	68
4.12	Maps depicting Ninnis Glacier's central rift system (2016-2018)	71
4.13	Time-series of annual velocity changes (2006-2011) at Ninnis Glacier extracted from Flowline 1	73
4.14	Time-series of annual velocity changes (2006- 2011) at Ninnis Glacier extracted from Flowline 2	74
4.15	Maps of annual velocity (m a^{-1}) at Ninnis Glacier (2006-2011)	75

4.16	Time-series of annual velocity changes (2013-2018) at Ninnis Glacier extracted from Flowline 1	77
4.17	Maps of annual velocity (m a^{-1}) at Ninnis Glacier (2013-2018)	79
4.18	Time-series of monthly velocity changes (2018-2021) at Ninnis Glacier extracted from Flowline 1	81
4.19	Maps of annual velocity (m a^{-1}) at Ninnis Glacier (2018-2021)	83
5.1	Map of the delineated 1974 terminus position within the Western Shear Zone	85
5.2	Map depicting the size comparison of tabular icebergs formed from Ninnis Glacier	88
5.3	Map depicting tabular iceberg migration (2019-2021)	90
5.4	Time-series of area change at Ninnis Glacier (1963-2021) (from Cheng et al., 2021)	99
5.5	Comparison of terminus position time series at Ninnis Glacier (1963-2021) between Cheng et al. (2021) and this thesis	100

Statement of Copyright

The copyright of this thesis rests with the author. No quotation from it should be published without the author's prior written consent and information derived from it should be acknowledged.

Acknowledgments

Firstly, I would like to sincerely thank my supervisors Professor Chris Stokes and Professor Stewart Jamieson for their continued support and patience with me during what has been a difficult year, or so. Chris and Stew - I consider myself extremely lucky to have worked with you both. Thank you for everything.

I would also like thank Dr. Bertie Miles for kindly processing the Sentinel velocity mosaics and for contributing to project discussions, Dr. Jenny Arthur for sharing her expertise throughout the project and Professor Massimo Frezzotti for kindly providing imagery.

A special mention must also go to my friends in Durham, especially James, Ellie, Thale and Nacho. My time in Durham would have been nowhere near as fun without them. I also want to say a massive thank you to Holly for her endless support and encouragement over the last six months. To my Mum, Dad and brother, Tom, thank you for everything you have done for me throughout my masters. I would not have made it this far without your love and support.

Finally, I want to dedicate this thesis to my Granny who was always with me, and continues to be with me, through good times and bad.

Chapter 1: Introduction

1.1. Recent changes of the Antarctic Ice Sheet

The latest reconciled estimate of Antarctic Ice Sheet mass balance indicates that it lost $2,720 \pm 1,390$ Gt of ice between 1992 and 2016, equivalent to 7.6 ± 3.9 mm of global mean sea-level rise (SLR) (The IMBIE Team, 2018). The IPCC are now *virtually certain* that cumulative mass loss emanates predominantly from the peripheral outlet glaciers of the West Antarctic Ice Sheet (WAIS) and the Antarctic Peninsula Ice Sheet (APIS) (Meredith et al., 2019). This is based on observational evidence of ice thinning, increases in ice velocity and ice discharge across the two ice sheets (Figure 1.1) (Pritchard et al., 2009; 2012; Rignot et al., 2011; 2019; Smith et al., 2020). The largest signals of ice mass loss derive from the Amundsen Sea sector of the WAIS (Milillo et al. 2019), where persistent oceanic warming over the last four decades has facilitated large-scale basal melt, calving and retreat of its major ice shelves and outlet glaciers (Pritchard et al., 2012; Rignot et al., 2013). Ice shelves play an important role in exerting back-stresses on grounded ice in a process called ‘ice shelf buttressing’ (Rignot et al., 2004; Scambos et al., 2004). However, the loss or weakening of buttressing can trigger positive feedbacks of grounding line retreat and accelerated discharge of inland ice which directly contributes to SLR (Rignot et al., 2014; Alley et al., 2016; Konrad et al., 2018).

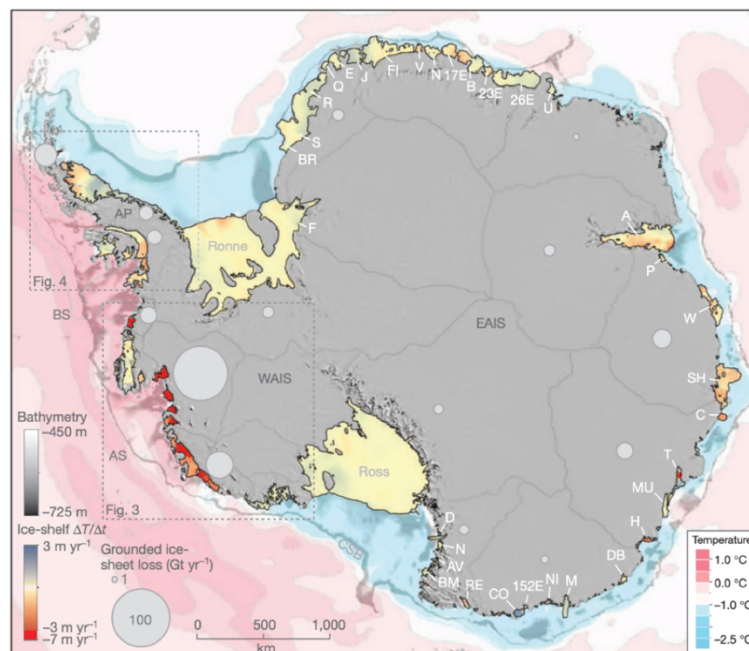


Figure 1.1: Map of Antarctica depicting ice shelf thickness changes between 2003 and 2008 derived from ICESat laser altimetry. Note the extensive rates of thinning of major WAIS outlet glaciers and ice shelves, and at Totten Glacier (T), Moscow Glacier (MU) and Holmes Glacier (H) in the EAIS (from Pritchard et al., 2012).

Roughly 90 % of Antarctica's ice sheet flow is modulated by floating ice shelves and ice tongues which are currently undergoing the largest signals of mass loss in Antarctica via increasing rates of basal melting (Depoorter et al., 2013; Fürst et al., 2016; Miles et al., 2016; Reese et al., 2018). Passive microwave satellite observations have also revealed surface melt on some major Antarctic ice shelves, which is an increasingly important component of Antarctica's mass budget in response to rising atmospheric temperatures and may also lead to future structural instability of outlet glaciers (Johnson et al., 2021).

1.2. Introduction to the East Antarctic Ice Sheet (EAIS)

Recent mass balance estimates for the WAIS and APIS are currently well constrained, yet uncertainties in Antarctica's overall mass balance remain large owing to the lack of consensus on the past and current state of the East Antarctic Ice Sheet (EAIS) (Meredith et al., 2019). The EAIS is the largest of Antarctica's three constituent ice sheets with a total sea-level equivalent (SLE) of 53 m (Fretwell et al., 2013), and its mass balance is thought to be either in equilibrium or slightly gaining mass (The IMBIE Team, 2018; Bamber et al., 2018). Indeed, the EAIS has received significantly less attention compared to regions of West Antarctica that are losing mass, with the magnitude of mass balance estimates varying considerably according to different methods (Rignot et al., 2008; Zwally et al., 2011; Shepherd et al., 2012; King et al., 2012).

The lack of consensus on EAIS mass balance, with some figures yielding uncertainties larger than their respective signals, is due to large observational gaps in accumulation and ice discharge from major EAIS outlet glaciers (Velicogna et al., 2014; Martin-Español et al., 2017). Updated regional-scale remote sensing observations for major outlet glaciers are essential if these uncertainties are to be reduced in the future (Rignot et al., 2019). Target glaciers include those with catchment areas containing large volumes of ice that can raise mean global sea level via increased mass discharge (Rignot et al., 2019).

Recent observations of EAIS outlet glaciers revealed thinning, acceleration, terminus retreat and inland grounding line migration within the Wilkes Land sector (Rignot et al., 2011; Miles et al., 2013; 2016; Greenbaum et al., 2015; Brancato et al., 2020; Smith et al., 2020). One of East Antarctica's largest outlet glaciers, Totten Glacier (3.9 m SLE), lost an estimated $74.4 \pm 2.6 \text{ Gt a}^{-1}$ of ice between 2009 and 2017 via basal melt on the thick portion of its floating ice shelf (Pritchard et al., 2012; Gwyther et al., 2014; Rignot et al., 2019). Denman Glacier (1.5 m SLE) also lost an estimated $59.2 \pm 4.2 \text{ Gt a}^{-1}$ of ice between 2009 and 2017, whilst undergoing grounding line retreat and acceleration in response to the unpinning of its ice tongue (Rignot et al., 2019; Brancato et al., 2020; Miles et al., 2021). Moscow University Glacier (1.3 m SLE)

has also experienced high surface melt rates at its grounding line (Rignot et al., 2013). These are significant observations due to the active role of Wilkes Land's outlet glaciers in draining the Aurora Subglacial Basin (ASB), which contains an SLE of 3.5 m (Young et al., 2011; Greenbaum et al., 2015).

Similar trends were also detected at Cook Glacier in George V Land, which accelerated following collapse of its ice shelf sometime in the 1970s and 1980s (Miles et al., 2018). This was speculated to have occurred via regional oceanic forcing (Miles et al., 2018). Cook is among the largest of EAIS outlets, draining the Wilkes Subglacial Basin (WSB) which, like the ASB, holds a multimeter (3-4 m) mean global SLE (Fretwell et al., 2013; Mengel and Levermann, 2014). However, many major East Antarctic outlet glaciers have been overlooked and require observations detailing changes in terminus position and velocity. This includes the glaciers of Vincennes Bay (66 cm SLE) and Shirase Glacier (118 cm SLE) in Queen Maud Land and Ninnis Glacier (95 cm SLE) in George V Land (Rignot et al., 2019), the latter of which this thesis focusses on.

1.3. Past glaciological changes of the East Antarctic Ice Sheet (EAIS)

Evidence of retreat, thinning and acceleration within some sectors of the EAIS has raised concerns about potentially high future contributions to global mean SLR, particularly from outlet glaciers draining deeply grounded drainage basins such as the ASB and the WSB (Golledge et al., 2015; DeConto and Pollard, 2016; Morlighem et al., 2020; DeConto et al., 2021). Palaeo-Ice Sheet reconstructions and numerical modelling of past warm periods, analogous to current and future atmospheric warming scenarios, revealed that ice mass loss from EAIS drainage basins contributed to multi-meter global mean SLR (Cook et al., 2013; Aitken et al., 2016; Wilson et al., 2018). Importantly, three-dimensional Ice Sheet-ice shelf simulations have also revealed varied responses in global mean SLR under different forcing scenarios (DeConto and Pollard, 2016). Simulations parameterising a 2°C and 400 p.p.m Pliocene scenario led to an 11.3 m SLR contribution from the deepest WAIS and EAIS drainage basins (DeConto and Pollard, 2016). In contrast, simulations applying the RCP.4.5 warming scenarios of the IPCC resulted in a projected 5 m of global mean SLR by 2500 in response to retreat of outlet glaciers draining the WSB and ASB (DeConto and Pollard, 2016). In other studies simulations following a high-emissions (RCP.8.5) scenario project that ice mass loss by 2100 CE will predominantly emanate from the Recovery Subglacial Basin (Golledge et al., 2017) This is due to its sensitivity to ocean temperature anomalies in the eastern Weddell Sea sector, whereas global SLR contributions projected for the WSB and

ASB are significantly lower because they respond predominantly to atmospheric temperatures (Mengel and Levermann, 2014; Sutter et al., 2020).

1.4. Instability of East Antarctic outlet glaciers

Surveys of Antarctica's subglacial landscape have revealed that the grounding lines of some major EAIS outlet glaciers are positioned atop or near reverse-facing (retrograde) slopes (Morlighem et al., 2020). Due to the buttressing force that ice shelves and ice tongues exert on grounded ice inland, thinning and terminus retreat of floating ice towards reverse-facing embayments can reduce their capability of restraining ice flow from the inland ice sheet (Pritchard et al., 2012; Fürst et al., 2014). This increases their susceptibility to Marine Ice Sheet Instability (MISI), a positive feedback loop characterised by enhanced ice mass loss, thinning, grounding line retreat and sea-level rise because of the strong relationship between water depth and ice discharge (Figure 1.2) (Weertman, 1974; Schoof, 2007; Fürst et al., 2014; Pattyn and Morlighem, 2020).

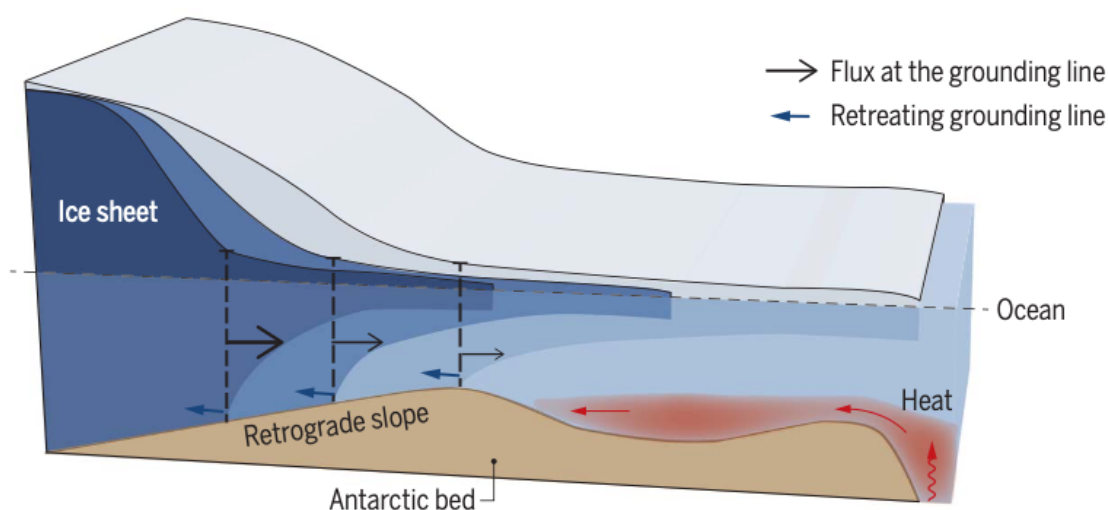


Figure 1.2: Schematic diagram of Marine Ice Sheet Instability (MISI) (from Pattyn and Morlighem, 2020).

Thwaites and Pine Island Glaciers in the Amundsen Sea sector of West Antarctica are thought to be susceptible to future MISI if wide-spread and rapid ice shelf thinning persists (Favier et al., 2014; Mouginit et al., 2014) and some have argued it is potentially already underway at Thwaites (Joughin et al. 2014). However, some major East Antarctic outlet glaciers that both lie on retrograde slopes and actively drain large subglacial basins have remained largely unstudied over the past two decades. Ninnis Glacier is one such example, characterised by

its large catchment actively draining the WSB and its grounding line positioning atop a retrograde slope (Mengel and Levermann, 2014; Morlighem et al., 2020). This poses questions as to its potential susceptibility to future MISI (Pattyn and Morlighem, 2020).

Ninnis has remained largely unstudied since 2003, with previous observations denoting a naturally occurring calving cycle (Frezzotti et al, 1998; Massom, 2003). Given the recent observations of EAIS outlet glacier change over the past four decades (Miles et al., 2013; Lovell et al., 2016), Ninnis requires updated observations to potentially uncover recent changes in its behaviour and assess their impact (Rignot et al., 2019). This thesis presents a new observational study of Ninnis Glacier motivated by the lack of recent work, prompting a series of important aims and objectives.

1.5. Aims and objectives

1.5.1 Aim

This study aims to quantify terminus position change, structural glaciology and velocity changes of Ninnis Glacier, George V Land, East Antarctica, and elucidate the driving mechanisms behind any recent changes.

1.5.2. Objectives

1. Obtain cloud-free aerial imagery from Landsat 1-8 and Sentinel 2 alongside a range of Synthetic Aperture Radar (SAR) satellite images (e.g., JERS-1, ERS-1 and ERS-2) to quantify terminus position change for Ninnis Glacier.
2. To record changes in ice frontal position (e.g., advance, retreat and calving events) and associated changes in glacier surface structures and surrounding spatial features (e.g., rifts, crevasses and sea ice) using cloud-free imagery.
3. Investigate ice flow velocity changes at Ninnis Glacier from 2006 to 2021 through analysis of annual MEaSURES, (e.g., Rignot et al., 2011), ITS_LIVE (e.g., Gardner et al., 2019) and Sentinel-2 sub-annual velocity mosaics.

1.6. Study site: Ninnis Glacier

Ninnis Glacier (68° 22' S 147° E) is a major outlet glacier in George V Land, East Antarctica, positioned between Mertz Glacier to the west and Cook Glacier to the east (Figure 1.3; 1.4). It comprises a single flow unit emanating from the EAIS interior, terminating into the D'Urville Sea as a heavily fractured ice tongue (Figure 1.3). Ninnis' ice tongue reaches an elevation up to 137 m above sea level with velocities that exceed 1,500 m a⁻¹ (Figure 1.5) (Rignot et al., 2011; Howat et al., 2019). It measured 49.8 km in length and 43.6 km along its terminus in December 2013 and displays an asymmetrical configuration (Figure 1.3). Its western seaboard passes through a pinning point at Dixon Island, located adjacent to a zone of heavy crevassing indicative of regionally high shear rates (Holt and Glasser, 2022). However, the ice tongue's eastern side is unconstrained and sealed in a zone of perennial fast ice (Figure 1.3a).

Ninnis has estimated mass discharge rates as high as $23.0 \pm 1.0 \text{ Gt a}^{-1}$ (2009-2017), draining from its large catchment (178,700 km²) that is among the largest of EAIS outlet glaciers, containing an SLE of 95 cm (Rignot et al., 2019). Its sinusoidal-shaped grounding line is thought to have undergone negligible inland migration between 2010 and 2016 (-0.7 m a^{-1}) (Konrad et al., 2018). One laser altimetry survey by Pritchard et al. (2012) recorded thickening from Ninnis' floating ice at a rate of $0.11 \pm 0.05 \text{ m a}^{-1}$ between 2003 and 2008, whilst Depoorter et al. (2013) recorded a relatively low mean basal mass loss rate ($< -1 \text{ m a}^{-1}$) between 1995 and 2009. Additionally, multi-mission satellite data over a longer time period (1992 and 2017) denoted slight thinning of grounded ice ($> -0.15 \text{ m a}^{-1}$) (Schröder et al., 2019).

Ninnis' ice tongue experiences low mean surface melt rates ($>75 \text{ mm w.e a}^{-1}$) relative to Wilkes Land's major ice shelves and ice tongues, such as Totten ($>100 \text{ mm w.e a}^{-1}$), Dibble ($>120 \text{ mm w.e a}^{-1}$) and Voyeykov ($>150 \text{ mm w.e a}^{-1}$) (Trusel et al., 2013). Recent surveying of Ninnis' bed topography also revealed a retrograde slope with a configuration comparable to Thwaites Glacier, West Antarctica (Morlighem et al., 2020). This reverse slope begins immediately up-ice of the grounding line and is positioned as deep as $-1834.6 \pm 89 \text{ m}$ below sea level (Figure 1.5) (Howat et al., 2019). Its retrograde slope extends inland towards the Wilkes Subglacial Basin (WSB) (3-4 m SLE) (Mengel and Levermann, 2014). Considering the recent changes that have occurred at neighbouring Cook Glacier (Miles et al., 2018), this raises concerns about its future susceptibility to MISI and role in draining ice from the WSB (Pattyn, 2018; Morlighem et al., 2020).

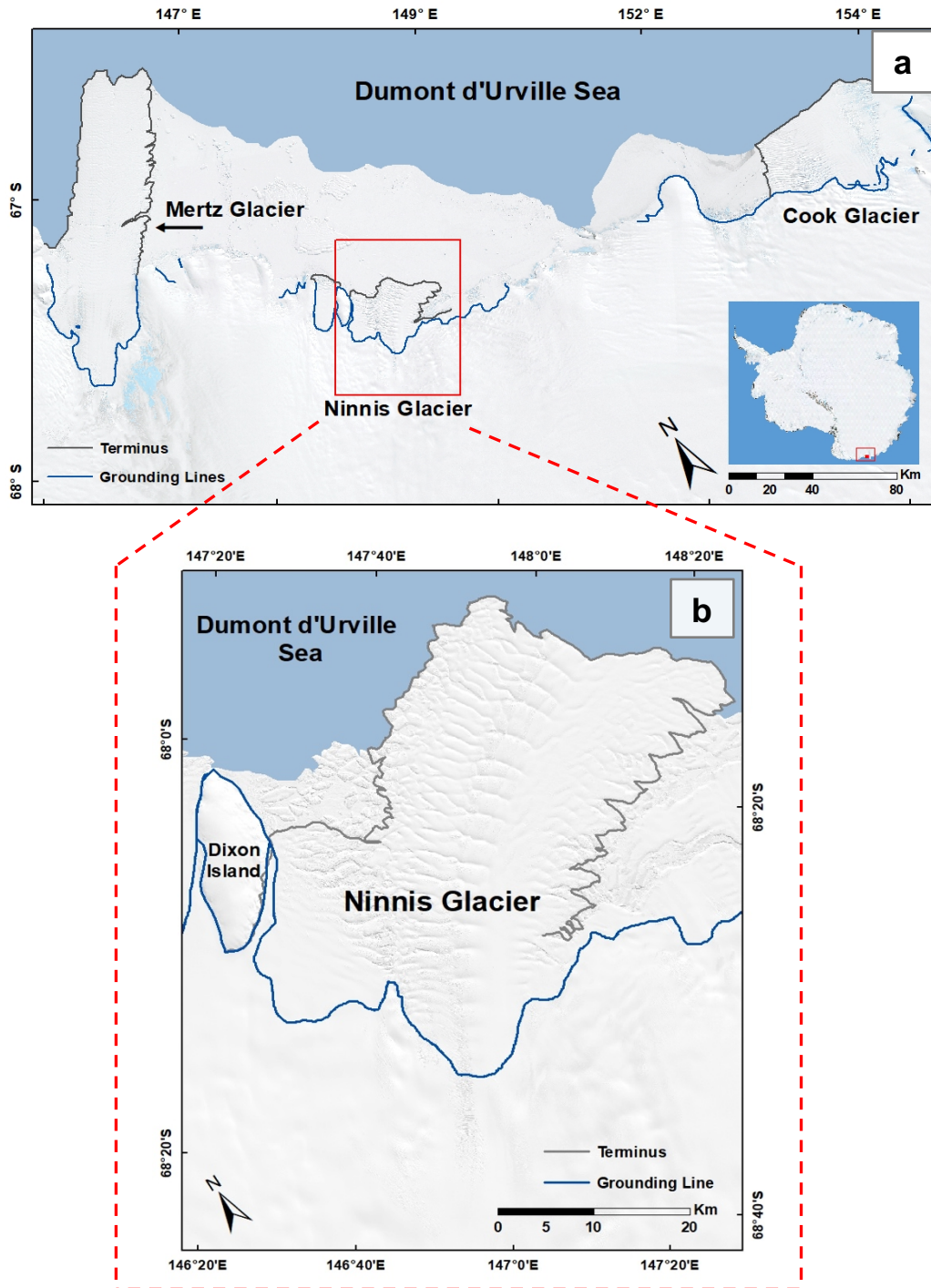


Figure 1.3: (a) Overview of the George V Land coastline from the Landsat Image Map of Antarctica (LIMA) featuring Mertz Glacier, Cook Glacier and Ninnis Glacier (Bindschandler et al., 2008). The red extent indicator depicts the study area used for detailed remote sensing observations of terminus position change, structural and spatial mapping and ice flow velocity. (b) 2013 Landsat image of Ninnis Glacier's ice tongue.

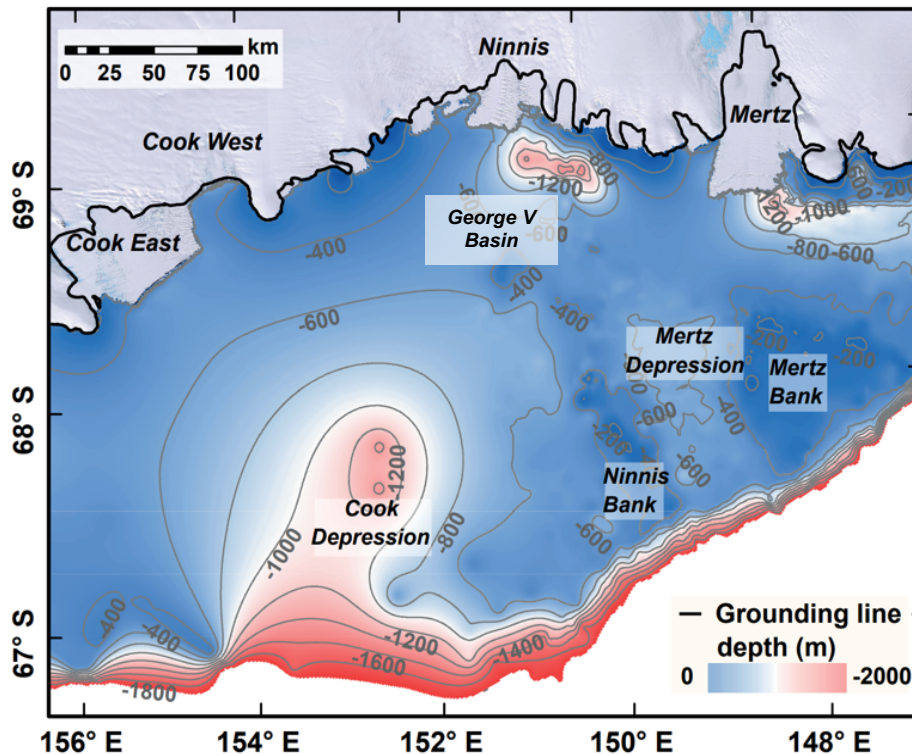


Figure 1.4. General Bathymetric Chart of the Oceans (GEBCO) bathymetric map of the George V Land coastline adjacent to Cook, Ninnis and Mertz Glaciers. Note the George V Basin directly south of Ninnis Glacier, and the Mertz Depression which separates the Mertz and Ninnis Banks. from Miles et al. (2018).

Ninnis Glacier is positioned within a complex atmospheric-oceanographic setting where major ocean currents influence the rate of iceberg and sea ice and drift (Massom, 2003). The Antarctic Divergence (AD) Zone, where average surface winds transition from westerlies (to the north) to easterlies (to the south), is thought to be located near the George V Land coast between ~ 62.5 and 64°S (Bindoff et al., 2000; Massom, 2003). Moreover, the southern fringe of the Antarctic Circumpolar Current, separating eastward-flowing surface ocean currents (to the North) from westward flowing currents of the East Wind Drift, is located proximal to the AD Zone (Bindoff et al., 2000). The George V Land Basin, located parallel to the coastline, provides a drift path for icebergs calved from Ninnis' ice tongue in water reaching depths of $<1,400$ m (Figure 1.4) (Massom, 2003). In the mid-to-outer regions of the continental shelf (148° - 150° E), icebergs drifting from Ninnis become grounded on the shallow (<250 m) Ninnis and Mertz Banks, both separated by the >600 m deep Mertz Depression (Figure 1.4) (Domack and Anderson, 1983). Icebergs emanating from Ninnis and Mertz occupy these linear banks, subsequently influencing both the regional formation and distribution of fast ice and the size of the Mertz Glacier Polynya (Massom, 2003; Tamura et al., 2012).

A recent mass balance assessment flagged Ninnis' floating ice tongue as being potentially vulnerable to mCDW incursions (Rignot et al., 2019). However, the extent of CDW incursions is largely unknown along the coast of the EAIS (Pritchard et al., 2012), with low (0-1° C) thermal forcing temperatures recorded in the coastal waters around Ninnis and Mertz Glacier (Adusumilli et al., 2020). Owing to its initial vulnerability, Ninnis has been identified as a “sector at risk” but it requires significant further investigation (Rignot et al., 2019).

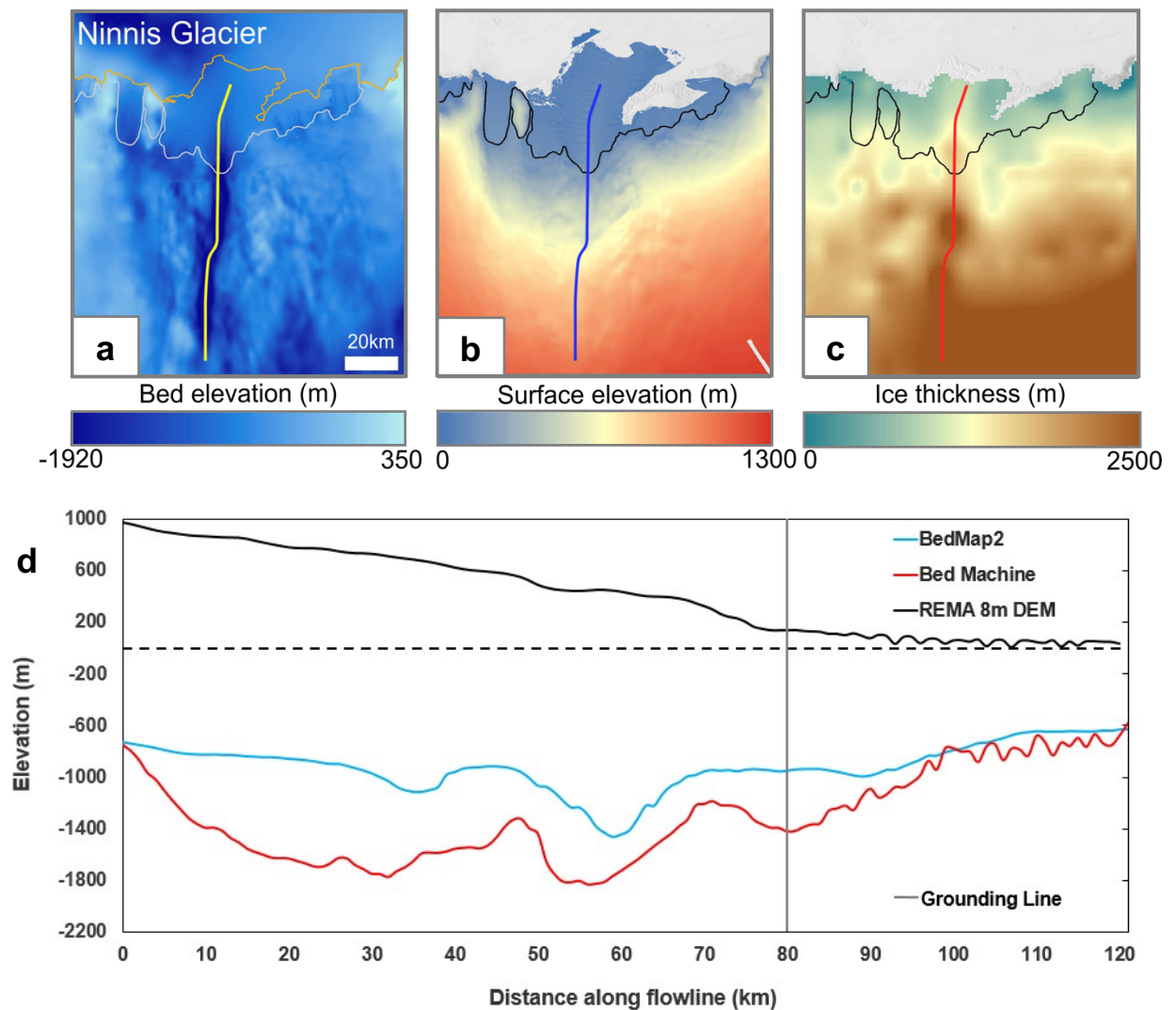


Figure 1.5: Maps depicting elevation of (a) bedrock topography (BedMachine) (Morlighem et al., 2020), (b) surface elevation (REMA) (Howat et al., (2019) and (c) ice thickness (Bedmap2) (Fretwell et al., 2013) at Ninnis Glacier. Maps are overlain with the MEaSURES 1992 grounding line for Ninnis (Rignot et al., 2011). The flowlines visualised in each panel were used to extract the respective profiles. (d) Cross-sectional profiles for bed elevation (Bedmap2, blue and BedMachine, red), surface elevation (REMA, black) and the MEaSURES 1992 grounding line for Ninnis Glacier (grey).

1.7. Thesis structure

Chapter 2 reviews the key scientific literature on the EAIS. Subsections in Chapter 2 outline the following: the past and current consensus on Antarctic and EAIS mass balance (2.1; 2.2), regional differences in Antarctic mass loss and gain (2.3), observational and modelling studies elucidating recent EAIS outlet glacier change (e.g., terminus and grounding line position, ice surface elevation, velocity, and structural glaciology) (2.4) and a review of all literature which focusses on Ninnis Glacier (2.5).

Chapter 3 describes the varying methods employed in this study. This includes the acquisition and processing of satellite imagery (3.2) and the methods used to produce a 58-year time series of terminus position change (3.3). The standardised criteria employed to produce structural glaciological maps across two different time periods (1989-1997 and 2016-2021) are also described (3.4). Secondary datasets acquired to analyse short-term velocity trends at Ninnis Glacier (2006-2011, 2013-2018 and 2018-2021) are described, along with the processing steps to extract velocity data at Ninnis (3.5). Finally, bed topography, ice surface elevation and grounding line datasets are detailed (3.6).

Results from these respective methods are presented in Chapter 4. This includes the results from terminus position mapping across between 1963 and 2021 (4.2), detailed rift maps (1989-1997) and structural glaciological maps (2016 and 2020) (4.3) and ice flow velocity trends across three time periods (2008-2011, 2013-2018 and 2018-2021) (4.4).

Results are discussed in detail in Chapter 5. This includes revisions made to the timing of major calving events previously described at Ninnis (1980-1982 and 2000) (5.2) and a discussion of Ninnis' periodic calving cycle (5.3). Further subsections also discuss the relationships between terminus position change and the observed changes in structural glaciology (5.4) and ice flow velocity (5.5). Chapter 5 also provides a review of a recent observational study made at Ninnis by Cheng et al. (2021) (5.6), as well as detailing the limitations (5.7) and suggestions for further research at Ninnis (5.8). The key conclusions of the thesis are summarised in Chapter 6

Chapter 2: A review of recent East Antarctic Ice Sheet change

2.1. Current estimates of Antarctic mass balance

The IPCC Special Report on the Ocean and Cryosphere in a changing climate (SROCC) reported with *virtual certainty* that the Antarctic Ice Sheet has undergone cumulative mass loss over the past three decades (Meredith et al., 2019). This is based upon recent mass balance estimates which denote losses as high as $109 \pm 56 \text{ Gt a}^{-1}$ between 1992 and 2017, equivalent to a global mean sea-level rise of $7.6 \pm 3.9 \text{ mm}$ (Figure 2.1) (The IMBIE Team, 2018). Signals of mass loss deriving predominantly from the peripheral outlet glaciers and ice shelves of the WAIS and APIS have continued to accelerate since results were published by the IPCC Fifth Assessment Report (AR5) (Church et al., 2013; Martín Español et al., 2016; Zwally et al., 2017; Rignot et al., 2019).

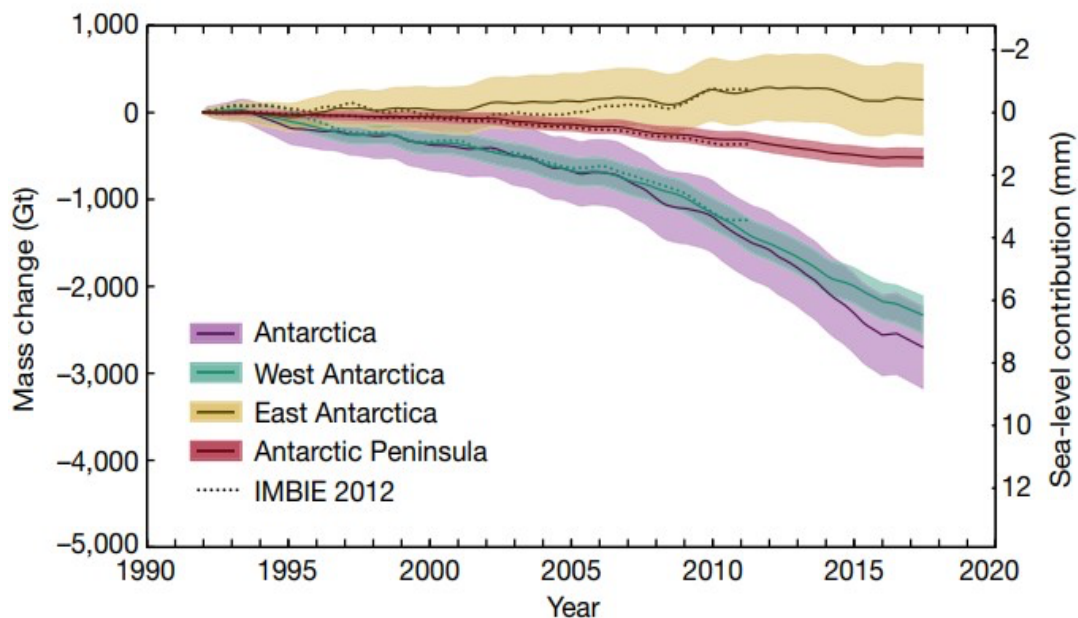


Figure 2.1: Cumulative mass change (Gt) and sea-level contribution (mm) for the Antarctic Ice Sheet between 1992 and 2016 (from the IMBIE Team, 2018).

In the WAIS, ocean-induced melting of outlet glaciers constitutes the largest signals of Antarctic mass loss, increasing from -53 ± 29 (1992-1996) to $-159 \pm 56 \text{ Gt a}^{-1}$ (2012-2016) (The IMBIE Team, 2018). Thwaites, Pine Island, Haynes, Pope, Smith, and Kohler Glaciers in the Amundsen Sea sector of the WAIS, with a combined global SLE of 123 cm, underwent dynamical losses exceeding 136 Gt a^{-1} in 2017. This resulted in pervasive grounding line retreat (Figure 2.2a) (Rignot et al., 2014; 2019). Atmospheric warming since the latter half of

the twentieth century has led to increased recession, thinning and acceleration of APIS outlet glaciers and ice caps (Siegert et al., 2019; Tuckett et al., 2019; Meredith et al., 2019). Between 2010 and 2014, the Western APIS experienced ice mass loss as high as $-56 \pm 8 \text{ Gt a}^{-1}$ (Figure 2.2b) (Cook et al., 2016).

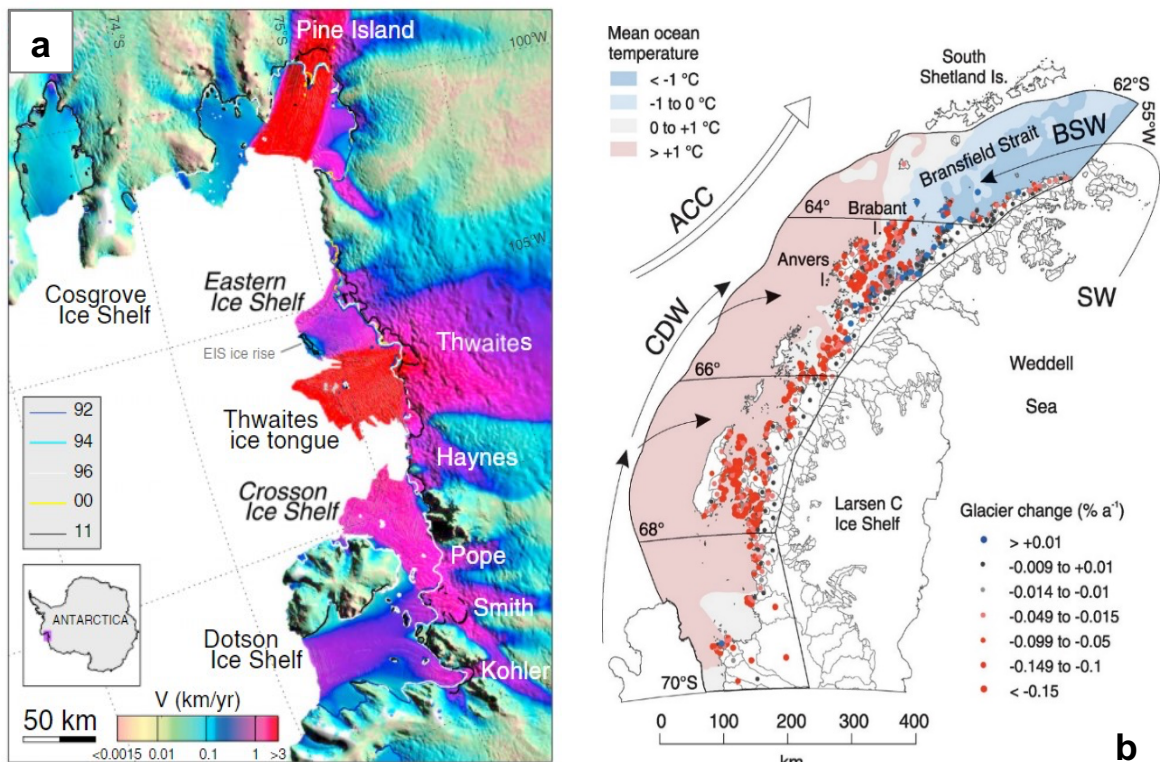


Figure 2.2: (a) Widespread grounding line retreat across outlet glacier in the Amundsen Sea sector of the WAIS (1992-2011) (from Rignot et al., 2014). (b) Mean ocean temperature and glacier area changes (1945-2009) across the western Antarctic Peninsula Ice Sheet (from Cook et al., 2016)

Currently, there is still ongoing debate over the past and current mass balance of the EAIS (The IMBIE Team, 2018), the largest of Antarctica’s constituent ice sheets, covering 85 % of continental ice with a SLE of 53 m (Meredith et al., 2019). Overall, the EAIS is thought to be either gaining mass or close to equilibrium (Zwally et al., 2005; King et al., 2012; Shepherd et al., 2012; McMillan et al., 2014). However, across the satellite era observations have been sparse, displaying no clear trends of EAIS mass loss or gain (The IMBIE Team, 2018; Bamber et al., 2018).

Recent observations have improved our understanding of past and current dynamics of East Antarctic marine-terminating outlet glaciers, particularly of those in the Wilkes Land sector (Miles et al., 2013; 2016). These changes may have contributed to some suggestion of EAIS mass loss between 2012 and 2016 (The IMBIE team et al., 2018; Bamber et al., 2018). However, uncertainties and the lack of consensus surrounding the magnitude of EAIS loss or gain remain high (Rignot et al., 2019; Smith et al., 2020) and spatial patterns of change are highly variable.

2.2. Mass balance of the East Antarctic Ice Sheet (EAIS) since 1992

Various, and often a combination of, estimation techniques have been used to quantify East Antarctic mass balance (Table 2.1). Some studies applied the mass budget method which derives mass balance from the difference between surface mass balance (SMB) input and ice discharge output (Hanna et al., 2013; Rignot et al., 2019). Other methods include laser and radar altimetry, which quantify ice sheet surface elevation change (Zwally et al., 2005; Pritchard et al., 2009; 2012; Smith et al., 2020) or gravimetry which derives ice sheet mass changes from gravitational attraction (Hanna et al., 2013; The IMBIE Team, 2018).

The magnitude of signals varies considerably according to these different methods (Figure 2.3). For example, Zwally et al. (2005) employed radar altimetry to estimate mass gains of $+16 \pm 11 \text{ Gt a}^{-1}$ between 1992 and 2001, whereas Rignot et al. (2008) estimated losses of $-4 \pm 61 \text{ Gt a}^{-1}$ during a similar period (1992-2006) using the mass budget technique. One study assimilated all three methods to reconcile mass balance between 1992 and 2011, yet uncertainties were far greater than the overall mass balance value ($+14 \pm 43 \text{ Gt a}^{-1}$) (Shepherd et al., 2012). Estimates of mass balance over the last two decades also show considerable variation. Notably, King et al. (2012) denoted mass gain of $+60 \pm 13 \text{ Gt a}^{-1}$ between 2002 and 2010, based on gravimetry. In contrast, McMillan et al. (2014) derived slight losses of $-3 \pm 36 \text{ Gt a}^{-1}$ for a similar period between 2010 and 2013 from radar altimetry.

Overall, varying estimation techniques present marked differences in the magnitude of EAIS mass balance with high uncertainties which often exceed their respective signals (Table 2.1). This is partly a consequence of sparse observational data in the EAIS relative to the WAIS and APIS, highlighting the additional focus that is required on the EAIS (Velicogna et al., 2014).

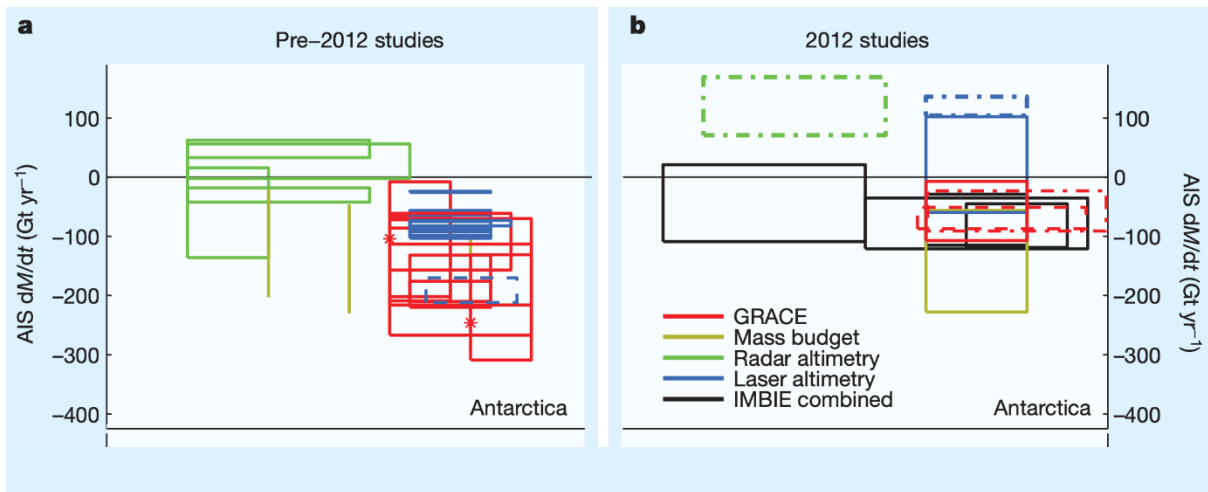


Figure 2.3: Review of pre-2012 (a) and 2012 (b) Antarctic mass balance estimates (Gt a^{-1}) (from Hanna et al., 2013).

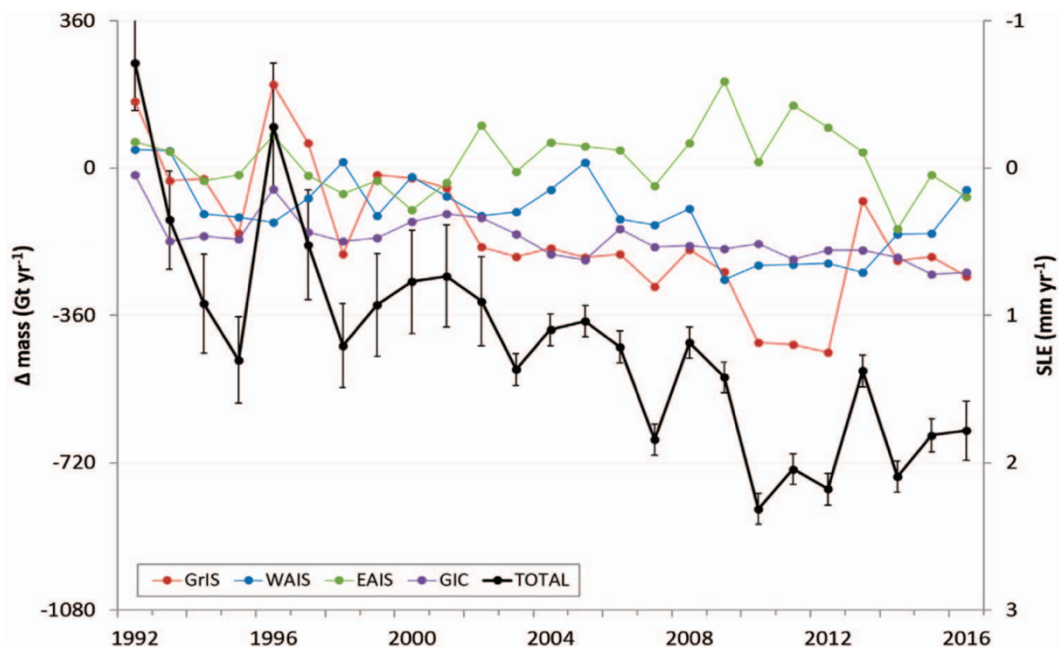


Figure 2.4: Synthesised annual time-series of changes in East Antarctic mass balance (labelled green) between 1992 and 2016 (from Bamber et al. 2018).

To arrive at a consensus on the past and current state of the EAIS, community-based efforts have assimilated varying satellite observations to reconcile Antarctic mass balance over the last three decades (IMBIE et al., 2018; Bamber et al., 2018). Overall, there is a pattern of mass gain recorded for the EAIS between 1992 and 2016 from both the IMBIE Team (2018) ($+15 \pm 41 \text{ Gt a}^{-1}$) and Bamber et al. (2018) ($+18 \pm 52 \text{ Gt a}^{-1}$). This period was marked by pronounced mass loss ($-28 \pm 30 \text{ Gt a}^{-1}$) between 2012 and 2016 according to the IMBIE Team (2018),

which was in slight agreement with values quoted by Bamber et al. (2018) ($-19 \pm 20 \text{ Gt a}^{-1}$). However, there is significant disagreement over EAIS mass balance for the period between 1997 and 2001, with respective figures yielding high uncertainties (Figure 2.4). Whilst Bamber et al. (2019) quantified a $-51 \pm 76 \text{ Gt a}^{-1}$ loss, values from the IMBIE Team (2018) are closer to equilibrium ($+8 \pm 56 \text{ Gt a}^{-1}$). The lack of consensus in EAIS mass balance is further reflected in recent surveys employing singular methods. One study indicates mass loss of $-51.0 \pm 13 \text{ Gt a}^{-1}$ between 2009 and 2017 (Rignot et al., 2019) and another finding gains up to $+106 \pm 29 \text{ Gt a}^{-1}$ for floating ice between 2003 and 2019 (Smith et al., 2020).

Table 2.1: A review of selected multi-method/year estimates of EAIS mass balance (Gt a^{-1}).

Study	Mass Balance Value (Gt a^{-1}).	Time Period	Employed Technique(s)
Zwally et al., (2005)	$+16 \pm 11$	1992-2001	Radar altimetry
Rignot et al., (2008)	-4 ± 61	1992-2006	Mass budget
Shepherd et al., (2012)	$+14 \pm 43$	1992-2011	Altimetry, mass budget and gravimetry
King et al., (2012)	$+60 \pm 13$	2002-2010	Gravimetry
McMillan et al., (2014)	-3 ± 36	2010-2013	Radar altimetry
The IMBIE Team (2018)	18 ± 52	1992-2016	Altimetry, mass budget, gravimetry
Bamber et al., (2018)	15 ± 41	1992-2016	Review of post-AR5 studies
Rignot et al., (2019)	-51.0 ± 13	2009-2017	Mass Budget
Smith et al., (2020) (Floating Ice)	$+106 \pm 29$	2003-2019	Laser altimetry
Smith et al., (2020) (Grounded Ice)	$+90 \pm 21$		

Mass balance estimates by Rignot et al. (2019), quantified using the mass budget method, highlighted East Antarctica as a greater contributor of cumulative mass loss and sea level rise than previously described ($-51.0 \pm 13 \text{ Gt a}^{-1}$) (Figure 2.5) (The IMBIE Team, 2018; Bamber et al., 2019). However, there were distinct differences in the long term (1979-2017) patterns of SMB and ice mass. For example, there was a significant decrease in SMB for the periods

between 1979 and 1989 ($+23 \pm 3 \text{ Gt a}^{-1}$) and 2009 and 2017 ($-14 \pm 9 \text{ Gt a}^{-1}$) which dominated the decadal variability in EAIS mass balance. While there is no evidence of a significant acceleration in overall ice mass discharge between 1979 and 2009, increases in the overall mass loss signal were estimated to be primarily driven from trends in SMB rather than dynamical ice mass loss. Between 2009 and 2017 ice mass discharge was higher ($-37 \pm 9 \text{ Gt a}^{-1}$) than that between 1999 and 2007 ($-28 \pm 5 \text{ Gt a}^{-1}$). However, this signal emanated predominantly from major outlet glaciers within the Wilkes Land sector (e.g., Totten and Denman). These recent high magnitude losses suggested that relatively warm CDW intrusions have become more pronounced in the EAIS than previously estimated (Pritchard et al. (2012).

Regional variations in mass loss and gain across the EAIS were also presented for major individual outlet glaciers by Rignot et al. (2019), highlighting potential “sectors of risk”, including the Denman/Shackleton ice shelf (149 cm SLE), Cook (158 cm SLE) and Ninnis (95 cm SLE).

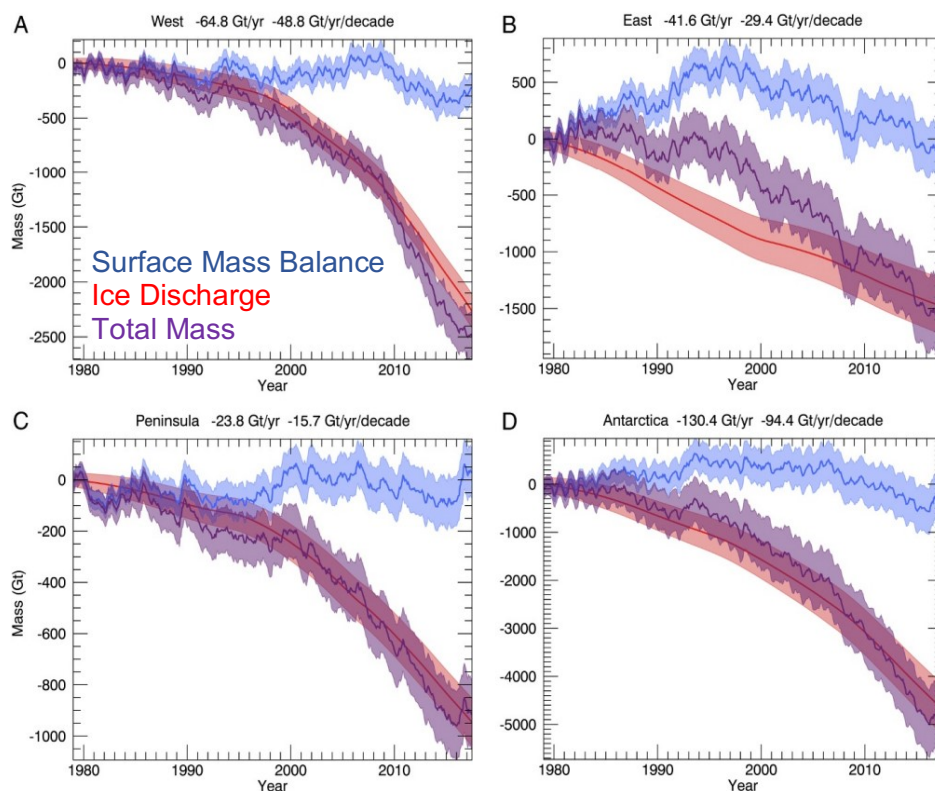


Figure 2.5: Time series of cumulative change in surface mass balance (SMB) (blue), ice discharge (red) and total mass balance (purple) (Gt a^{-1}) for (A) West Antarctica, (B) East Antarctica, (C) Antarctic Peninsula and (D) the entirety of Antarctica between 1979 and 2017 (from Rignot et al., 2019).

2.3. Regional changes in the East Antarctic mass budget

The EAIS mass budget between 1979 and 2017 revealed that 97 % of its mass loss derived from specific sectors of the Antarctic Ice Sheet where ice mass discharge exceeded its SMB (Figure 2.6) (Rignot et al., 2019). The Wilkes Land sector dominated negative EAIS mass balance anomalies and contributed $+4.4 \pm 0.9$ mm of SLR between 1979 and 2017. Notable mass losses from Wilkes Land are sourced from Totten Glacier which underwent rates of discharge ranging from 69.0 to 71.4 ± 2.6 Gt a^{-1} in the same period, contributing $+0.7$ mm of SLR (Rignot et al., 2019). Despite this, Totten remains within 10 % of its balance flux (Li et al., 2016). Similar trends were observed in Porpoise Bay, whereby sea ice break-up induced by warmer-than-usual austral summers led to simultaneous disintegration for Holmes (11 cm SLE), Dibble (12 cm SLE) and Frost (84 cm SLE) glaciers (Miles et al., 2017) (Rignot et al., 2019). However, some glaciers within the same region have varying magnitudes of mass loss and gain. Notably, Moscow University in the Wilkes Land sector, gained mass at a negligible rate ($+0.3$ Gt a^{-1}) between 2009 and 2017 despite discharging 3 Gt a^{-1} of ice between 1979 and 2003 (Rignot et al., 2019).

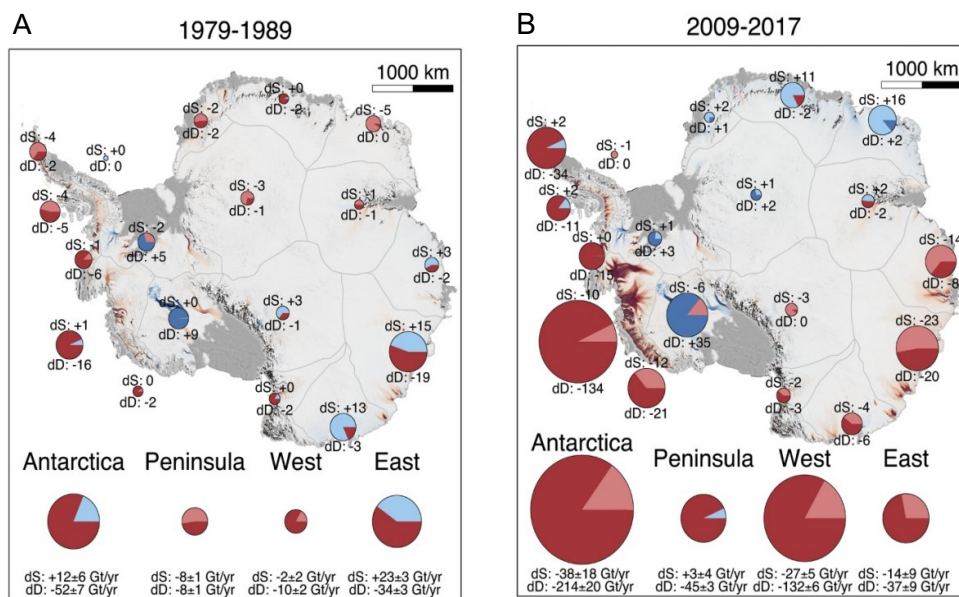


Figure 2.6: Time series of cumulative change in surface mass balance (SMB), ice discharge (red) and total mass balance (blue) (Gt a^{-1}) for West Antarctica (A) and East Antarctica (B), between 1979 and 2017 (from Rignot et al., 2019).

Elsewhere, the Amery Ice Shelf system remained in balance and has undergone no fluctuations in velocity between 1979 and 2017. However, recent observations have provided evidence of ice surface thinning via melt ponding and surface water drainage on the Amery

Ice Shelf (Dell et al., 2021; Fricker et al., 2021; Spergel et al., 2021). Queen Maud Land's outlet glaciers have gained mass, equivalent to $+63 \pm 6 \text{ Gt a}^{-1}$ (Velicogna et al., 2014), notably after a major snowfall event which added 200 Gt of mass to the EAIS in 2009 (Rignot et al., 2019).

A recent laser altimetry analysis by Smith et al. (2020) also attempts to understand Antarctic Ice Sheet mass balance, highlighting significantly large signals of mass gain among the grounded ($+90 \pm 21 \text{ Gt a}^{-1}$) and floating portions ($+106 \pm 29 \text{ Gt a}^{-1}$) of East Antarctic outlet glaciers between 2003 and 2009. However, even though the overall mass balance was positive, Smith et al. (2020) detected a strong signal of mass loss from Wilkes Land's outlet glaciers (Figure 2.7).

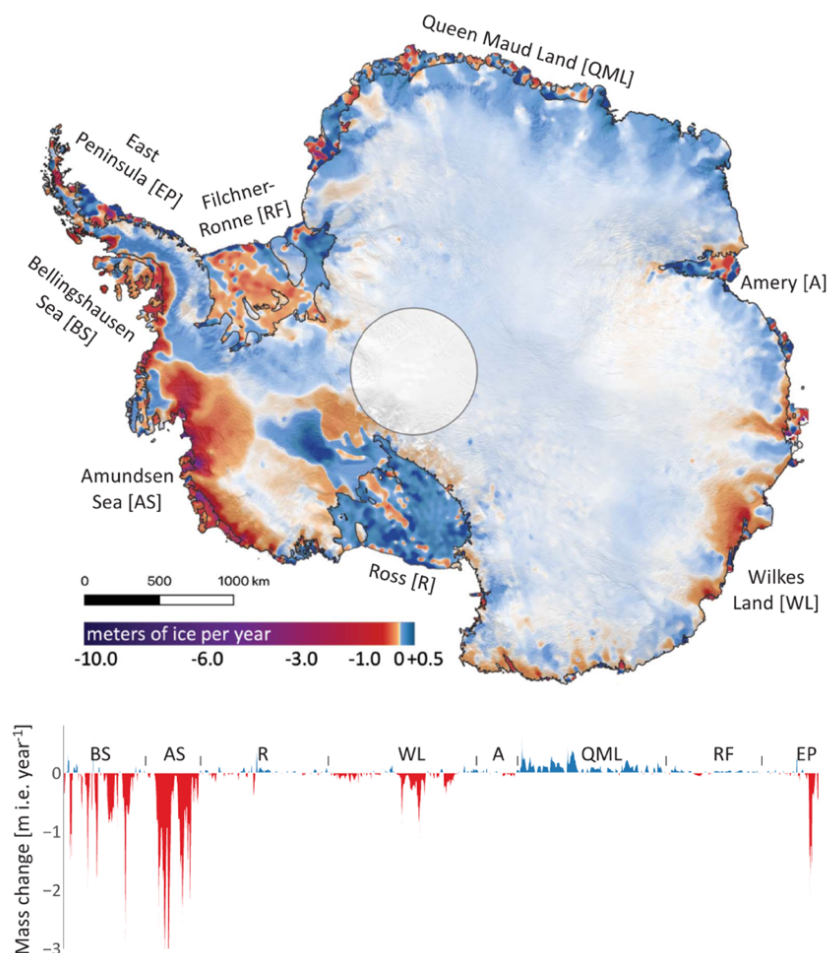


Figure 2.7: Above: Magnitudes of Antarctic mass loss (meters of ice per year) between 2003 and 2019. Below: Mass changes observed at the grounding line. Note the highest recorded East Antarctic mass losses in Wilkes Land (from Smith et al., 2020).

2.4. Elucidating the drivers of East Antarctic outlet glacier change

2.4.1. Introduction

There is a strong consensus on the climatic and oceanic forcing factors that drive outlet glacier and ice shelf changes outside of East Antarctica. In the APIS, multiple studies have attributed the disintegration of the Larsen A, Larsen B and Prince Gustav ice shelves to an intensifying atmospheric warming trend over the past four decades, governed by positive Southern Annular Mode (SAM) index (Cape et al., 2015; King et al., 2017; Turton et al., 2018). In the WAIS, positive SAM index is known to drive the upwelling of warm modified Circumpolar Deep Water (mCDW), facilitating glacier discharge where portions of its grounded ice and grounding lines are positioned below sea level (Spence et al., 2014; Milillo et al., 2019).

Observations of East Antarctic outlet glacier change prior to 2013 were limited in comparison to the APIS and WAIS and presented no discernible trends in glacier fluctuations (Wendler et al., 1996; Frezzotti, 1997; Frezzotti et al., 1998; Rolstad et al., 2000; Frezzotti and Polizzi, 2002). Most notably, prior observations of large East Antarctic outlet glaciers (e.g., David, Mertz and Ninnis) attributed large-scale and periodic tabular iceberg calving events to naturally occurring cycles (Frezzotti and Mabin, 1994; Massom et al., 2001; Massom, 2003). Little attention was placed on associating potential ocean-climatic forcing factors with major calving events, as a localised mass balance investigation by Rignot (2002) quantified negligible imbalances at David, Mertz, Ninnis and on other major outlets (e.g., Totten, Scott and Denman) (Rignot, 2002).

2.4.2. Ocean drivers of Antarctic glacier change

Oceanic processes are a driving mechanism for recent Antarctic ice sheet change, notably Circumpolar Deep Water (CDW) currents which have contributed to enhanced basal melt for major Antarctic ice shelves and glaciers (Pritchard et al., 2012; Depoorter et al., 2013). CDW is a relatively warm, saline water mass which flows onto, and across, the Antarctic Ice Sheet's continental shelf (Dinniman et al., 2012). In the eastern Amundsen Sea of the WAIS, CDW intrusions reach the continental shelf at depths exceeding 300 m and at $> 3.5^{\circ}\text{C}$ above freezing point. This is positioned within the bottom layer of an ocean thermocline (temperature-salinity gradient) (Jacobs et al., 2012). Here, CDW is overlain with a layer of colder, fresher surface water, which combine with local fast ice production to prohibit High Salinity Shelf Water (HSSW) formation (Dinniman et al., 2003; Stewart and Thompson, 2015), commonly found on the continental shelf of the EAIS (Kushara et al., 2013; Yoon et al., 2020).

Although the Amundsen Sea sector's continental shelf provides a barrier for regional deep-water currents (Jacobs et al., 2012), subglacial troughs and depressions act as pathways for CDW intrusions onto the continental shelf, depending on the height of the CDW column (Walker et al., 2007). This process facilitated widespread recession, thinning and acceleration of major Amundsen Sea sector outlet glaciers (Rignot et al., 2014). Mostly notably, Pine Island Glacier (PIG) (51 m SLE) underwent a reduction in ice shelf buttressing in response to an increase in temperature and volume of CDW intrusions which accessed the glacier via its deep subglacial trough (Walker et al., 2007; Jacobs et al., 2012). Ocean modelling experiments showed that PIG's meltwater production increased by 50 % between 1994 and 2009, resulting from CDW-induced sub-marine ice shelf melt (Jacobs et al., 2012). As basal melt exceeded the rate of ice shelf flow, an inner cavity formed and migrated inland, allowing water $<4^{\circ}\text{C}$ above freezing point to access PIG's grounding line (Jacobs et al., 2012). Between 1992 and 2011, PIG's grounding line retreated by 31 km, increasing its susceptibility to MISI (Rignot et al., 2014; Favier et al., 2014). Overall, CDW intrusions beneath major WAIS outlet glaciers are becoming more frequent in response to enhanced westerly winds associated with tropical forcing and positive SAM index (Steig et al., 2012; Dinniman et al., 2012). This raises questions surrounding the potential impact of changes in the ocean-climate system to major EAIS outlet glaciers.

2.4.3. Decadal observations of widespread EAIS outlet glacier change

Consensus on the state of East Antarctica's outlet glacier behaviour was brought to question by ICESat altimetry surveys (Pritchard et al., 2012) (Pritchard et al., 2012). Between 2003 and 2008 relatively warm CDW incursions initiated basal melt on the floating portions of major outlet glaciers in the Wilkes Land sector (Pritchard et al., 2012). For instance, net ice shelf thinning was recorded at Holmes and Dibble Glaciers and the thickest part of the Totten Ice Shelf, which thinned at rates between 0.24 and 0.41 m a^{-1} (Pritchard et al., 2012). Ice shelf thinning trends in Wilkes Land demonstrated that East Antarctica's outlet glaciers were in fact more sensitive to external forcing than previously considered (Pritchard et al., 2009). This provided the rationale for one study to quantify terminus position change across 175 marine-terminating outlet glaciers spanning 5,400 km of the EAIS coastline (Miles et al., 2013). Around 300 satellite images between 1974 and 2010 were analysed at multi-decadal resolution, revealing rapid, widespread and synchronous terminus position changes in response to ocean-climate forcing across some sectors of the EAIS. Overall, Wilkes Land and George V Land glaciers underwent synchronous retreat phases (1974-1990; 2000-2010) in response to warmer-than-usual austral winter air temperatures and a more positive SAM index (Figure 2.8). Temperatures in Wilkes Land were 9-12 $^{\circ}\text{C}$ warmer than the much colder Ross Sea sector

(Victoria Land), positioned south of the Antarctic circle, with its glaciers displaying no discernible terminus position changes over the last 40 years (Figure 2.8) (Miles et al., 2013). While this study provided accounts of previously unrecorded regional variability in EAIS outlet glacier behaviour, less attention was placed on quantifying change at sub-decadal resolution.

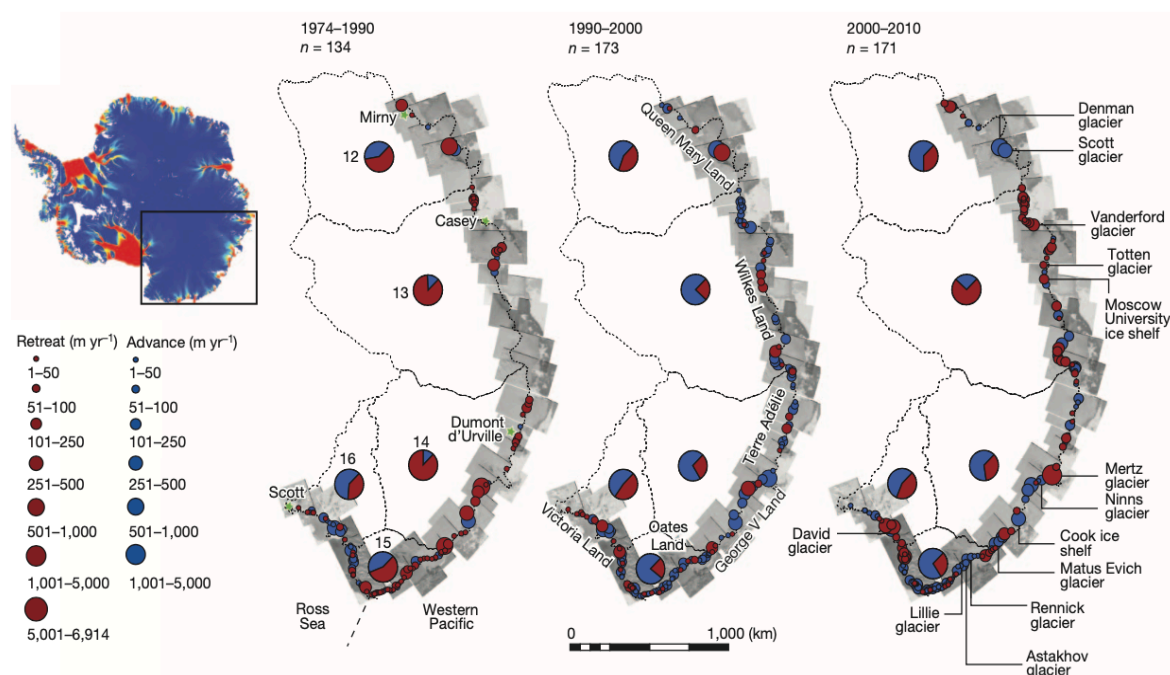


Figure 2.8: Temporal variations in terminus position change across different regions of the EAIS (1974-1990; 1990-2000; 2000-2010). Magnitude of terminus position changes (m a^{-1}) for each respective outlet glacier are visualised in single-colour circles (Blue = Advance; Red = Retreat), whilst pie charts visualise the percentage of advancing and retreating glaciers for each major drainage basin. (from Miles et al., 2013).

A study by Lovell et al., (2018) mapped terminus position changes across 135 outlet glaciers spanning the Victoria Land, Oates Land and George V Land coastlines at a higher (sub-decadal) resolution between 1972 and 2013. Approximately 36 % of all glaciers advanced, 27 % retreated and the remaining glaciers underwent no changes. Glaciers in Victoria Land were the most stable and rarely exhibited phases of advance or retreat beyond $+ 42.8 \pm 1.6 \text{ m a}^{-1}$, correlating with observations in the same sector by Miles et al. (2013). Oates Land glaciers underwent slightly greater changes ($+ 47.6 \pm 1.6 \text{ m a}^{-1}$), whilst the greatest variations were observed across George V Land. This sector underwent advances as high as $1,101 \text{ m a}^{-1}$ (1972-1988) and retreat phases as high as $-14,177 \text{ m a}^{-1}$ (2009-2013) (Lovell et al., 2016).

While negligible changes in terminus position across Victoria Land reflect its cold regional climate, variations observed across Oates Land and George V Land were not directly correlated to air temperature. Analysis of climate data revealed that the warmest average temperatures were recorded in Oates Land (-0.3°C), whilst an air temperature cooling trend from 1980 onwards was recorded at George V Land despite experiencing the greatest magnitude glacier fluctuations (Lovell et al., 2018). This revealed that atmospheric temperatures in the EAIS did not play a critical role in modulating the retreat of its outlet glaciers compared to that observed at the APIS (Banwell et al., 2013). Alternatively, theories of glacier (de-)buttressing from sea ice were considered, attributing epochs of advance and retreat at Oates Land and George V Land to high and low observed sea ice concentrations (Amundson et al. 2010; Fukuda et al. 2014; Lovell et al., 2016). However, the study acknowledged that further work was necessary on individual glaciers to elucidate the factors behind recent changes.

2.4.4. Detailed observations elucidating East Antarctic outlet glacier change

Recent observations have focussed on singular, or a cluster of, glaciers emanating from the same EAIS drainage basin, elucidating regional factors that contributed to widespread changes in outlet glacier (Miles et al., 2013; Lovell et al., 2016). For example, a time-series of terminus position change across six marine-terminating outlet glaciers in Porpoise Bay by Miles et al. (2017) captured a near-synchronous calving event in January 2007 and the start of a similar calving event in March 2016 (Figure 2.9). Both calving events were characterised by wide-spread ice tongue disintegration, analogous to that of the Larsen A and B ice shelves in the APIS (Rott et al., 1996; Rignot et al., 2004; Scambos et al., 2009; Hogg and Gudmundsson, 2017). This raised concerns for potential ocean-climatic forcing mechanisms which initiated these calving events. Detailed observations linked both calving events to extensive break-up of Multi-Year Landfast Sea Ice (MYLI) occupying Porpoise Bay, subsequently leading to a loss of buttressing of the glacier termini (Miles et al., 2017). However, MYLI break-ups in 2007 and 2016 were triggered by contrasting mechanisms. The 2007 disintegration was linked to an atmospheric circulation anomaly in December 2005 which weakened the multi-year sea ice through surface melt and changing wind direction. By contrast, the March 2016 event was linked to a long-term calving cycle of Holmes (West) Glacier (Figure 2.9b), whereby its advancing tongue pushed the protective sea ice out of Porpoise Bay. This study not only highlighted the importance of sea ice in modulating calving activity in East Antarctica, but also the complex mechanisms that drive sea ice break-up and calving position (Miles et al., 2017).

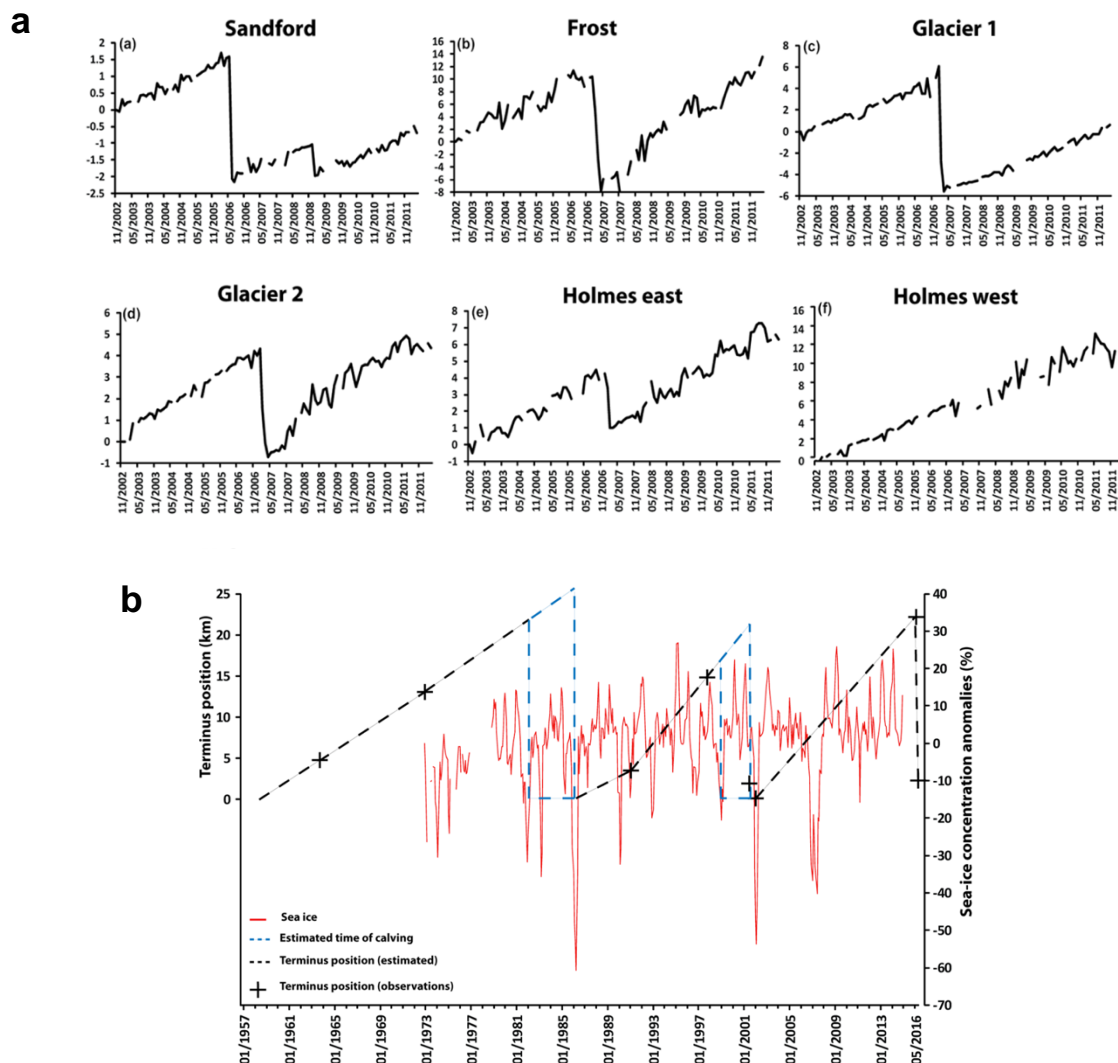


Figure 2.9. Calving cycle reconstructions across Porpoise Bay. (a) Time-series of terminus position change for six major outlet glaciers in Porpoise Bay between November 2002 and March 2012. Note the synchronous calving event in 2007 for Sandford, Frost, Glacier 1, Glacier 2 and Holmes East. (b) The calving cycle of Holmes West Glacier between and sea ice anomalies between 1957 and 2016 (from Miles et al. 2017).

Further observations denoting the importance of sea ice concentrations proximal to East Antarctic Glacier and ice shelf margins were made recently at the Voyeykov Ice Shelf (VIS), Wilkes Land. Between 27th March and 28th May 2007, the VIS underwent rapid disaggregation of its floating ice shelf in response to a large-scale (~2,445 km²) break-up of sea ice mélange (Arthur et al., 2021). Glaciers and ice shelves display ranging surface structures (e.g., rifts, crevasses and fractures) that are indicative of past and present glacier dynamical processes (Jennings and Hambrey, 2021). As surface features are known to evolve prior to ice shelf

recession or break-up (Vieli et al., 2007), Arthur et al. (2021) presented a detailed structural assessment to elucidate the triggering mechanisms of the 2007 VIS disaggregation. This revealed the pre-cursors to disaggregation in the form of transverse rifts on Voyeykov's central flow unit which were internally bound by sea ice. Weakening of the mélange surrounding the ice shelf, believed to be triggered by anomalies in regional atmospheric circulation, led to rift propagation as they became unconstrained by sea ice (Figure 2.10). Although the disaggregation of the VIS did not trigger an acceleration of inland ice, observations highlighted the mechanical coupling between sea ice and floating ice shelves. Whilst it is known that sea ice plays an important role in sealing rift zones, which slow down their propagation and thus delay the timing of calving (Arthur et al., 2021), internal factors have been linked to the prevention of rift growth. Investigations on the Drygalski Ice Tongue, Victoria Land, revealed that heterogeneities in ice rheology as the ice tongue thins downstream leads to greater rates of rift propagation, triggering large scale calving events (Indrigo et al., 2020).

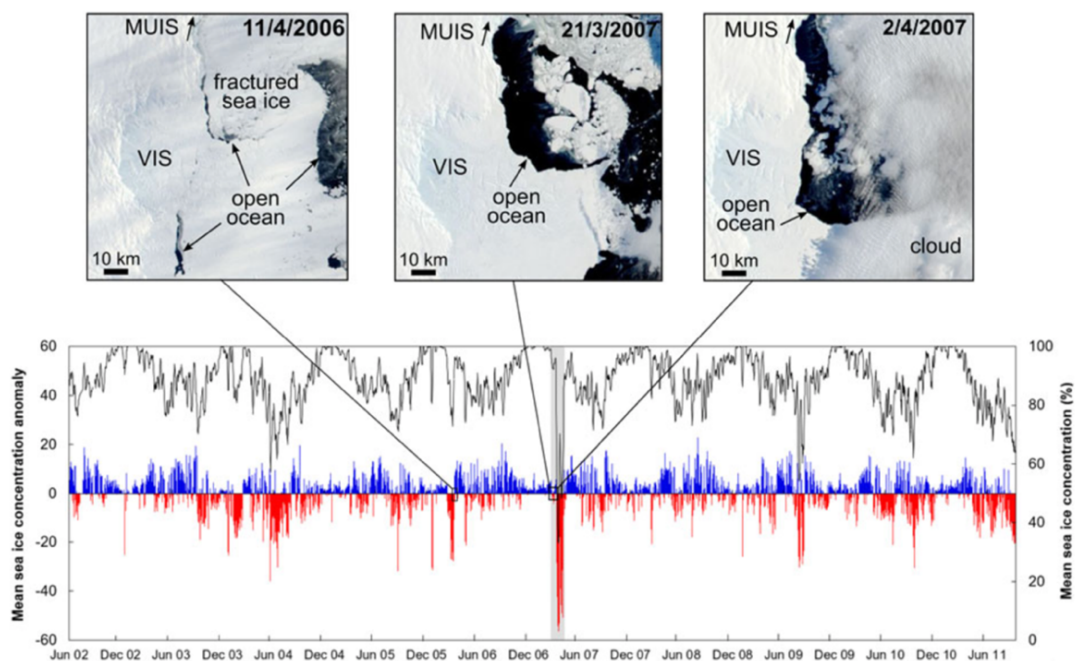


Figure 2.10. AMSR-E daily sea-ice concentration anomalies extracted off-shore of the Voyeykov Ice Shelf between June 2002 and December 2011. Positive anomalies = blue lines and negative anomalies = red lines. Ice shelf disaggregation between March and April 2007 is visualised using the grey bar and correlated with a negative anomaly in sea ice concentrations (from Arthur et al., 2021).

2.4.5. Observations of potentially unstable East Antarctic Outlet Glaciers

Subglacial bed topography plays a key role in Antarctic outlet glacier retreat rates (Serroussi et al., 2017; Winter et al., 2020), so it is important that the landscape beneath the AIS is well constrained. The gridded products of Bedmap2 provided valuable insights into surface elevation, ice thickness and subglacial bed elevation (Fretwell et al., 2013). However, under sampling in some sectors, particularly in East Antarctica, resulted in large uncertainties (Fretwell et al., 2013). BedMachine was developed to increase the resolution of Antarctic bed topography based on mass conservation methods (Morlighem et al., 2020). BedMachine revealed hitherto unrecorded subglacial features which would improve estimates of ice discharge rates within mass balance calculations and sea level projections (Figure 2.11). This included retrograde slopes beneath major East Antarctic outlet glaciers draining large subglacial basins, including at Denman and Ninnis Glaciers (Figure 2.11f;h).

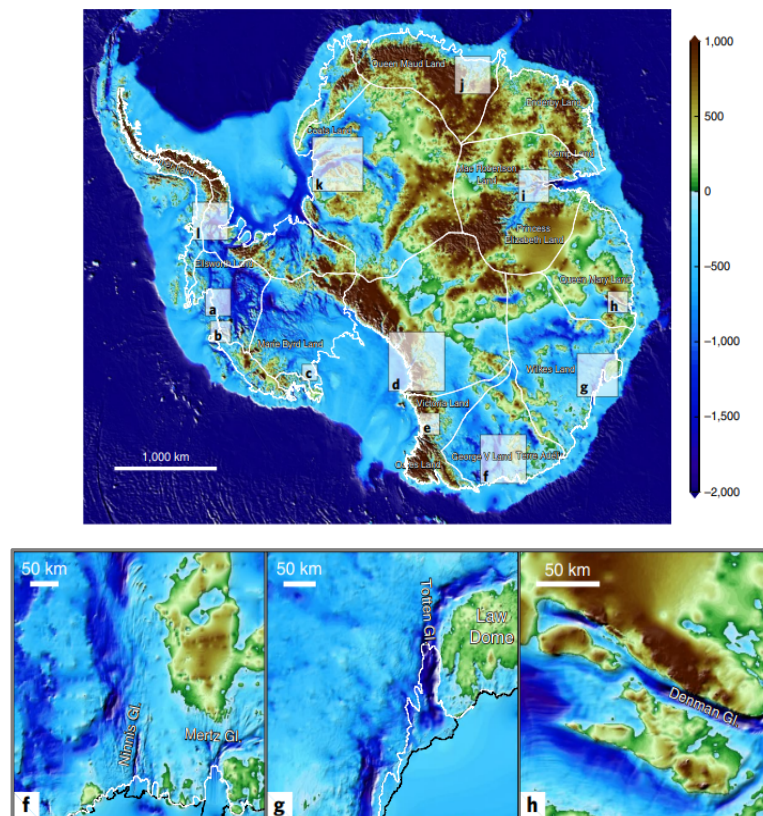


Figure 2.11: Bed Machine map depicting bed elevation for the Antarctic Ice Sheet. White lines delineate drainage basins by The IMBIE Team (2018). Numbered extent indicators refer to subglacial bed elevation for major outlet glaciers (a-l). Panels below (f-h) depict bed elevation for Ninnis (f), Totten (g), and Denman (h) are shown below (from Morlighem et al., 2020).

Prior to the release of BedMachine, most observations of East Antarctic outlet glaciers focussed on Totten (3.9 m SLE) in the Wilkes Land sector. Totten exhibited the highest rates ice shelf thinning in East Antarctica (Pritchard et al., 2012; Flament and Remy, 2012), suggesting potential basal melt from ocean forcing (Pritchard et al., 2012). Bathymetric surveys revealed an ice shelf cavity reaching depths between 400 and 500 m beneath the Totten Ice Shelf which may have provided access for relatively warm mCDW intrusions to facilitate basal melt (Figure 2.12) (Greenbaum et al., 2015). It was argued by Li et al. (2015) that this ice shelf cavity may have also played a key role in a 1 to 3 km retreat of Totten's grounding line between 1996 and 2013. This retreat pattern was associated with an ice shelf thinning rate estimated $0.7 \pm 0.1 \text{ m a}^{-1}$, but potential MISI is unlikely because its grounding line remained far from an inland retrograde slope (Morlighem et al., 2020). The extent to which these changes were triggered by mCDW intrusion were unknown due to minimal oceanographic observations made beneath Totten's ice shelf at the time (Li et al., 2015).

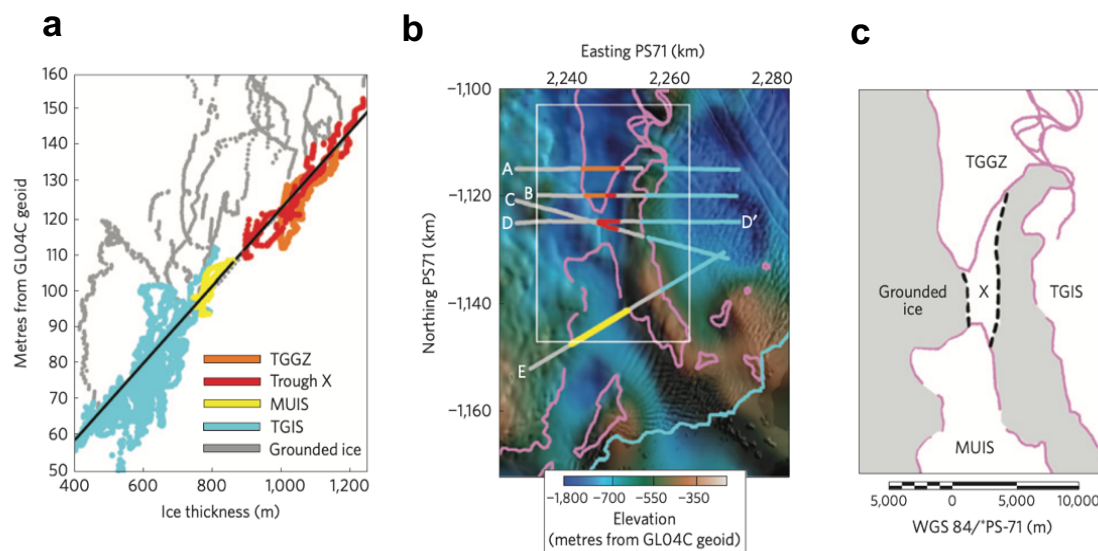


Figure 2.12: Bathymetric profile for the newly discovered cavity below the Totten Shelf. (a) Ice-surface elevation plotted against ice thickness derived from the five elevation profiles beneath the Moscow University Ice Shelf (MUIS), Totten Glacier Grounding Zone (TGGZ) and Totten Glacier Ice Shelf (TGIS), visualised in panel b. (c) Expanded map from the grey extent indicator in panel b. Note the newly discovered trough (X) from the low elevation profile beneath the TGIS (panel a) (from Greenbaum et al., 2015).

It was later confirmed that basal melt and grounding line retreat were modulated by mCDW incursions (Rintoul et al., 2016), entering the same cavity uncovered by Greenbaum et al. (2015). These recent changes observed at Totten Glacier are analogous to that experienced in the Amundsen Sea sector of the WAIS (Pritchard et al., 2009; Gwyther et al., 2014; Smith

et al., 2020), providing evidence that ice mass loss of major EAIS outlet glaciers was modulated by regional ocean-climatic forcing.

Recent remote sensing observations have often targeted EAIS outlet glaciers with grounding line positions near or atop retrograde slopes (Morlighem et al., 2020). Cook Glacier is a major outlet situated in the George V Land sector of East Antarctica thought to be susceptible to MISI owing to its sub-glacial troughs connected to WSB (Mengel and Levermann, 2014). Recent long-term observation of terminus position change (1947-2017) and velocity (1973-2017) revealed significant changes in the dynamics of the Cook East and Cook West ice shelves (Miles et al., 2018). A major tabular calving event took place at Cook East sometime between 1963 and 1974, which resulted in the complete loss of “passive ice” and formed a new terminus position deep into its constrained embayment (Figure 2.13a) (Miles et al., 2018). However, re-advance immediately followed with negligible grounding line change observed between 2010 and 2018 (Konrad et al., 2018), indicating the retreat did not pre-dispose the glacier to MISI. Although a short-term increase in velocity was observed, this was linked to the drainage of subglacial Lake Cook (Stearns et al., 2008; Miles et al., 2018).

In contrast, the Cook West Ice Shelf retreated 34 km over two distinct phases between 1947 and 2018. The first occurring between 1947 and 1963, punctuated by a period of stabilisation until 1973, which was followed by a further 13 km retreat until 2018. This culminated the complete loss of the Cook West Ice Shelf, with its 2018 terminus position positioned close to its grounding line (Figure 2.13b) (Miles et al., 2017; Rignot et al., 2011). Cook West’s ice shelf loss was flagged as uncharacteristic behaviour for large East Antarctic ice shelves, with no other observations in the EAIS recording persistent terminus retreat to their grounding line (Miles et al., 2013; 2016; Lovell et al., 2016). This was attributed to a doubling in ice flow velocity in response to reduced buttressing as the terminus retreated and inland ice underwent dynamical thinning between 1992 and 2010 ($\sim 50 \text{ cm a}^{-1}$) (Schröder et al., 2019). Although dynamical thinning at Cook West is significantly less compared to that of the Amundsen Sea sector in the WAIS (Pritchard et al., 2012; Depoorter et al., 2013; Schröder et al., 2018), observations revealed the sensitivity of inland ice to changes in terminus position and surface elevation change.

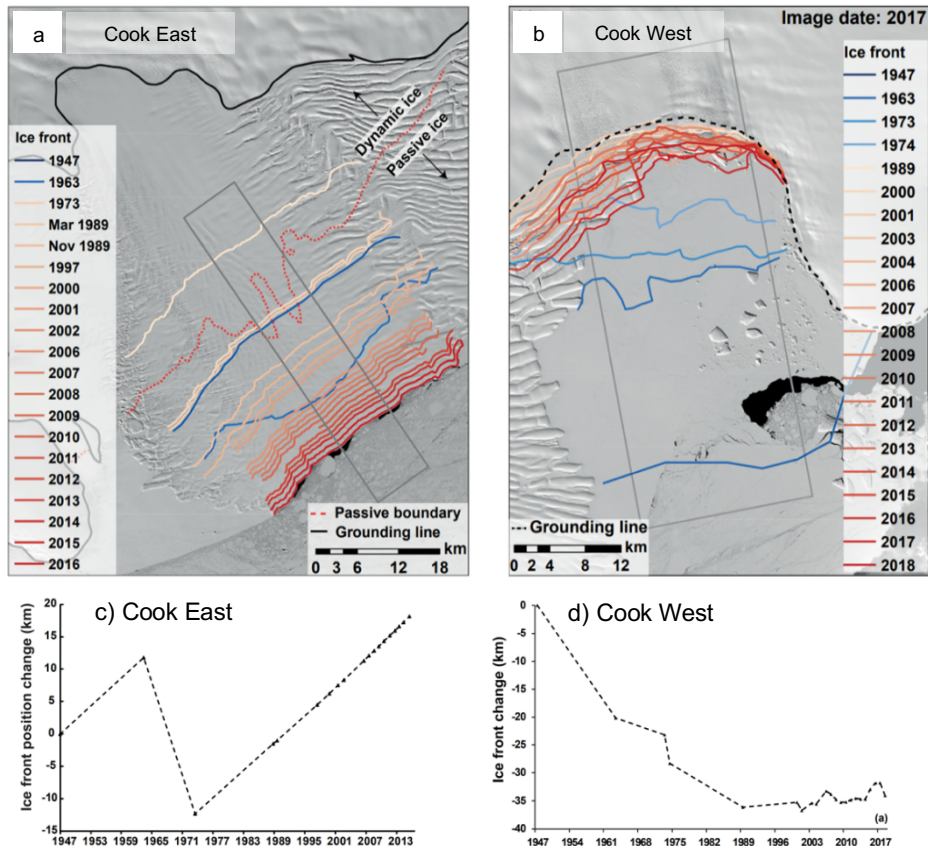


Figure 2.13: (a) Mapped changes in terminus position for the Cook East Ice Shelf and (b) Cook West Ice Shelf between 1947 and 2016, overlain with grounding line position and passive ice boundary (Fürst et al., 2016). Cumulative terminus position change was quantified using the black box. (c) Cumulative terminus position change for the Cook East Ice Shelf. (d) Cook West Ice Shelf between 1947 and 2017 (from Miles et al., 2018).

One outlet glacier which was identified by Morlighem et al. (2020) as being potentially vulnerable to MISI is Denman Glacier (1.5 m SLE). Denman is the second largest contributor to global mean sea level from East Antarctica, which lost an estimated -190 Gt of ice between 1979 and 2017, slightly comparable to that of Totten Glacier (-236 Gt) (Rignot et al., 2019). Denman's grounding line has been retreating along a retrograde slope over the last 20 years (Brancato et al., 2020) and experienced thinning inland of its fast-flowing ice trunk between 1992 and 2017 (Schröder et al., 2019). Basal melt rates (1995-2009) at Denman are comparable to that of the Getz Ice Shelf in West Antarctica (Depoorter et al., 2013) and are suggestive that mCDW incursions reached the ice cavity beneath Denman's ice shelf, similar to that of Totten (Rintoul et al., 2016; Gwyther et al., 2018; Brancato et al., 2020).

Recent observations of Denman's calving cycle, changes in velocity and the structure of its large ice tongue between 1972 and 2017 have recently been made (Miles et al., 2021). This revealed a periodic calving cycle similar to that of Mertz Glacier and the Cook East Ice Shelf (Giles, 2017 Miles et al., 2018; 2021). However, velocity analysis for the period 1972 and 2017 recorded a $17 \pm 4 \%$ and $6 \pm 5 \%$ acceleration on the grounded and floating portions, respectively. Perturbation experiments were simulated to elucidate the factors that initiated this acceleration. Results revealed that a combination of grounding line retreat, ice shelf thinning and ungrounding of its pinning point on Chugunov Island was necessary to facilitate this widespread acceleration (Figure 2.14) (Miles et al., 2021).

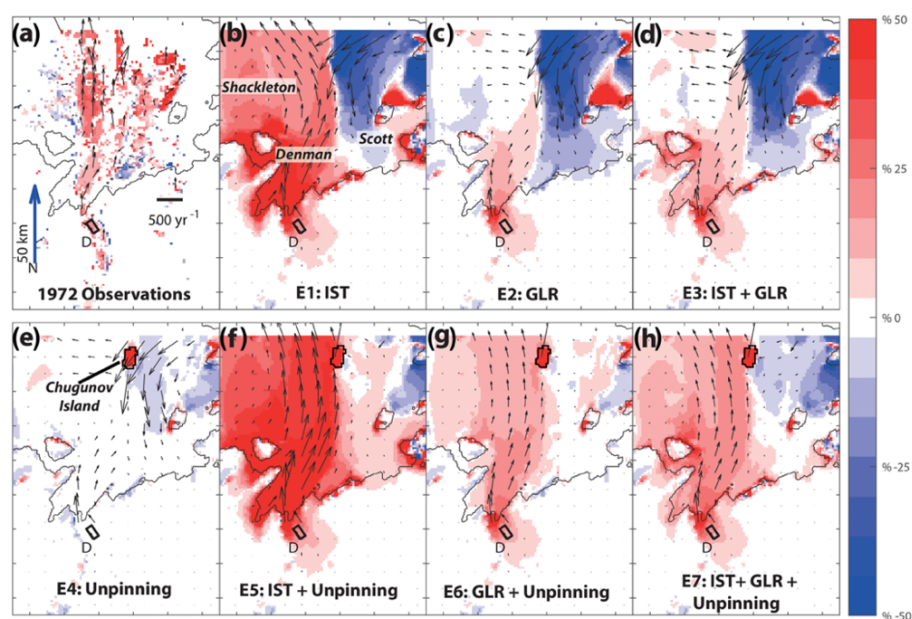


Figure 2.14. Results from *Uá* flow model perturbation experiments revealing the effect of different geometric configurations on ice flow velocity on the Denman Ice Tongue. Each perturbation experiment consisted of combinations of ice shelf thinning (IST), grounding line retreat (GLR) and the unpinning from Chugunov Island. Note panel h which simulated velocities combining IST, GLR and unpinning that are comparable to observations (from Miles et al., 2021).

In addition to BedMachine identifying retrograde slopes beneath major EAIS outlet glaciers (Morlighem et al., 2020), past studies have also pointed towards other internal controls which modulate EAIS mass loss. Dynamical simulations found that the removal of coastal ice (<80 mm of SLR) from ice shelves and outlets draining the WSB would trigger sustained ice mass loss and raise global sea level by 3-4 m (Figure 2.15) (Mengel and Levermann, 2014). One of

the glaciers which actively drains ice from the WSB is Ninnis Glacier. However, significantly less attention has been placed on its recent behaviour, with the last study performed by Massom (2003).

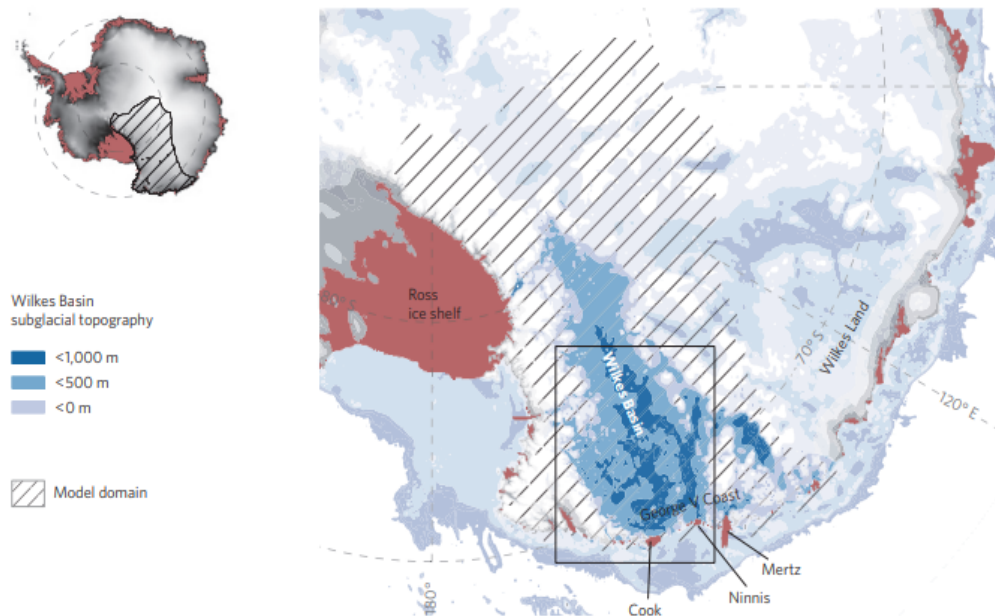


Figure 2.15. Topographical map of the Wilkes Subglacial Basin (WSB), with Cook Glacier, Ninnis Glacier and Mertz Glacier labelled. Subglacial topography displayed inside black box (from Mengel and Levermann, 2014).

2.5. A review of previous work on Ninnis Glacier

Section 1.7 highlights the importance of Ninnis' glaciological setting, with a recent bed topography survey pointing towards its potential susceptibility to MISI (Morlighem et al., 2020). To date, only three studies have exclusively focussed on dynamical changes at Ninnis Glacier (Wendler et al., 1996; Frezzotti et al., 1998; Massom, 2003). Wendler et al. (1996) observed a 110 km terminus retreat and a one-third reduction in the area of Ninnis' tongue between 1912 and 1993, comprising of two major tabular calving events in the early 1950s and between 1980 and 1982. While neighbouring Mertz Ice Tongue doubled in size and advanced by 26 km at a rate of 0.9 m a^{-1} between 1962 and 1993, most of the Ninnis' retreat was observed between 1913 and 1962 before re-advancing at a rate of 910 m a^{-1} between 1963 and 1993 (Figure 2.16) (Wendler et al., 1996). As observations of terminus position changes were only quantified from images in 1913, 1962 and 1993, the nature of Ninnis' calving patterns was not accurately constrained and would require shorter-term (ideally annual) image analysis.

Evidence of Ninnis' tongue undergoing major rifting in 1993 provided the rationale for a remote sensing investigation into shorter-term terminus position changes by Frezzotti et al. (1998). A time-series (1963-1996) of area change for Ninnis' ice tongue was subsequently produced by Frezzotti et al. (1998) (Figure 2.17). Analysis of *in-situ* surveys from the 1979 Deep Freeze Expedition led them to postulate that the earliest calving event in their study occurred in the early 1950s, which led to the detachment of a >1,480 km² tabular iceberg. Landsat, Synthetic Aperture Radar (SAR) and aerial imagery was suggestive of more pronounced retreat from the 1980s onwards, due to a large-scale calving event estimated between 1980 and 1982. Although there was no *in-situ* data that can accurately link calving dynamics to climatic forcing, the study attributed the event to relatively warm mCDW incursion which led to thinning of Ninnis' ice tongue (Frezzotti et al., 1998).

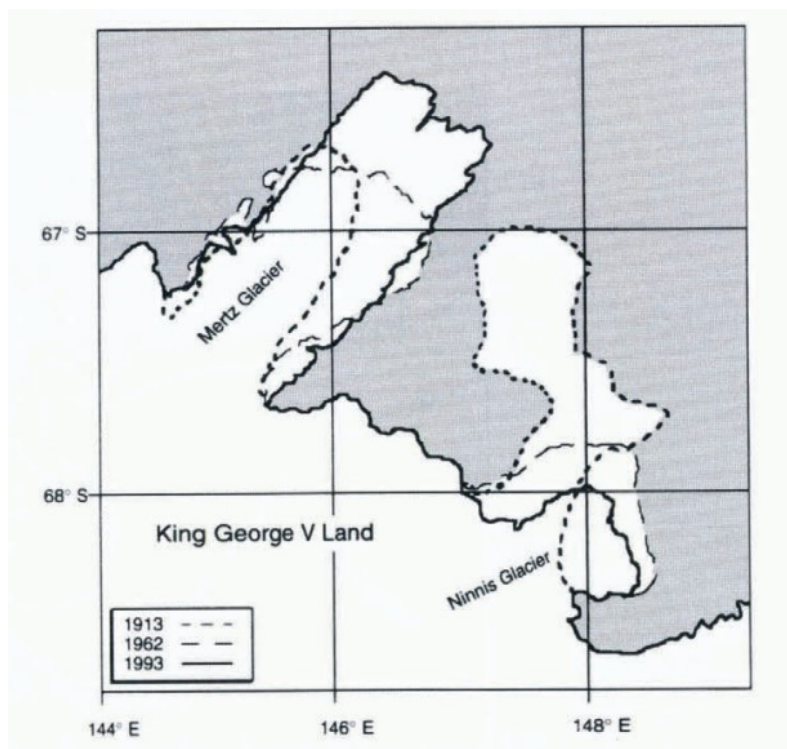


Figure 2.16: Terminus position change and Mertz and Ninnis Glacier tongues (1912-1913, 1962 and 1993) (from Wendler et al., 1996).

The state of Ninnis Glacier was recorded before the 1980s calving event in a 1974 Landsat image, with their interpretations showing a heavily fractured tongue enclosed with high concentrations of MYLI and a down-ice terminus position similar to that in 1913 (Wendler et al., 1998). A re-advance followed immediately after the 1980-1982 calving event, lasting until

the end of the study period in 1996. By this time, Ninnis' tongue was heavily rifted and predisposed to imminent detachment (Frezzotti et al., 1998).

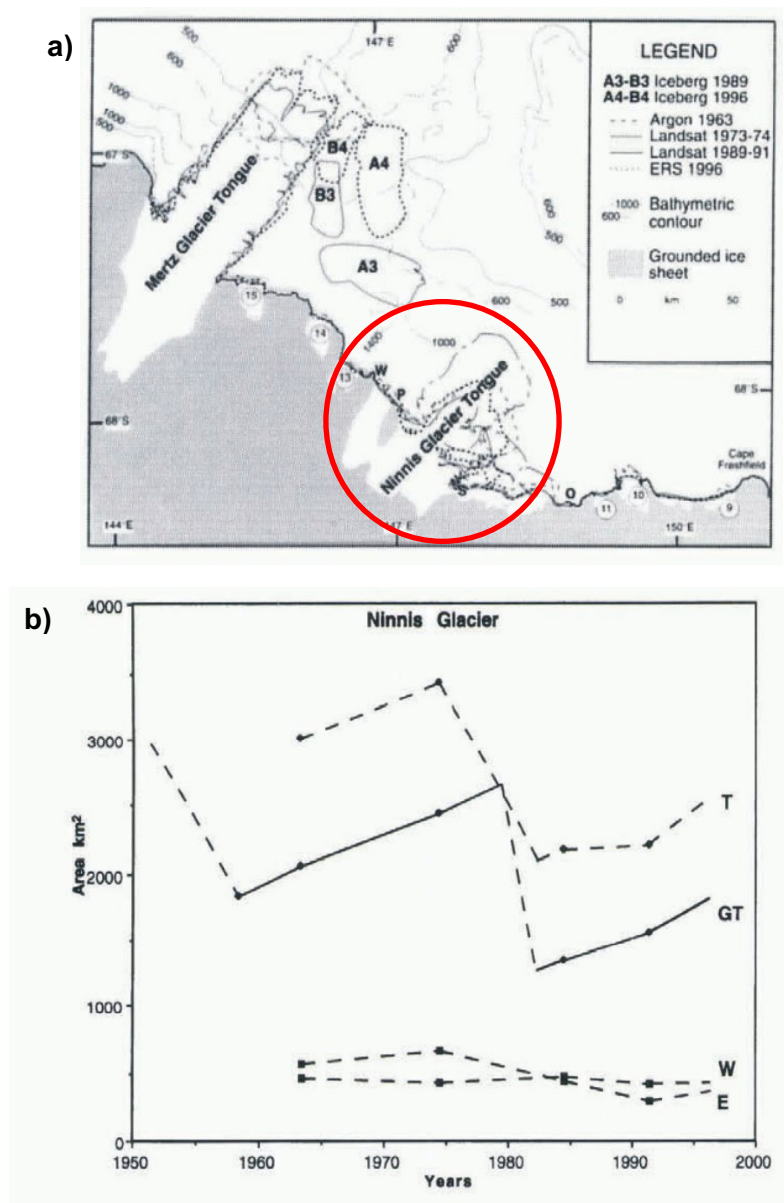


Figure 2.17: (a) Map depicting ice frontal position change and iceberg variations at Mertz and Ninnis Glacier (circled) (b) Area change of the Ninnis tongue (T), central tongue (GT), eastern tongue (E) and western tongue (W) and (b) table of area change for Mertz and Ninnis Glacier tongues (1912-1913, 1962 and 1993) (from Frezzotti et al., 1998).

According to the most recent study of Ninnis Glacier (Massom, 2003), the next major calving event occurred around January 2000. Previous time-series were extended by combining SAR and Advanced Very High-Resolution Radiometer (AVHRR) imagery which captured late 20th-

century to early 21st-century observations of glacier dynamics. The January 2000 calving event culminated in a prolonged period of east-to-west rifting which began pre-1989 and was completed in June 1998 (Massom, 2003). The detachment of a large tabular iceberg followed and remained grounded proximal to the terminus for ~19 months before drifting towards the Ninnis Bank in January 2000. The Ninnis Bank has been referred to as an ‘iceberg trap’, owing to its shallow (~250 m) bathymetry which curtails iceberg drift paths (Domack and Anderson, 1983). This is also known to form extensive, thick (~5 m) sea ice lenses which intercept drifting wind from the east and ice from the west, interfering with polynya formation (Massom et al., 2001; Kushara et al., 2011) (Figure 2.18) (Domack and Anderson, 1983; Frezzotti et al., 1989).

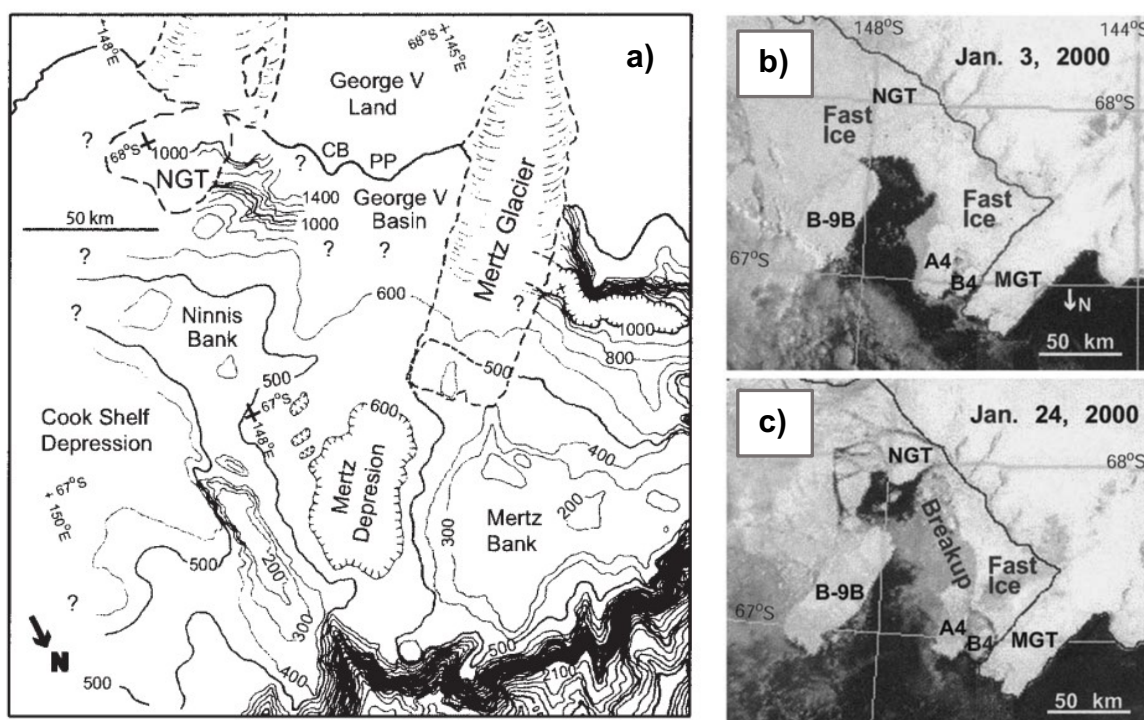


Figure 2.18: (a) Bathymetric map of George V Land depicting banks and depressions offshore of the Ninnis Glacier Tongue (NGT) and Mertz Glacier. (b) NOAA AVHRR images showing changes eventual sea ice break-up in the build-up to the January 2000 calving event (from Massom, 2003).

To summarise, previous work suggests that calving events are estimated to have taken place at Ninnis in the early 1950s, early 1980s and in 2000 (Frezzotti et al., 1998; Massom, 2003), but it is still unclear whether this is part of a natural, predictable calving cycle or if there is any

variability between calving cycles. Furthermore, it is possible that a more recent calving event has taken place. Given the context of recent outlet glacier behaviour in some sectors of the EAIS, more detailed observations are required. Observations should particularly focus on changes in advance rates relative to prior calving cycles and detailed analysis of ice flow velocities. Currently, it is still unknown if calving events from Ninnis result in the loss of dynamically important ice and induce a speed-up of ice up-ice of the grounding line (Fürst et al., 2016).

Chapter 3: Methods

3.1. Introduction

This section outlines the remote sensing framework that was applied to quantify recent glaciological changes at Ninnis Glacier, as previously adopted in similar studies on Antarctic outlet glaciers and ice shelves (Glasser et al., 2011; Holt et al., 2013; Miles et al., 2013). The first section describes the range of image sources obtained and the processing techniques required before performing detailed analysis (section 3.2). This is followed by sections specifying the approach and criteria used for mapping terminus position change (section 3.3) and structural glaciology (section 3.4). The next section (section 3.5) details the methods used to produce a time-series of short-term velocity changes across three key time periods. Finally, secondary datasets obtained to visualise Ninnis' grounding line and produce profiles of bedrock topography and surface elevation are described in section 3.6).

3.2. Image acquisition

3.2.1. Satellite data sources

This study primarily used optical Landsat and Sentinel-2 imagery due to their accessibility, high spatial resolution (10-60 m) and regular coverage, appropriate for mapping long-term changes in terminus position change and structural glaciology for major East Antarctic outlet glaciers (Table 3.1) (Miles et al., 2013; Indrigo et al., 2020; Arthur et al., 2021). Geocorrected Landsat and Sentinel-2 images were obtained from the Google Earth Engine (GEE) *v1.012* Tier 2 Antarctic image archive and filtered at <25 % cloud cover throughout the austral summer (November-March) (Lea, 2018). For years when GEE automatically provided multiple images of Ninnis Glacier which meet the criteria, one image was selected for each annual austral summer based subjectively on the extent of cloud cover surrounding Ninnis' terminus.

Images selected for terminus mapping from the GEE archive included two Landsat 4/5 Thematic Mapper (TM) images (1989 and 1991), 12 Landsat 7 ETM+ images (2000-2004 and 2006-2012), seven Landsat 8 OLI images (2013-2019) and two Sentinel 2A images (2020 and 2021) (Figure 3.1). Large GEE data gaps from Landsat 4-5 Thematic Mapper (TM) imagery initially prohibited inter-annual comparisons of terminus position change between 1989 and 1999. These gaps were filled by obtaining a range of Synthetic Aperture Radar (SAR) images (Table 3.1). This included images from the JERS-1 (1993), ERS-1 (1996) ERS-2 (1998) satellites, all provided by the Alaskan Satellite Facility (ASF), and one RADARSAT-1 mosaic of Antarctica (1997) courtesy of the National Snow and Ice Data Center (NSIDC) (Table 3.1; Figure 3.1e-h). Available SAR scenes provide ideal sources of supplementary imagery for

mapping Antarctic outlet glaciers as they can penetrate cloud cover yet produce high resolution (30 m) images (Massom, 2003). To extend the time series, one ARGON (1963) and one Landsat Multispectral Scanner (MSS) image (1974) were obtained from the USGS Earth Explorer Declassified and Tier 1 Landsat image archives. In addition, a Soyuz Cosmos KATE (1984) aerial image was provided by M. Frezzotti (pers. comm.; see Figure 3.1c). Overall, exactly 22 Landsat, 4 SAR, 2 Sentinel scenes and 1 aerial image was analysed across 30-time steps between 1963 and 2021.

Table 3.1: Overview of satellite and aerial image sources, and their respective spatial resolutions, acquired for terminus and structural mapping Ninnis Glacier.

Image	Dates	Data Source	Spatial resolution (m)
ARGON	August 1963	USGS Earth Explorer Declassified	140 m
Soyuz Cosmos KATE	February 1984	Massimo Frezzotti personal archive	15-30 m
Landsat 1-3 MSS	January 1974	USGS Earth Explorer	60 m
Landsat 4-5 TM	January 1989 and March 1991	Google Earth Engine Tier 2 Image Archive	30 m
JERS-1 SAR	May 1993	Alaskan Satellite Facility (ASF)	18 m (across track) 18 m (along track)
ERS-1/2 SAR	February 1996 / June 1998	Alaskan Satellite Facility (ASF)	26 m (across track) 30 m (along tack)
RADARSAT	1997 Mosaic	National Snow and Ice Data Centre (NSIDC)	8-100 m
Landsat 7 ETM+	February 2000 – February 2012		15 m (Band 8)
Landsat 8 OLI	December 2013 – March 2021	Google Earth Engine Tier 2 Image Archive	15 m (Band 8)
Sentinel 2	November 2020 – March 2021		10 m

A range of image sources enabled quantification of cumulative terminus position change between annual time-steps to produce a long-term time series of terminus position change for Ninnis Glacier. Inter-annual advance and retreat rates were also quantified, constraining the timing of calving cycles whilst distinguishing changes between respective calving cycles.

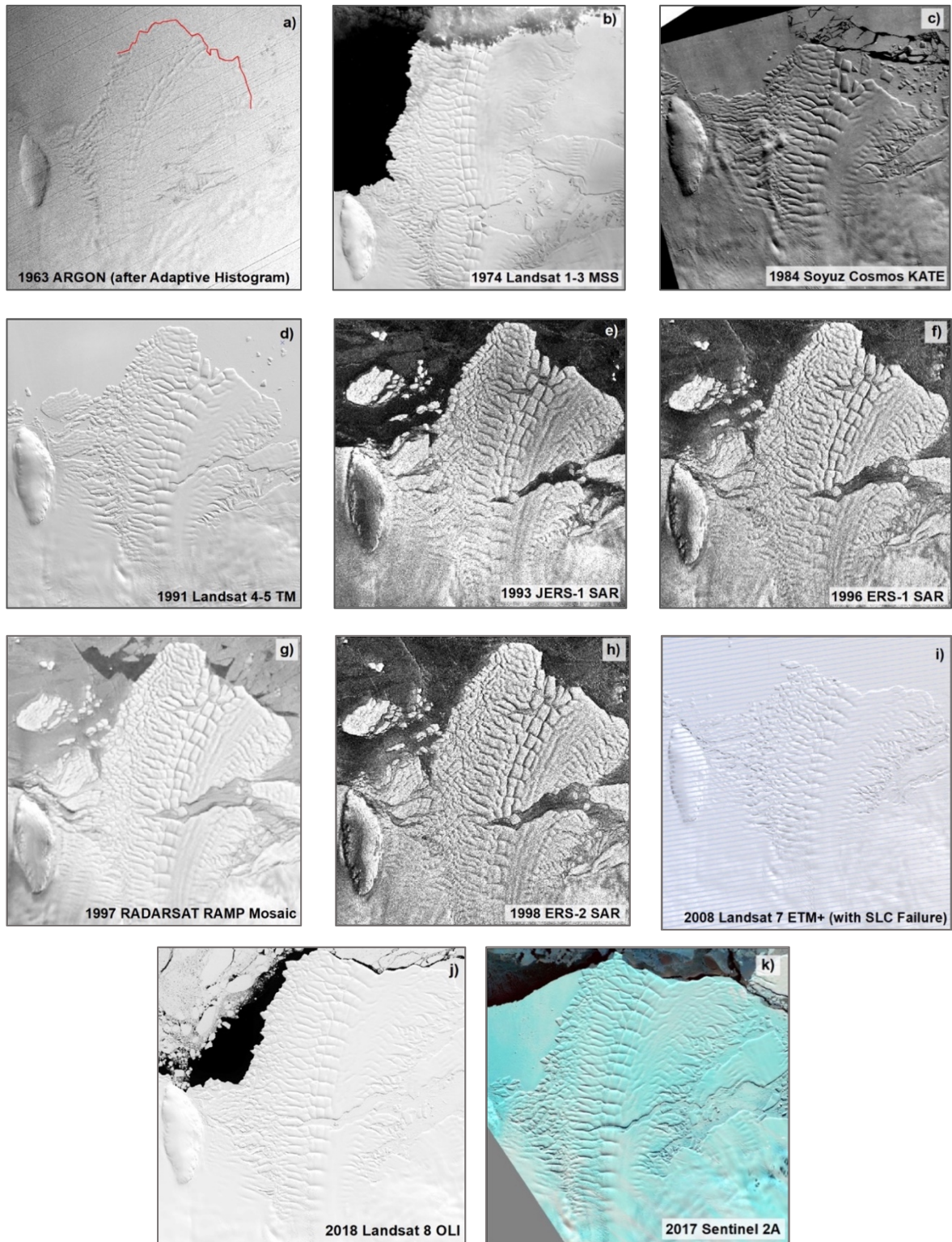


Figure 3.1: Visual example of satellite and aerial images used for delineating terminus position change at Ninnis Glacier. Panel a depicts the post-processed ARGON image using the adaptive histogram method (see section 3.2.2). The red line in panel a depicts where the 1963 terminus was delineated. Panel i shows a zoomed-in sample of a Landsat 7 ETM+ image which is hindered with Scan Line Corrector (SLC) failure.

3.2.2. Satellite data processing and geocorrection

Image quality of the 1963 ARGON image was poor and did not provide a clear outline of the ice tongue. To improve this, an Adaptive Histogram Equalisation method was performed using ArcGIS 10.5 to alter the image contrast to the point in which the terminus could be accurately delineated (Figure 3.1a).

Images unassigned to a projected coordinate system were manually co-registered using the 'nearest neighbour' geocorrection tool on ESRI ArcGIS10.5. This included the 1963 ARGON, 1993 JERS-1, 1996 ERS-1 and 1998 ERS-2 images. Geocorrection was performed by referencing a 2018 Landsat 8 base scene already assigned to the WGS Antarctic Polar Stereographic Projected Coordinate System. This image was deemed suitable for its cloud-free coverage of immovable and stable Ground Control Points (GCPs). This required identification of ice rises and rumples which are clearly distinguishable from surrounding ice (Matsuoka et al., 2015). Typically, up to 30 GCPs would be plotted between assigned and unassigned images (Paul and Andreassen, 2009; Giles et al., 2009), but a lack of widespread ice-free areas proximal to Ninnis Glacier restricted the maximum GCP placement to a maximum of 9 per image. As these were predominantly clustered around Dixon Island and a neighbouring ice rise to its west, the projection of the unassigned image projection would skew once this limit was exceeded and resulted in model errors at around two pixels in scale. Therefore, to determine their suitability for terminus position mapping, geocorrection uncertainty was quantified manually in ArcGIS 10.5.

3.2.3. Error quantification for geocorrected images

A standardised technique, previously used for measuring the processing error for Landsat images, was employed to calculate the errors for newly geocorrected images (Miles et al., 2013; Lovell et al., 2016). Qualitative image analysis was first performed using the ArcGIS 10.5 swipe tool to visualise the alignment of Dixon Island between orthorectified images and the 2018 Landsat base scene. The newly geocorrected images were then layered on top of the base scene to measure the displacement between GCPs in both image layers. A total of 10 GCPs were plotted between each image pair around Dixon Island and surrounding ice rises, allowing the minimum (min), maximum (max) and mean displacement distance between all points to be quantified. The mean displacement represents the geocorrection error, which also used to represent terminus digitisation error (Table 3.2). Quantified geocorrection errors are as follows: ARGON (± 167 m), JERS-1 (± 89.3 m), ERS-1 (± 101.7 m) and ERS-2 (± 113.36 m) (Table 3.2).

Table 3.2: Quantified displacement errors (m) for geocorrected images of Ninnis Glacier.

Year	Satellite image	Min Displacement (m)	Max Displacement (m)	Geocorrection error (m)
August 1963	ARGON	80.4	291	167
May 1993	JERS-1 SAR	43	245.7	89.3
Feb 1996	ERS-1 SAR	55.6	239.9	101.7
June 1998	ERS-2 SAR	54	175.8	113.36

3.3. Terminus position change at Ninnis Glacier

3.3.1. Terminus digitisation

A 58-year time series of terminus position change between 1963 and 2021 was produced using imagery obtained from GEE tier 2 archive. Termini visible in selected cloud-free (<25 %) images were manually delineated using the Google Earth Engine Margin Digitisation Tool (GEEDiT). This provides a freely accessible and efficient means of manually digitising and quantifying terminus change (Lea, 2018). A standardised mapping criteria was applied to account for Ninnis' heavily fractured tongue, surrounding sea ice and amalgamation of grounded icebergs. This defines the terminus as a clear and obvious boundary between consolidated floating ice and calved icebergs, sea ice or open water (Figure 3.2) (Table 3.3).

Cumulative terminus position change was quantified using the single centreline method (Figure 3.3). This was deemed the most suitable approach due to Ninnis' single flow unit which displayed uniform changes in ice frontal behaviour during each calving cycle across the 58-year observational period. It is also the simplest method which measures linear distance change between two terminus boundaries along a point of intersection determined by the centreline (Figure 3.3) (Cook et al., 2005; VanLooy and Foster, 2008). This specific method also assumes that the margin advances and retreats at uniform rates and configurations, allowing detailed comparisons of terminus position between each time-step (Lea, 2018). The centreline was digitised starting down-ice of the grounding line and along the central flow path of Ninnis' ice tongue. Changes in vertices along the centreline were intersected at homogenous breaks in terminus configuration displayed between each annual terminus position shapefile (Figure 3.3).

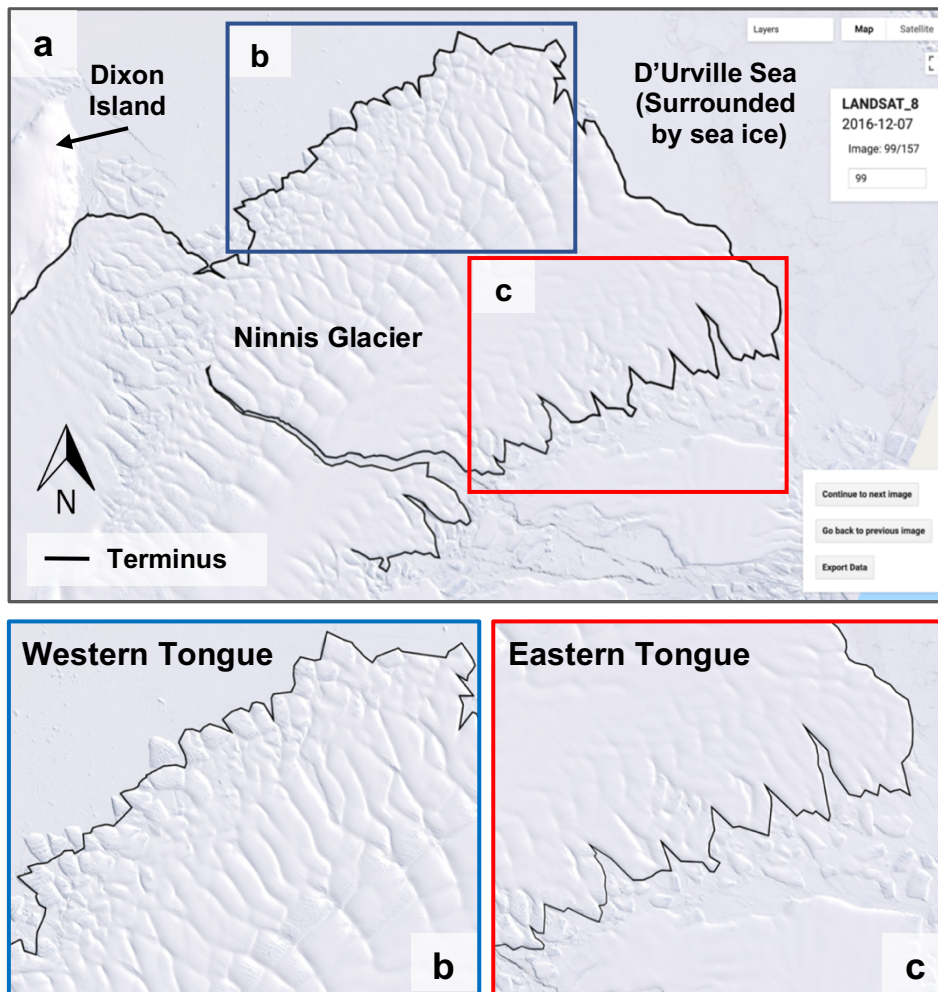


Figure 3.2: Terminus position digitised in GEEDiT from a 2016 Landsat image (a) (Lea, 2018). Note: The blue and red extent indicators in panel (a) are enlarged in panels b and c to illustrate how heavily fractured glacier ice was delineated from surrounding sea ice and icebergs.

Images between 2003 and 2010 yield a 22 % loss in pixel coverage per scene and greater data processing error caused by the Scan Line Corrector (SLC) failure of the Landsat 7 ETM+ sensor in 2003 (Fig.3.1i) (USGS, 2013). However, due to the size of Ninnis' terminus relative to pixel failure, it was still possible to delineate terminus positions between 2003 and 2010. As some Landsat 7 images comprised of full pixel coverage for some portions of the Ninnis terminus, terminus digitisation errors were generally lower compared to those with SLC failure observed directly at the terminus. Overall, no Landsat 7 images were omitted from the investigation, with previous studies successfully delineating termini with sufficient accuracy in images impeded by SLC failure (Moon and Joughin, 2008; Bolch et al., 2010; Miles et al., 2013; Lovell et al., 2016).

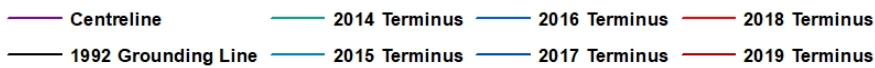
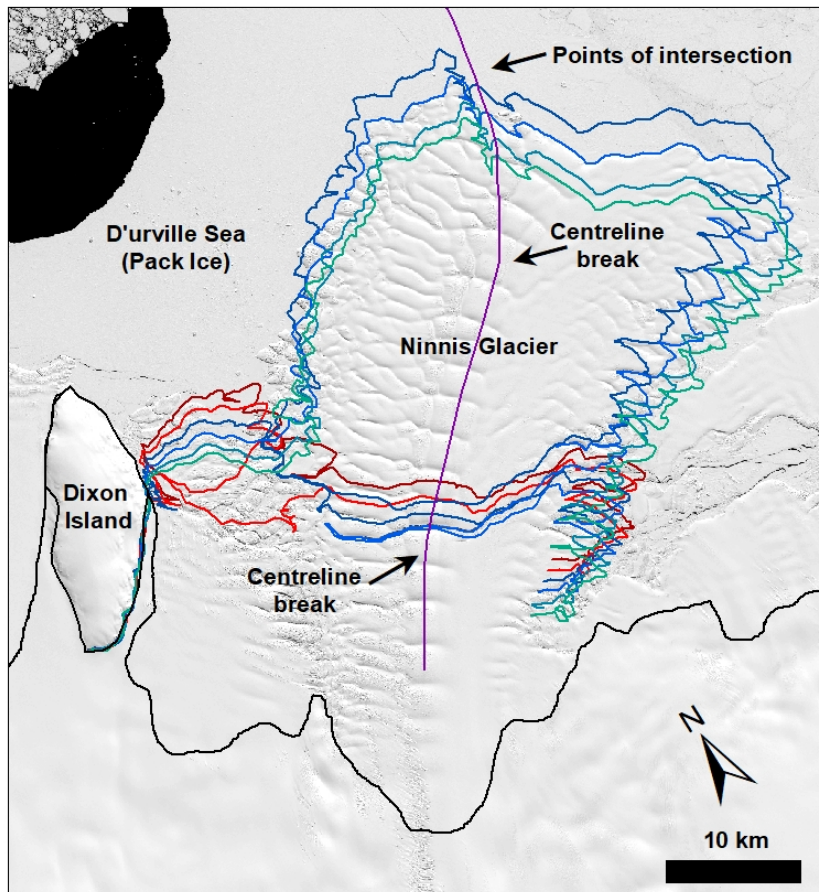


Figure 3.3: Mapped example of the single centreline method applied at Ninnis Glacier (between 2014 and 2018 in this figure). Cumulative terminus position change was quantified between each image pair at points intersecting Ninnis' terminus along the centreline.

3.3.2. Sub-annual terminus position change

High temporal resolution for Landsat 8 (16 days) and Sentinel 2A (6 days) images allowed for further investigations of the terminus following a major calving event in 2018. The standardised mapping criteria was used to digitise termini across 19 cloud-free (<25 %) Landsat 8 and Sentinel images. These were spaced >1 week apart between the 27th of January 2018, immediately after calving, and March 2021 where temporal coverage ended. Cumulative terminus position change was also quantified using the single centreline method (Lea, 2018). This allowed a secondary high-resolution sub-annual time-series of terminus position change to be produced and identify any short-term fluctuations in terminus re-advance or small-scale calving events or retreat phases.

3.3.3. Terminus digitisation error quantification

Ninnis Glacier's heavily fractured and crevassed ice tongue poses difficulties in accurately delineating precise terminus positions across multiple time steps. Thus, digitisation errors need to be quantified to determine the accuracy of the time series of cumulative terminus position change at Ninnis. Typically for 'clean' outlet glacier or ice shelf termini, glacier digitisation error rarely exceeds the pixel size for each respective image (De Beer and Sharp, 2007). For images already assigned to a projected coordinate system, errors were quantified by digitising 10 independent terminus positions for each image and taking the maximum distance between any two digitised termini for each image (Stokes et al., 2006). Overall, errors for projected images are as high as 41.8 m for Landsat MSS, 80 m for Soyuz KATE, 32.9 m for Landsat TM, 113.24 m for RADARSAT, 11.58 m for Landsat ETM+ (without SLC failure) and 15.5 m for Landsat ETM+ (with SLC failure), 8.7 m for Landsat OLI and 5.5 m for Sentinel 2 images.

3.4. Structural glaciological mapping

Structural glaciological features (e.g., crevasses fields, fractures, and rifts) identified across Ninnis Glacier were manually mapped using ArcGIS 10.5 to elucidate any potential relationships between terminus position change and the structural integrity of Ninnis' grounded and floating ice. A standardised mapping approach was adapted from Glasser et al. (2011), Holt et al. (2013) and Arthur et al. (2021) across two epochs. The first epoch consists of five time steps before the 1998 calving event (1989, 1991, 1993, 1996 and 1997) and the second epoch consists of two time steps before the 2018 calving event (2016; 2017), one during (2018) and two after (2019; 2020).


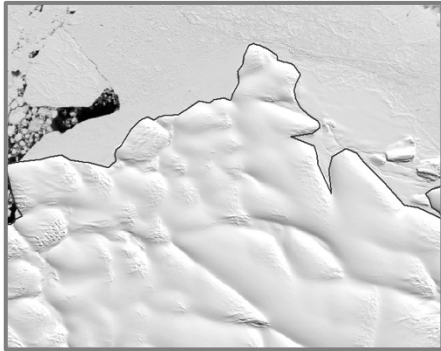
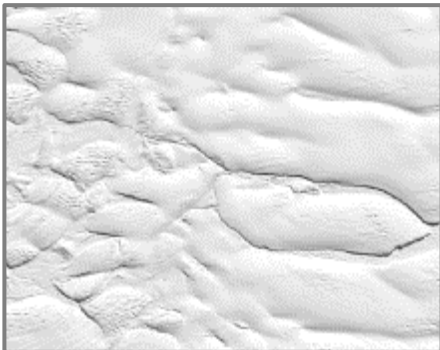

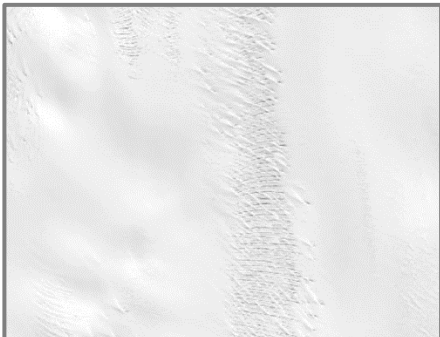
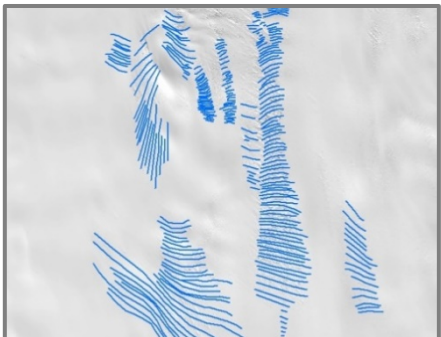
Identification of features was performed at different scales: 1:50,000-1:100,000 for sea ice, rifts and fractures, and 1:25,000-1:30,000 for crevasses. Poor pixel resolution of 1990s SAR images restricted crevasse mapping across Ninnis. Therefore, structural maps generated across the first epoch focussed on visualising the evolution of the central rift system in the build-up to the 1998 calving event. For consistency, a rift map was also produced prior to the 2018 calving event. By mapping rifts, their down-ice displacement was measured to extract independent estimates of ice flow velocity between successive time-steps. This was achieved by dividing the distance between rift endings by the length of time between image pairs as it migrated downstream.


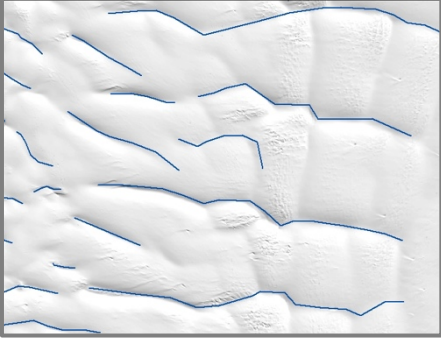
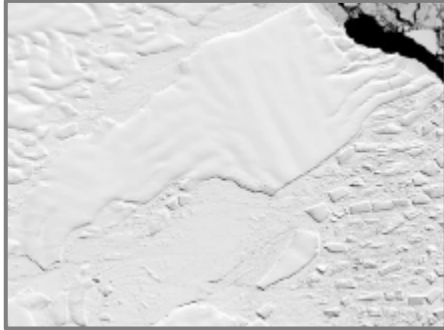

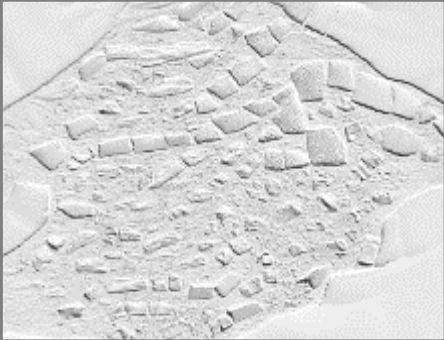

Detailed mapping of rift evolution is important for delineating terminus positions and constraining the timing of calving events upon rift completion (Table 3.3). However,

determining the timing of calving events is unclear as complete detachment is sometimes difficult to ascertain if the calved iceberg remains close to the terminus, following its detachment. For instance, Massom (2003) recorded tabular iceberg formation at Ninnis immediately after the completion of a major rift in June 1998. Following rift completion, the iceberg remained grounded and enclosed in sea ice for 18 months. Yet, the timing of the calving event was described at the point in which the tabular iceberg began drifting in January 2000. This thesis adopts the same criteria as Frezzotti et al. (1998) which constrained timing events based on the detachment of tabular icebergs following rift completion, rather than when the iceberg begins to drift away from the terminus. Rifts are easily distinguishable from crevasses as they often occur as singular fractures perpendicular to ice flow and show a pronounced inter-annual evolution, whilst crevasses are typically clustered and are smaller in size (Table 3.3).

Past studies have identified basal crevasses on the floating portions of major East Antarctic outlet glaciers, perhaps linked to weakened buttressing of grounded ice (Dow et al., 2018; Child et al., 2021; Indrigo et al., 2021). Structural maps produced for images between 2016 and 2020 therefore acknowledge the possibility of basal crevassing on Ninnis' ice tongue, but solely focus on visible surface crevasses. Crevasses have been split into separate zones based upon their location and evolution between 2016 and 2020. Smaller clusters or standalone features have been labelled as 'Other Crevasses' as a measure of accuracy for the spatial distribution of crevassing, despite not necessarily playing an important role in the structural integrity of Ninnis Glacier (Table 3.3).

To complement structural glaciology, Ninnis' complex sea ice regime, consisting of unconsolidated pack ice, landfast sea ice and multiyear landfast sea ice (MYLI), was mapped. Sea ice types are distinguished using a recognised mapping criteria adopted by Giles et al. (2008), Fraser et al. (2012) and Arthur et al. (2021) (Table 3.3). This differentiates areas of sea ice which appear cracked or detached from some portions of the tongue (pack ice) with fastened and consolidated sea ice along the terminus and side of the ice tongue (landfast ice). Areas of visibly thicker ice with rougher surface features observed over multiple years are mapped as MYLI (Table 3.3). In contrast, *mélange* is characterised by assemblages of calved blocks, sea ice and firn and sometimes misinterpreted as MYLI (Giles et al., 2008; Fraser et al., 2012). Additionally other mapped features include areas of extremely low sea ice concentrations (<70 % sea ice cover) and polynyas, which are non-linear open-water exposures found within sea ice (Morales Maqueda et al., 2004) (Table 3.3).

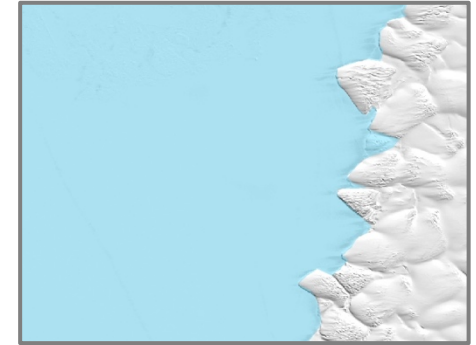
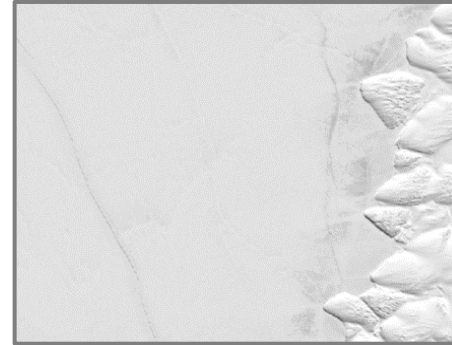
Feature	Identification	Significance	Image example	Mapped image example
Terminus	Clear and obvious boundary between consolidated floating ice and calved icebergs, sea ice or open water. When digitising termini, sea ice was distinguishable from glacial ice due to darker, smoother surface features and open water exposure.	Indicates maximum extent of floating ice tongue and provides important quantitative data when producing a time series of glacier terminus position at multi-decadal resolution.		
Rifts	Evidence of opening initiation and widening and propagation of openings. Typically, perpendicular to ice flow, these can be filled with sea ice, mélange or open water (Indrigo et al., 2020). Completion of rift can be used to define new terminus position.	A pre-cursor to calving, depending on the lateral extent and frequency of rifting. Strain rates can be derived as well as independent velocity measurements (Rignot et al., 2011).		
Crevasses	Light (snow-filled) or dark (open and water filled) linear-curvilinear features. Depending on type, they form either perpendicular or parallel to flow (Glasser and Gudmundsson, 2012). Often found in clusters or zones.	Crevasses form when ice regimes exceed a critical threshold. Open crevasses are indicative of extensional flow (Patterson, 1994). Formed at shear margin at grounding line (Scambos et al., 2009).		

Fractures	<p>Prominent ice shelf indentation typically formed perpendicular and parallel to ice flow. No visible opening. Hence, fractures form a continuum from rifts and are distinguished by their lighter surface (Holt et al., 2013).</p>	<p>Fractures form due to perpendicular ice shelf compression and at the same orientation as up-ice rifting. Also linked to basal channels beneath ice shelves, initiating thinning and ice surface deformation (Dow et al., 2018).</p>		
Calved blocks	<p>Medium-large sized icebergs deriving from ice termini. Can be floating, constrained by sea ice or resting against glacier calving margins. Some remain static for years due to iceberg traps due to coastal bathymetry (Massom, 2003).</p>	<p>Indicator of recent calving events. Thus, sequential images can constrain the timing of detachment. Observing movement and drift of calving blocks used to infer wind regimes, bathymetry and iceberg traps.</p>		
Mélange	<p>An assemblage of sea ice and marine ice, firm, and an amalgamated iceberg (Arthur et al., 2021).</p>	<p>Acts to buttress ice shelves and glacier tongues and modulate major calving event (Massom et al., 2010). Occurs after a succession of major calving events (Miles et al., 2020).</p>		

Pack Sea ice

Easily distinguishable from glacier termini and calving blocks. Sea ice is seen distributed nearby the calving front and is often seen breaking up or with cracks which eventually expose open water.

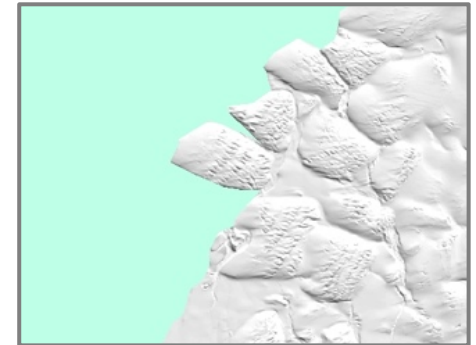
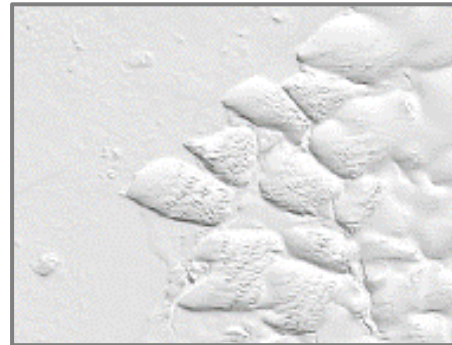
Impacts the Earth's energy balance by modulating heat and moisture exchange between the atmosphere and ocean and high albedo scattering. Act to buttress ice shelves and moderate calving event frequency (Stroeve and Notz, 2018).



Landfast sea ice

Highly consolidated sea ice which is fastened to the edge of ice shelves, whilst constraining newly calved or amalgamated ice bergs. Appears brighter than pack sea ice, with no exposure of open water and has a rougher texture.

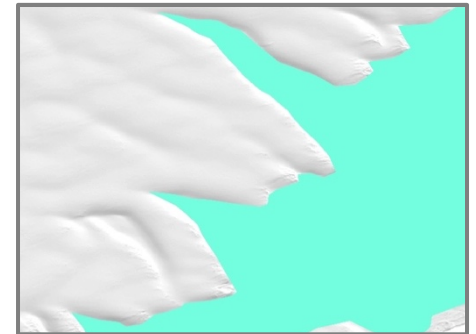
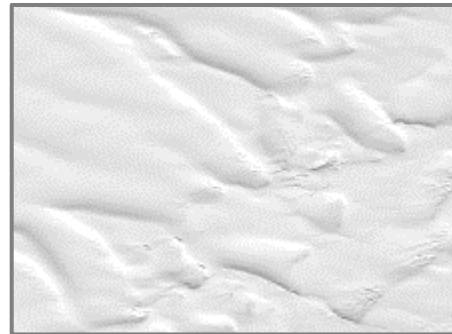
Also impacts ocean stratification, temperature and polynya activity (Miles et al., 2016). Both can be incorporated in mélange (Giles et al., 2008).



Multiyear Landfast Sea Ice (MYLI).

Landfast sea ice which has survived multiple melt seasons and is permanently fastened to ice shelves and trapped ice bergs. Distinguishable because MYLI appears thicker and higher than landfast sea ice.

Forms thick slabs of ice as high as tens of meters which can last decades. Mechanical coupling between MYLI and the Mertz Ice Tongue is argued to have delayed the 2010 calving event by buttressing open rifts (Massom et al., 2010).



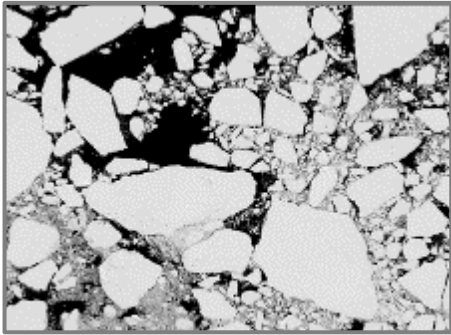
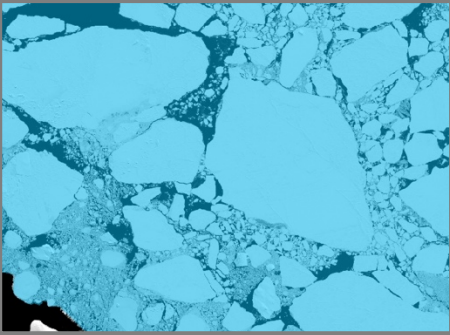
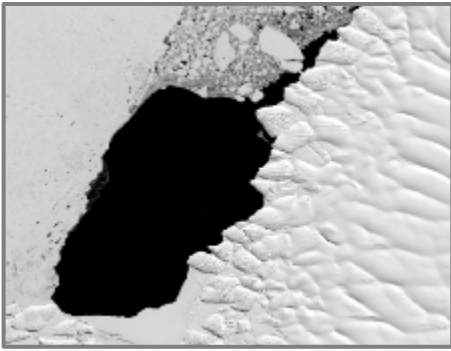
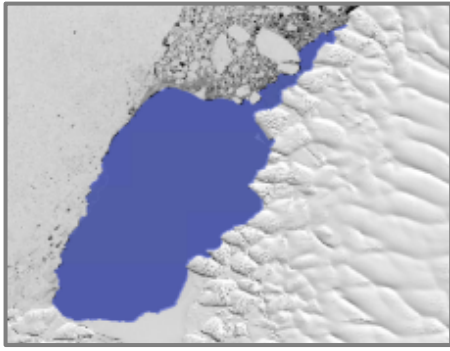
<p><70 % Sea ice cover</p>	<p>Notable clusters of calved blocks and slabs of unconsolidated surrounded by open water. Often widespread across coastlines</p>	<p>Reduces the buttressing force exerted onto ice shelves (Miles et al., 2016). Indicative of warming oceanic and atmospheric conditions and changes in circulation. Can qualitatively suggest sea ice minima (Parkinson and Cavalieri, 2012).</p>		
<p>Polynya</p>	<p>Large openings or pools of ocean water surrounded by winter sea ice. Also referred in literature as “sensible-heat polynyas” and “open-ocean polynyas”.</p>	<p>Polynyas expose the surface of oceans to the overlying atmosphere, initiating heat transfer between them (Campbell et al., 2019). Modulates sea ice variability by impacting water column stratification, preventing CDW incursion (Tamura et al., 2008).</p>		

Table 3.3: Breakdown of the criteria used for identifying and mapping structural glaciological and oceanic features at Ninnis Glacier and their significance. See image sample and mapped image sample columns for visible representation before and after mapping.

3.5. Velocity mapping

Velocity trends were quantified across three key time-periods to produce separate time-series of short-term velocity change at Ninnis Glacier. The first time period (2006-2011) investigates a potential dynamical response of Ninnis before, during and after a localised calving event on the western seaboard of Ninnis' ice tongue before January 2007. According to Rignot et al. (2019), Ninnis Glacier underwent an acceleration following this small calving event in 2008. However, no direct observational evidence was presented to illustrate the magnitude of the break-up and acceleration following this event. To understand whether this event constitutes a period of significant dynamical loss, mean ice flow velocity trends (2006-2011) were quantified from annual mosaics courtesy of the NASA Making Earth System Data Records for Use in Research Environments (MEaSURES) InSAR-Based Antarctic Ice Velocity Map V2 (Rignot et al., 2011). This freely accessible velocity product, comprising of both magnitude (v) and directional ($x;y$) vectors, was generated by compiling multiple interferometric Synthetic Aperture Radar (SAR) image sources including the ALOS PALSAR (2006-2010), ENVISAT ASAR (2007-2009) and RADARSAT-2 (2009-2016) satellites (Rignot et al., 2011). Overall, a 5-year velocity time-series was produced, excluding the 2009-2010 MEaSURES velocity mosaic which was omitted as there was no pixel coverage on the 'floating ice tongue' and 'distal ice tongue' portions of digitised flowlines.

The second time-series quantified ice flow velocity between 2013 and 2018 to assess Ninnis' potential dynamical response in the build-up to and during the 2018 calving event. Velocity data were obtained from annual mosaic products courtesy of the NASA MEaSURES Intermission Time Series of Land Ice and Velocity and Elevation (ITS_LIVE) dataset (Gardner et al., 2019). Mosaics at 240 m spatial resolution were originally processed using feature tracking of prominent structural glaciological features such as rifts visible in Landsat image pairs, produced annually as an averaged velocity product (Gardner et al., 2019). By correlating observed changes in ice flow velocity with terminus position change, it is possible to elucidate whether Ninnis displayed a velocity response in the build-up to calving in 2018, whilst assessing whether floating ice close to the terminus behaved similarly to ice immediately up-ice and down-ice of the grounding line (Arthur et al., 2021). However, the data series stopped beyond 2018, meaning that Ninnis' velocity response following the 2018 calving event could not be examined using ITS_LIVE mosaics.

Given the importance of investigating whether calving triggered an acceleration of both the floating and grounded portions of Ninnis Glacier after the 2018 calving event, an additional dataset was required. Thus, the final time-series quantified the velocity response of Ninnis

Glacier following the 2018 calving event through short-term analysis of ice flow changes from high resolution Sentinel-1 radar imagery between 2018 and 2021. Repeat velocity GeoTiffs were pre-processed via the European Space Agency Sentinel Application Platform (SNAP). Vector processing began by downloading interferometric Wide Swath (IW) Ground Range Detected (GRD) imagery between 2018 and 2021 from the Copernicus Sentinel Hub to provide a 3-year time series of sub-annual ice flow velocity. This comprises image pairs at a 6 or 12-day resolution calibrated by precise orbits from the Sentinel 1 satellite.

Mean annual velocities across all three time periods were extracted along a central flowline (Flowline 1) (Figure 3.4). This was digitised starting 5 km up-ice of the 1992 MEaSURES grounding line and along Ninnis' central flow path until the point of pixel termination of Ninnis' ice tongue (Figure 3.4). Flowline 2 was digitised for the 2006-2011 time-series along the western seaboard of Ninnis' tongue where the small-scale calving event took place (Figure 3.4). Flowline 2, therefore, provides a more accurate representation of localised velocity response on Ninnis' ice tongue relative to Flowline 1. Ice flow velocity changes were examined across different sectors of Ninnis: 5 km up-ice of the grounding line, 5 km down-ice of the grounding line and on the floating ice tongue. The final 5 km of the flowline on the distal portion of Ninnis' ice tongue is representative of velocities closest to Ninnis' terminus. This was performed to determine whether the region up-ice of the grounding line underwent similar trends to that of floating ice before, during and after calving events.

Velocity magnitudes (m a^{-1}) were extracted along the digitised flowlines using processing tools on ArcGIS. Firstly, the 'Geodetic Densify' tool was applied to create new output rasters for the flowlines with densified approximations of geodesic intervals specified at 1 km. Secondly, the 'Feature Vertices-to-Points' tool was applied to input the densified flowlines and produce a new output raster consisting of points generated from vertices generated along the 1 km intervals. Finally, the 'Extract Multivalued-to-Points' tool on ArcGIS Spatial Analyst was applied to extract the raster values at the specified intervals along the flowlines which are automatically recorded in the attribute table attached to the Feature Points output raster. Velocity magnitudes were then processed by converting the values stored in the Attribute table to Microsoft Excel using the 'Table to Excel' tool in ArcGIS. To reduce noise in each velocity time series, erroneous pixels in each sector were omitted if they were >50 % of the mean values within each sector.

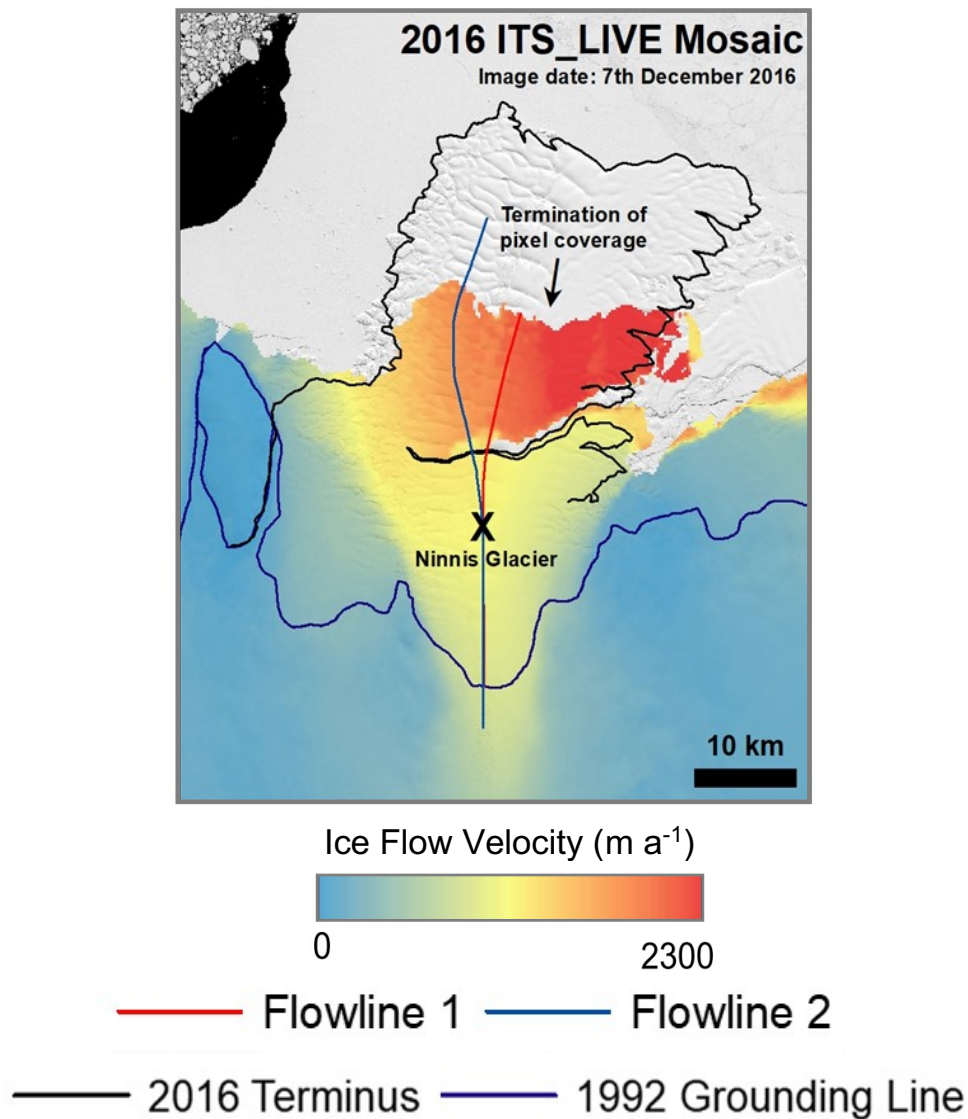


Figure 3.4: December 2016 Landsat 8 image overlain with the 2016 ITS_LIVE velocity mosaic depicting the digitised flowlines used for velocity extraction at Ninnis Glacier. Flowline 1 (red line) was applied across all three time periods (2006-2011, 2013-2018 and 2018-2021), whereas Flowline 2 (blue line) was applied only between 2006 and 2011. Flowline 2 depicts the area in which a localised calving event took place on the western sector of Ninnis' ice tongue in January 2007. X marks the point of divergence between Flowline 1 and Flowline 2.

As Sentinel-1 velocity magnitudes are standardised at meters per day (m d^{-1}), all extracted values were first converted into meters per annum (m a^{-1}) to provide direct comparisons with the ITS_LIVE time-series. Mean monthly velocities were quantified across each designated sector of the flowline in order to determine percentage changes at any given time-step. Annual mean velocities were also quantified to provide direct comparisons of sectoral changes in

velocity magnitude between the Sentinel-1 and ITS_LIVE time-series. Overall, the percentage difference in mean 2018 velocities recorded from the ITS_LIVE and Sentinel-1 datasets were 0.4 % for upstream of the grounding line, 1.4 % downstream of the grounding line, 0.4% across the floating ice tongue and 0.7 % for the distal portion of the ice tongue. This indicates the suitability of comparing both ITS_LIVE and Sentinel-1 velocity datasets at Ninnis Glacier.

3.6. Bed topography, ice surface elevation and grounding line datasets

Bed topography profiles beneath Ninnis Glacier (Figure 1.5) were derived from Bedmap2 (Fretwell et al., 2013) and BedMachine (Morlighem et al., 2020) products. Bedmap2 comprises 1 km² grid cells depicting ice thickness, surface elevation and subglacial bed topography of Antarctica. BedMachine used 500 m horizontal resolution mass conservation to refine estimates of ice thickness and bed topography from Bedmap2 (Figure 1.5a;c). An additional profile was produced to depict spatial changes in Ninnis' ice surface elevation relative to its subglacial topography, courtesy of the 8 m Reference Elevation Model of Antarctica (REMA) (Figure 1.5b). The REMA dataset was processed from stereophotogrammetric DEMs from <1 m resolution optical satellite image pairs and vertically calibrated using radar and laser altimetry data (Howat et al., 2019). Profiles for surface elevation and bed topography were expressed along a newly digitised 120 km flowline, emanating 80 km upstream from the 1992 grounding line along the central flow of Ninnis Glacier (Figure 1.5). This extended flowline differs to those shown in Figure 3.4 as it extends further up-ice and allows the widespread changes in bedrock topography and ice thickness to be visualised. Profiles were processed using the 'Geodetic Densify', 'Feature Vertices-to-Points' and 'Multivalued-to-points' extraction tools on ArcGIS.

To complement terminus position, structural glaciological and velocity mapping, the MEaSURES grounding line dataset was obtained from the NSIDC in attempt to visualise changes in grounding line position at Ninnis Glacier (Rignot et al., 2011). The dataset compiled various SAR interferometric satellite data (e.g., ERS-1/2, RADARSAT-1/2 and ALOS PALSAR) to produce a time-series of grounding line between 1992 and 2014 for the whole of Antarctica. However, only one grounding line SHP file from 1992 was available for Ninnis and was used as a quantitative metric to determine changes in terminus position relative to Ninnis' 1992 grounding line position.

Chapter 4: Results

4.1. Introduction

This chapter presents the results generated from the methods detailed in Chapter 3. Section 4.2. presents the key observations from the 58-year time-series of terminus position change at Ninnis Glacier and is split into three sub-sections. Sub-section 4.2.1 quantifies change in the build-up to 1974 and 1998 calving events, whilst also presenting the image analysis criteria for constraining the 1974 calving event. Section 4.2.2 quantifies terminus position change in the build-up to the 2018 calving event (1998-2018), whereas the section 4.2.3 quantifies sub-annual (monthly) terminus position change following the 2018 calving event.

Detailed spatial and structural glaciological maps of Ninnis Glacier are presented in Section 4.3. This focusses on the structural evolution of Ninnis Glacier before the 1998 calving event (4.3.1), the structural evolution of Ninnis Glacier pre and post 2018 calving event (4.3.2) and the extent and distribution of sea ice offshore of Ninnis Glacier (2016-2020) (4.3.3). Section 4.4 examines short-term trends in ice flow velocity across Ninnis Glacier at three key time periods: before, during and after a localised calving event in 2007 (2006-2011), before and during the much larger 2018 calving event (2013-2018) and after the 2018 calving event (2018-2021).

4.2. Terminus position change

A 58-year time-series of terminus position change captures three major calving events at Ninnis Glacier between 1963 and 2021 which occur at a 20 to 25-year periodicity (Figure 4.1; 4.2). This is characterised by (re)advance phases which culminate in the detachment of large tabular icebergs, retreating to a similar positions up-ice, 28, 29 and 25 km downstream of the 1992 grounding line position, respectively. Cumulative terminus position change and quantified (re-) advance rates (m a^{-1}) are presented for each successive time step in Table 4.1.

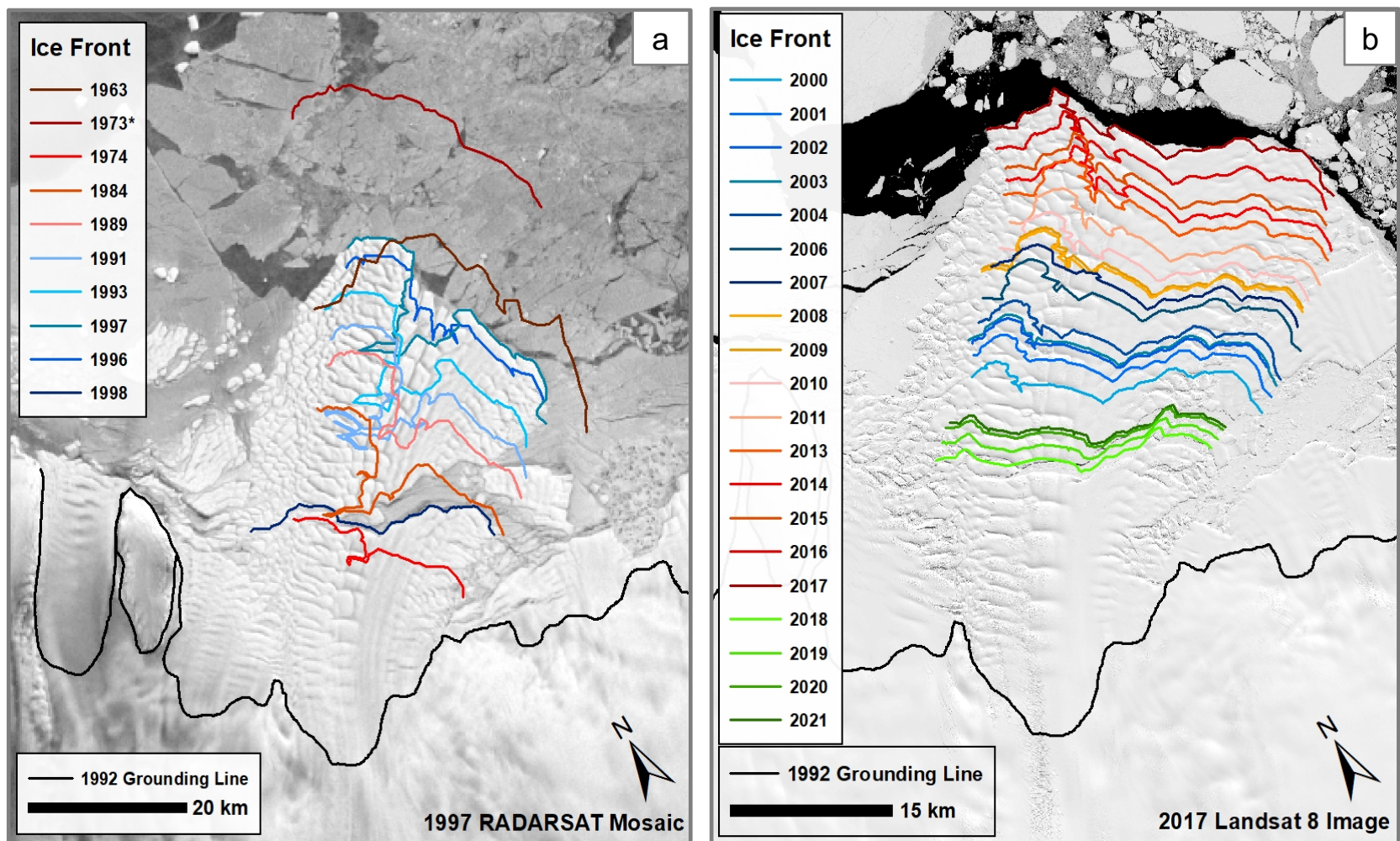


Figure 4.1: Terminus positions for Ninnis Glacier digitised from various satellite and aerial images between 1963 and 1998, overlain on the 1997 RADARSAT RAMP Mosaic (a), and between 2000 and 2021, overlain on a 2017 Landsat 8 image (b). Note the extrapolated early 1970s terminus position from the 1974 Landsat MSS image, labelled 1973* for clarity, in panel 1 and the 2018 calving event in panel b.

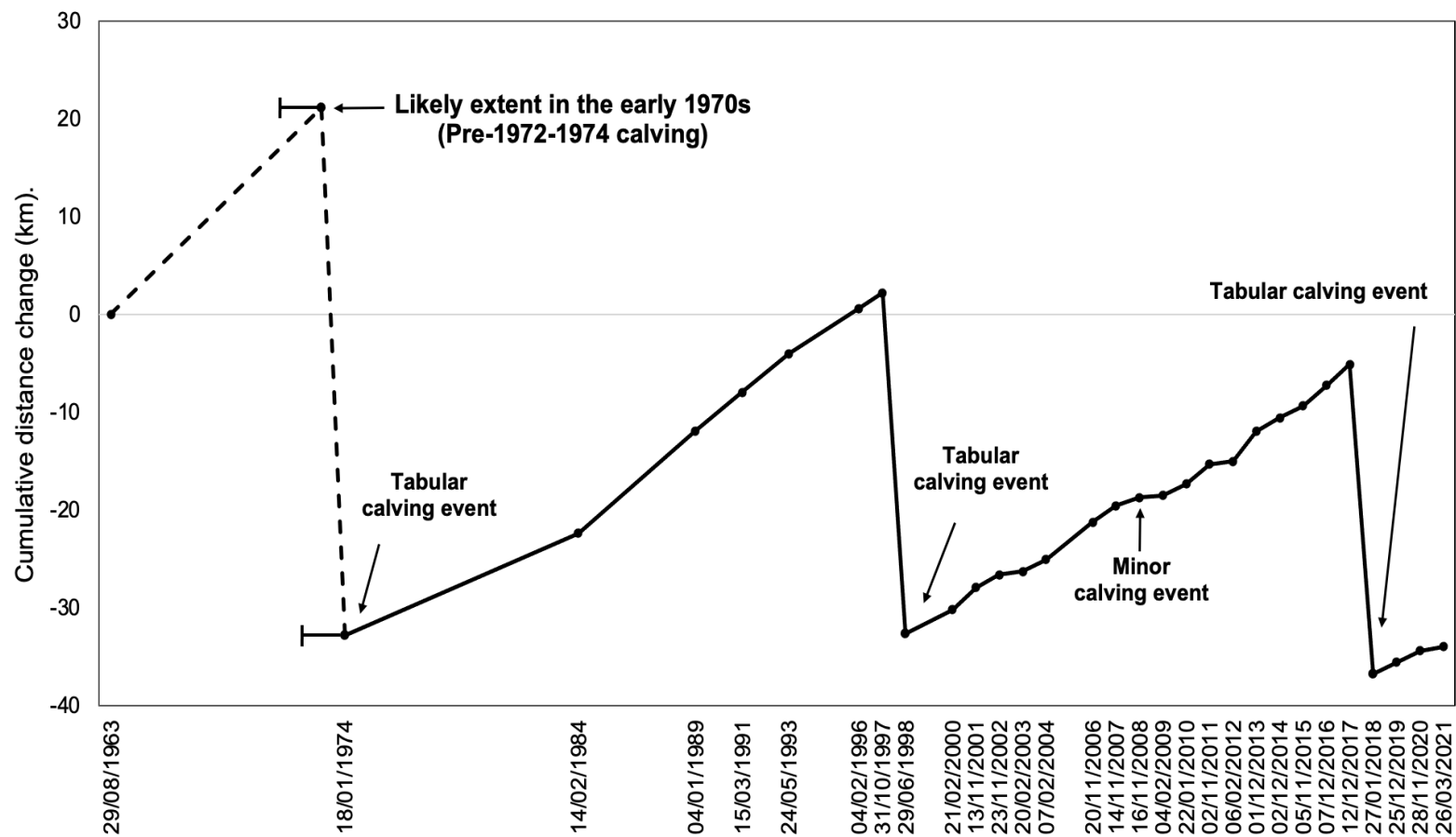


Figure 4.2: Annotated time series of cumulative terminus position change (km) for Ninnis Glacier between 1963 and 2021, relative to first measurement in 1963. Note the likely terminus position extent before the calving event estimated between 1972 and 1974. This position was extrapolated based on the fact that the tabular iceberg in the Landsat MSS image was 54 km down-ice from the mapped 1974 terminus.

Table 4.1: Cumulative ice front advance (km), error (m) and estimated (re-)advance rates (km a⁻¹) at Ninnis Glacier between 1963 and 2021.

From (Date)	To (Date)	No of Days	Ice Front Advance (km)	Error (m)	Estimated Advance Rate (km a ⁻¹)
29/10/1963	18/01/1974	3,734	Calving event estimated between 1972-1974		
18/01/1974	14/02/1984	3,679	10.45	± 41.8	1.04
14/02/1984	04/01/1989	1,786	10.18	± 80	2.08
04/01/1989	15/03/1991	800	3.94	± 32.9	1.8
15/03/1991	24/04/1993	771	4.54	± 32.9	2.15
24/04/1993	04/02/1996	1,016	4.6	± 89.3	1.65
04/02/1996	31/10/1997	635	1.59	± 101.7	0.91
20/06/1998		Calving event			
20/06/1998	21/02/2000	611	2.45	± 113.36	1.46
21/02/2000	13/11/2001	631	2.26	± 11.58	1.31
13/11/2001	23/11/2002	375	1.33	± 11.58	1.29
23/11/2002	20/02/2003	89	0.3	± 11.58	1.23
20/02/2003	07/02/2004	352	1.23	± 15.54	1.28
07/02/2004	20/11/2006	1,017	3.79	± 15.54	1.36
20/11/2006	14/11/2007	359	1.68	± 15.54	1.71
14/11/2007	16/11/2008	368	0.86	± 15.54	0.85
16/11/2008	04/02/2009	80	0.19	± 15.54	0.87
04/02/2009	22/01/2010	352	1.15	± 15.54	1.19
22/01/2010	02/11/2011	649	2.03	± 15.54	1.14
02/11/2011	02/06/2012	213	0.3	± 15.54	0.51
02/06/2012	02/12/2013	548	3.06	± 8.71	2.04
01/12/2013	02/12/2014	366	1.38	± 8.71	1.38
02/12/2014	05/11/2015	338	1.2	± 8.71	1.3
05/11/2015	07/12/2016	398	2.12	± 8.71	1.94
07/12/2016	12/12/2017	370	2.13	± 8.71	2.1
27/01/2018		Calving event			
27/01/2018	28/11/2019	670	1.23	± 8.71	0.67
28/11/2019	28/11/2020	366	1.18	± 5.53	1.18
28/11/2020	26/03/2021	118	0.42	± 5.53	1.3

4.2.1 Terminus position change (1963-1998)

The first calving event, depicted in a 1974 Landsat MSS image reveals the completion of a major transverse rift and detachment of a large ca.1,450 km² iceberg. The western side of the terminus, which remained in contact with the iceberg, is located within an active shear zone (labelled Western Shear Zone in Figure 4.3) containing assemblages of smaller icebergs enclosed in MYLI (Figure 4.3; 4.4). However, as no imagery exists of the Ninnis tongue between 1963 and 1974, the precise date of detachment could not be constrained. This poses challenges in speculating the year in which the rift completed and initiated a major calving event. Considering the presence of MYLI in the 1974 Landsat imagery, it is speculated that rift completion could have taken place anytime between 1972 and 1974 when open water was present within the rift.

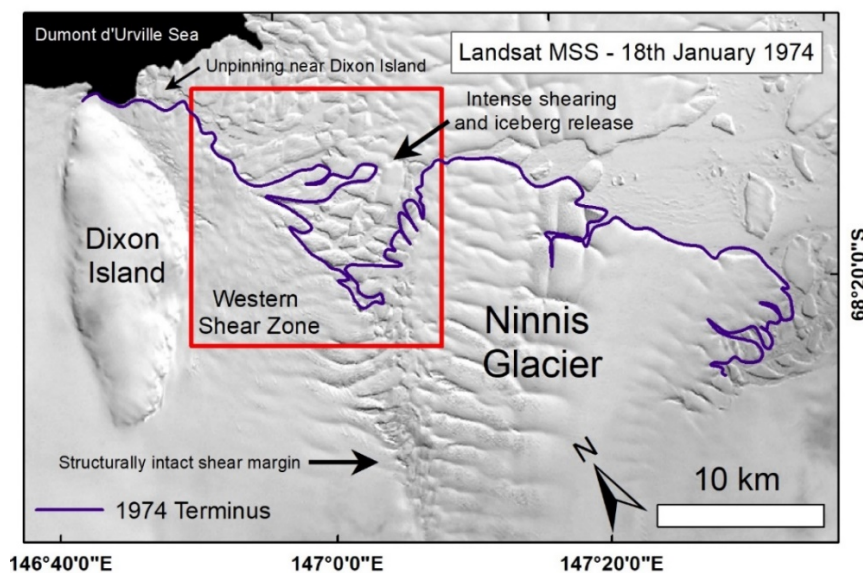


Figure 4.3. Landsat MSS image showing the newly delineated 1974 terminus position. Note the expansive MYLI within an area of intense shearing, labelled “Western Shear Zone” (within the red extent indicator) which enclosed small icebergs. Delineation between the tabular iceberg and 1974 terminus was made in accordance with the mapping criteria in Table 3.3 which accounts for differences in floating ice, icebergs and sea ice.

Although impeded by cloud cover, the 1974 Landsat MSS image roughly depicts a maximum offshore position for the tabular iceberg (Figure 4.4). Given the image gap between 1963 and 1974 prohibiting Ninnis’ maximum extent from being accurately delineated, an estimated terminus position for the early 1970s has been extrapolated. This was delineated based on the knowledge that the iceberg in the 1974 Landsat image was positioned 54 km down-ice from the mapped 1974 terminus (Figure 4.1; 4.2; 4.4).

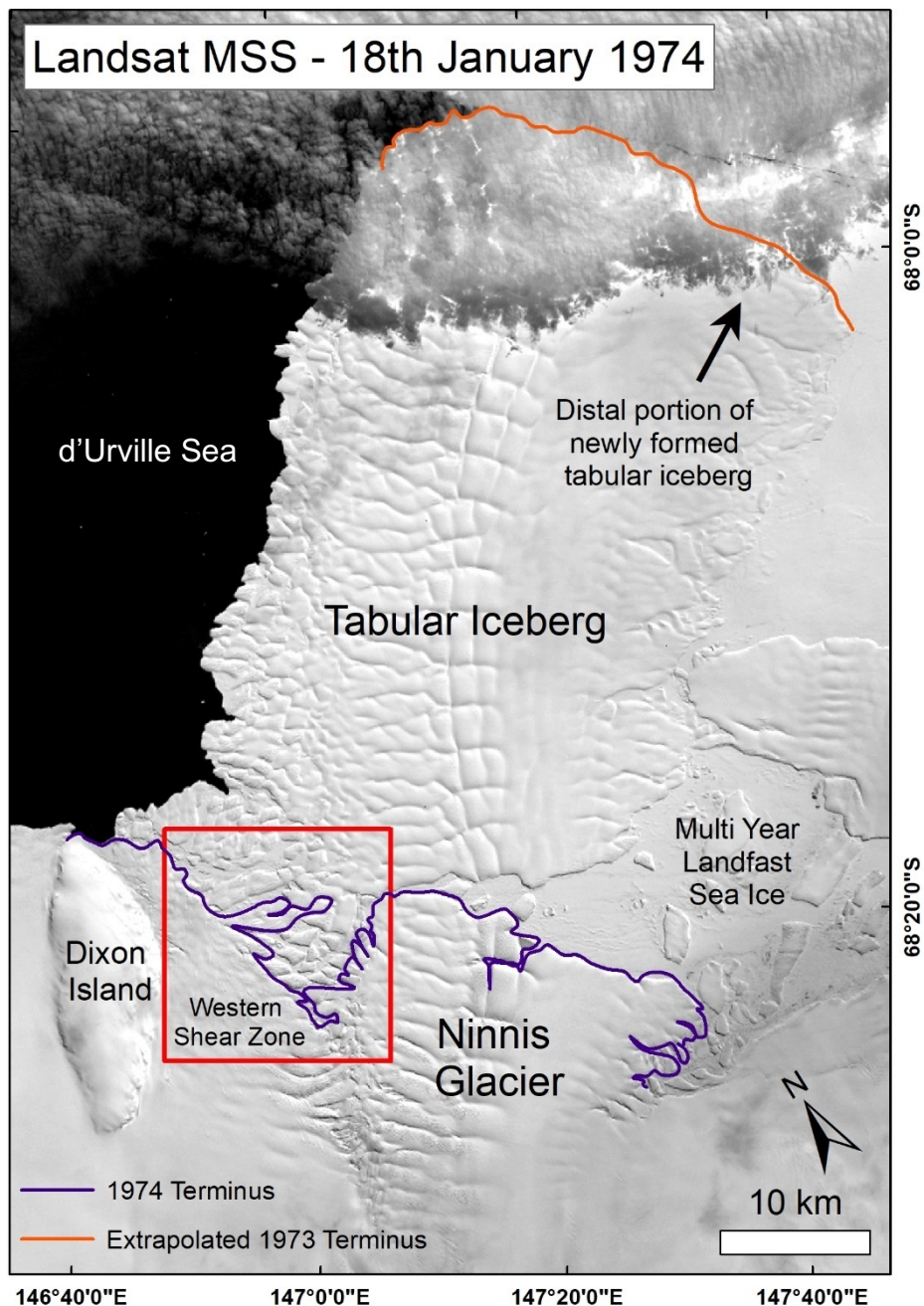


Figure 4.4: Landsat MSS image for 18th January 1974 used extrapolate an early 1970s terminus position (labelled 1973). The red inset represents the area used for structural analysis of the shear zone used to constrain the 1974 calving event (See Figure 4.3). Note the assemblage of MYLI which constrains calved icebergs within the shear zone and conceals obvious detachment of the tabular iceberg. The extrapolated '1973' terminus position is mapped 54 km down-ice of the 1974 terminus where the distal portion of the tabular iceberg is partially visible from cloud cover.

Between 1974 and 1996 Ninnis re-advanced by ~33 km at a mean rate of 1,500 m a⁻¹ (Table 4.1), exhibiting no discernible changes in terminus configuration indicative of major calving events (Figure 4.1a). A slow-down in advance estimated at 917 m a⁻¹ occurred between 1996 and 1997, immediately before the next recorded calving event in 1998 (Table 4.1; Figure 4.5). The second calving event took place between May and June 1998, marked by the detachment of a large ~780 km² tabular iceberg (Figure 4.5). This formed a new terminus position ~29 km down-ice of the 1992 grounding line position and <1 km further advanced than Ninnis' 1974 position (Figure 4.1a; 4.5).

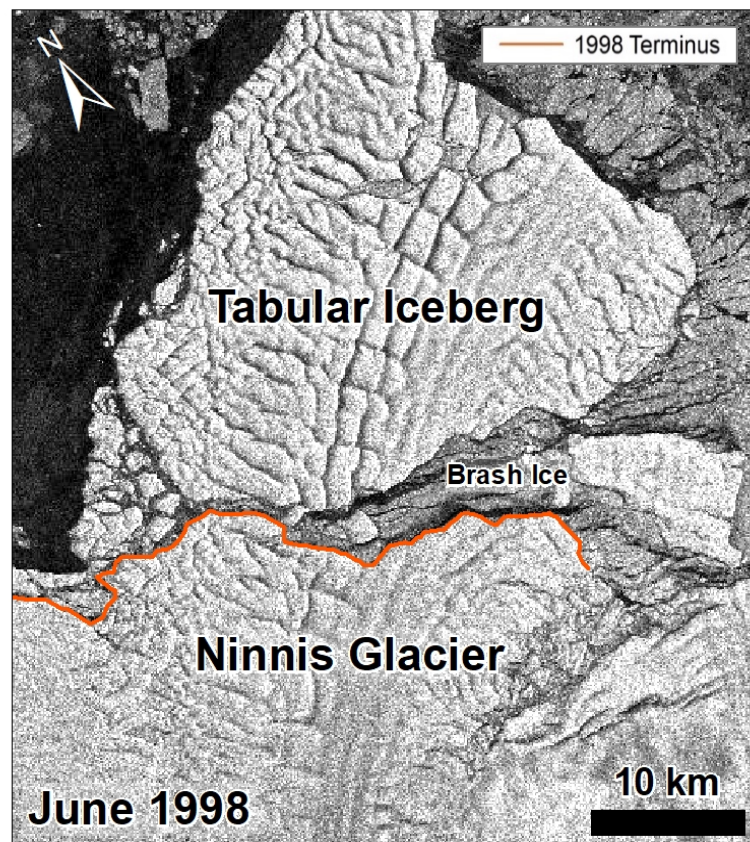


Figure 4.5: Map visualising the completion of central rift system and subsequent tabular calving event in the June 1998 ERS-2 SAR image. Note the brash ice proximal to the newly formed terminus and the eastern side of the tabular iceberg.

4.2.2 Terminus position change (2000-2018)

Between 1998 and 2006, the newly formed terminus re-advanced at an average rate of 1,350 m a⁻¹ (Figure 4.1b; 4.2; Table 4.1), with no evidence of smaller calving events at the terminus. However, in February 2004 a 10 km-long protruding section of ice detached from its pinning point at Dixon Island. This remained partially attached to the western seaboard of Ninnis'

heavily fractured ice tongue and was pre-disposed to imminent calving (Figure 4.6). By January 2007, the 10 km-long section of ice fully detached from Ninnis' ice tongue along with an assemblage of smaller sized icebergs which extended across the Ninnis' western tongue. Although the icebergs remained enclosed in sea ice, calving of small-scale icebergs persisted until January 2008 (Figure 4.6 c-f).

The 30 km² iceberg, which calved in 2007, is substantially smaller than that produced from large-scale tabular calving events in the early 1970s and in 1998 (Figure 4.4; 4.5). However, despite its small-scale, the localised calving event coincided with an 89 % decrease in the average terminus advance rate between 2007 and 2008. This marked the slowest cumulative advance phase since between 1974 and 1984 (Table 4.1). Exceptionally low advance rates persisted between 2007 and 2012, with average values 47.8 % lower than that between 2006 and 2007. Between 2012 and 2013, following a slow 5-year advance phase averaging 900 m a⁻¹, terminus advance rates increased and returned to within 18 % of that recorded in 2006-2007 (Table 4.1).

In the build-up to the next major calving event at Ninnis Glacier, which took place in January 2018, the average advance rate between 2012 and 2017 was 45 % higher than pre-2012 averages (Table 4.1). During this period, Ninnis advanced at rates among the highest across the entire 58-year time-series and the fastest since between 1984 and 1993 (Table 4.1). Unlike the period immediately before the 1998 calving event (1996-1997), advance rates recorded from between 2015 and 2017 were considerably higher (>2,100 m a⁻¹) (Table 4.1). In January 2018, 20 years after its last major calving event, a large ~811 km² tabular iceberg calved from Ninnis (Table 4.1) (Figure 4.1b; 4.2; 4.7). This remained grounded directly in front of the terminus until January 2021 before drifting towards the Ninnis Bank (Figure 1.4). This most recent calving cycle is notably 4 years shorter than the previous one, forming a terminus position <4 km up-ice from the previous post-event terminus position in 1998, and 25 km down-ice of the 1992 grounding line (Table 4.1). This represents Ninnis' most landward position recorded (Figure 4.1b; 4.2).

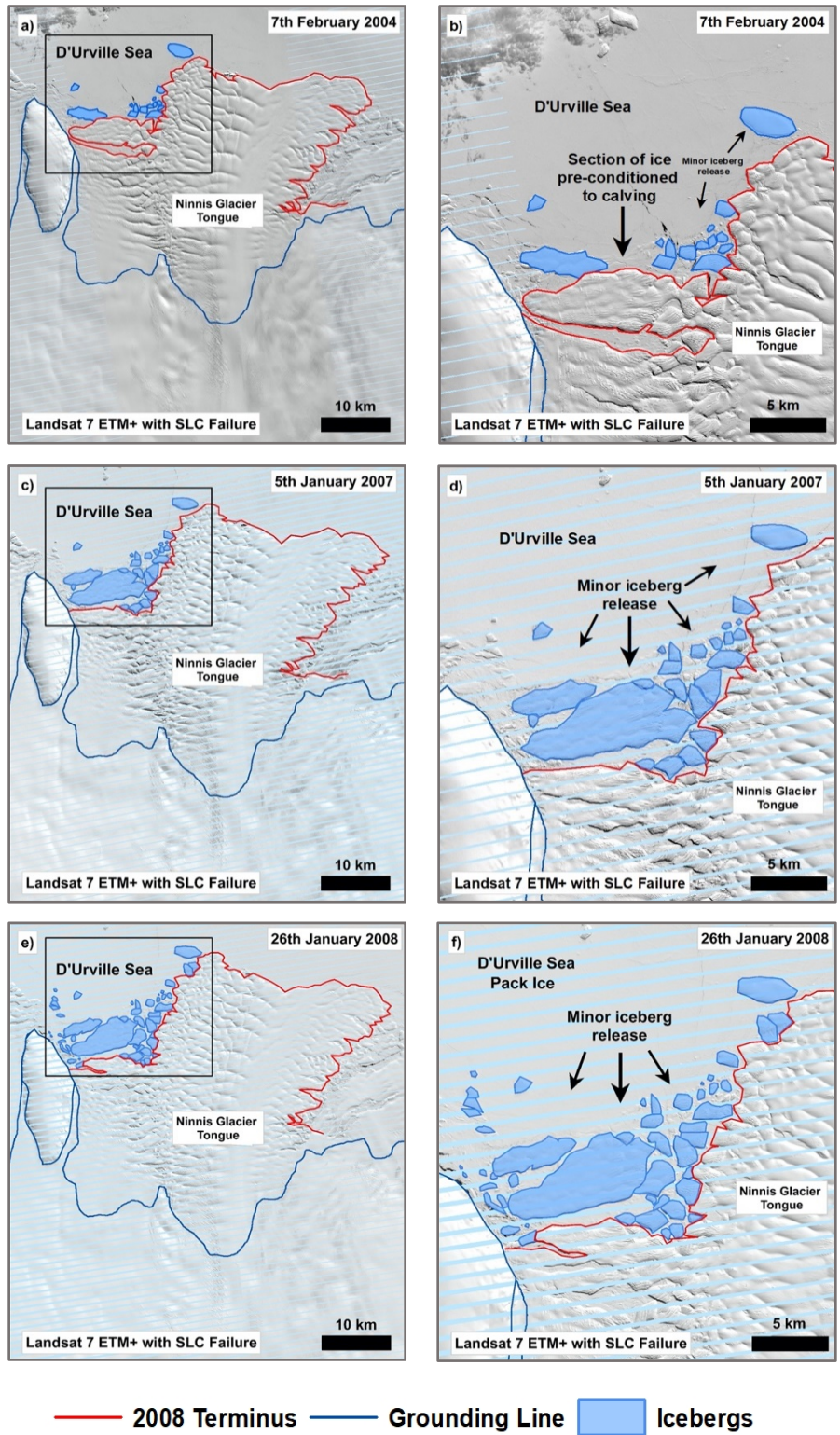


Figure 4.6: Mapped extent of the small-scale calving event observed between on Ninnis' western tongue break-up event of Ninnis in (a;b) February 2004, (c;d) January 2007 and (e;f) January 2008. The black extent indicator in panel e refers to panel 'f' which depicts the each of the mapped icebergs. SLC failure in the Landsat ETM+ images are shown with faint blue lines.

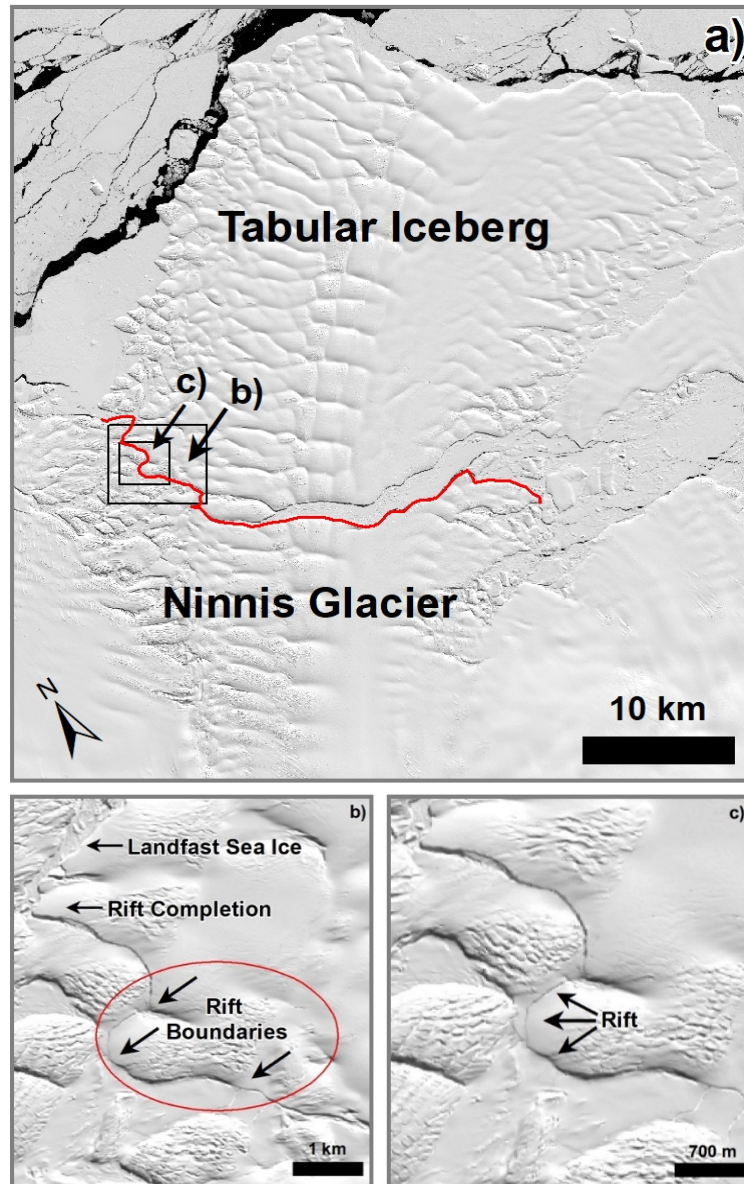


Figure 4.7: Map visualising the completion of central rift system and subsequent calving tabular calving event in the January 27th 2018 Landsat 8 image. The black extent indicators in panel a refer to panels b and c (below) which depict the rift boundaries used to delineate a new terminus position and constrain the 2018 calving event at Ninnis Glacier.

4.2.3 Sub-annual terminus position change (2018-2021)

Figures 4.8 and 4.9 outline the short-term changes in cumulative terminus position digitised between January 27th 2018 (following the 2018 calving event) and March 26th 2021. During this period, Ninnis re-advanced at a comparatively slower rate (700 m a^{-1}) than the post-1998 calving re-advance ($1,500 \text{ m a}^{-1}$ between 1998 and 2000) (Figure 4.1a; Table 4.1; 4.2). Cumulative terminus position change was linear between January 2018 and November 2020, while two time-periods (21st - 28th February 2018 and 6th – 15th December 2018) exhibited negligible retreats in terminus position (-0.02 km and 0.01 km). However, analysis of satellite imagery provided no direct evidence of small-scale calving events directly at the terminus to account for this retreat (Table 4.2) (Figure 4.8; 4.9). This coincided with high sea ice concentrations surrounding the newly formed terminus which persisted for 2-years following the major calving event.

Table 4.2: Summary table of cumulative ice front re-advance (m) and estimated re-advance rate (km a^{-1}) between 27th of January 2018 and 26th of March 2021. Note the periods of slight retreat observed between 27/02/2018 – 28/02/2018 and 06/12/2018 – 15/12/2018.

From (Date)	To (Date)	No of Days	Ice Front Re-advance (km)	Estimated Re-advance Rate (km a^{-1})
27/01/2018	21/02/2018	25	0.17	2.42
21/02/2018	28/02/2018	7	-0.02	-1.07
28/02/2018	09/03/2018	9	0.03	1.40
09/03/2018	20/11/2018	256	0.90	1.24
20/11/2018	06/12/2018	16	0.06	1.46
06/12/2018	15/12/2018	9	-0.01	-0.60
15/12/2018	01/02/2019	48	0.16	1.23
01/02/2019	25/12/2019	327	1.08	1.20
25/12/2019	17/01/2020	23	0.14	2.22
17/01/2020	18/02/2020	32	0.11	1.59
18/02/2020	16/11/2020	272	0.92	1.24
16/11/2020	28/11/2020	12	0	0
28/11/2020	03/01/2021	36	0.18	1.82
03/01/2021	13/01/2021	10	0	0
13/01/2021	23/01/2021	10	0.03	1.17
23/01/2021	06/02/2021	14	0.03	0.82
06/02/2021	04/03/2021	26	0.10	1.34
04/03/2021	26/03/2021	22	0.09	1.55

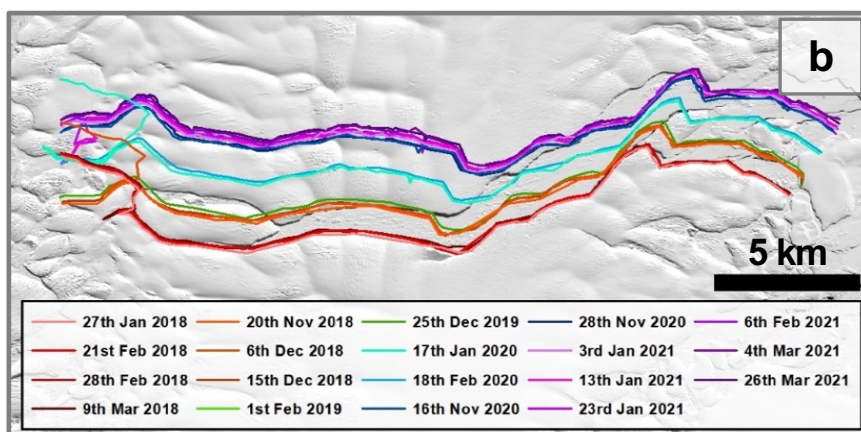
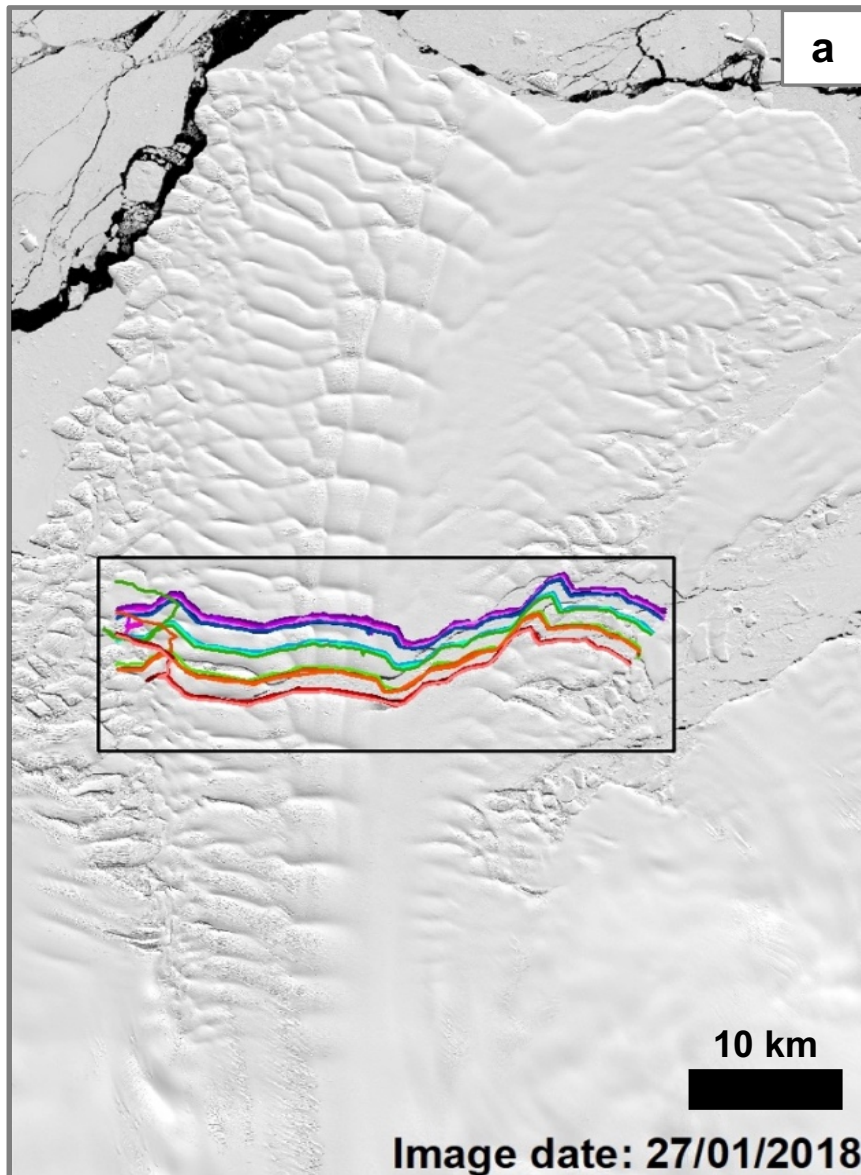


Figure 4.8: (a-b) Visualisation of cumulative terminus re-advance at Ninnis Glacier following the January 2018 calving event (27th January 2018 and 26th March 2021). Mapping was performed at sub-annual resolution using Landsat 8 and Sentinel-2 satellite imagery.

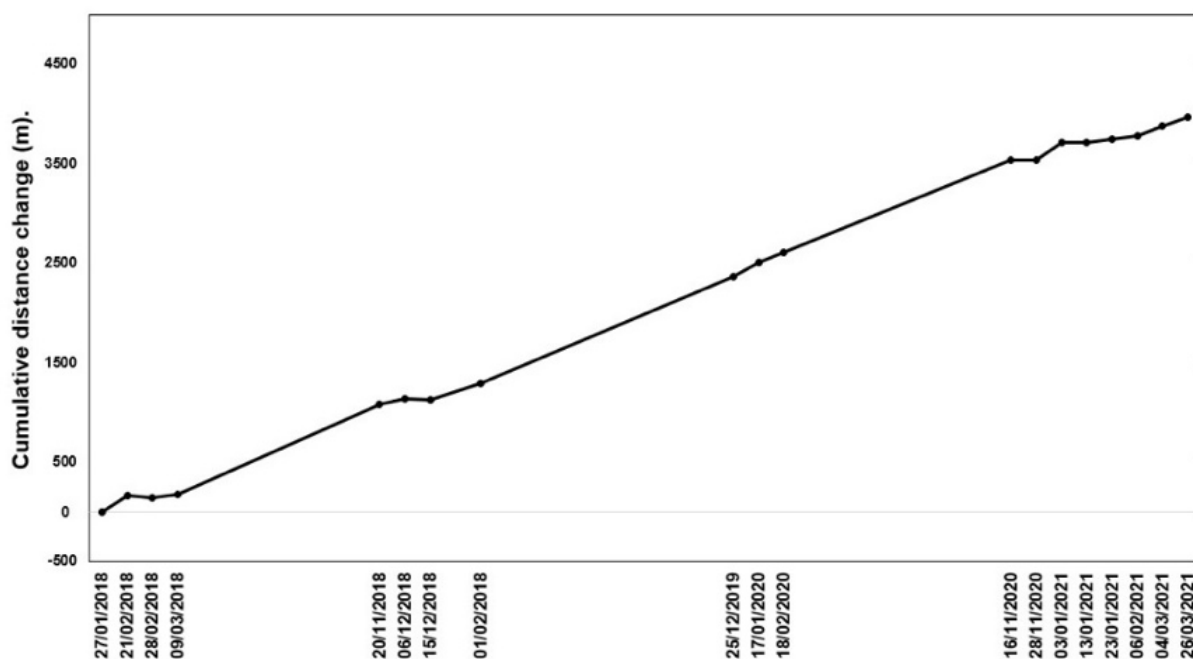


Figure 4.9: Cumulative sub-annual terminus position change (m) (27/01/2016 – 26/03/2021).

4.3. Structural Glaciology

4.3.1. Structural evolution of Ninnis Glacier (pre-1998 calving event)

The evolution of Ninnis' structural glaciology prior to the June 1998 calving event (January 1984 – June 1998) is shown in Figure 4.10. The development of a transverse (perpendicular to flow) rift system was captured on the central portion of Ninnis' tongue which widened and propagated from east to west. The rift emanated from a 2.5 km-wide opening approximately mid-way along Ninnis' eastern ice tongue in January 1989 (Figure 4.10a), measured around 5.8 km in length. This marks the start of Ninnis' structural weakening and disaggregation leading up to the 1998 calving event. Between 1989 and 1991, the rift width expanded by 1.1 km and propagated towards the central flowline of the tongue at a rate of 6,100 m a⁻¹ (Figure 4.10a;b). Expansive sea ice is visibly fastened to the entire rift between 1989 and 1991, whereas no sea ice was present within the rift between 1993 and 1996 during a period when rift migration decelerated (Figure 4.10c;d). Between 1996 and 1997, the rift extended towards the opposing side of Ninnis' tongue (Figure 4.10e;f), leading to minor iceberg break-off inside the rift and dispersal of vertical fractures down-ice of the tongue (Figure 4.10e). By June 1998 the rift propagated across the entire tongue, initiating separation of a large tabular iceberg from the newly formed 1998 ice front, which advanced until the following calving event in 2018 (Figure 4.5; 4.10).

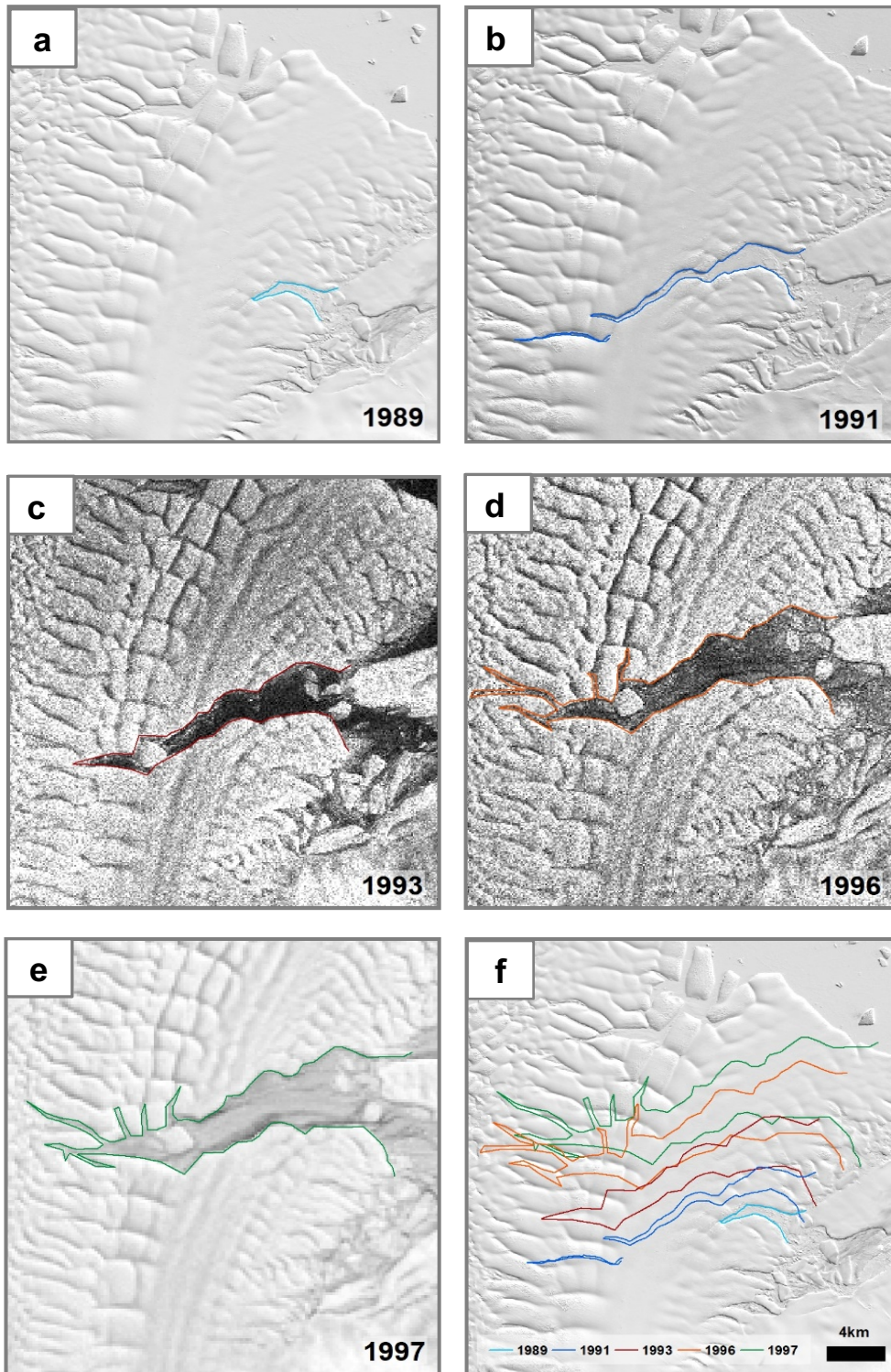


Figure 4.10: Maps depicting the evolution of the central rift system at Ninnis Glacier for 1989 (a), 1991 (b), 1993 (c), 1996 (d), 1997 (e). Shapefiles for panels (a-e) are overlain in panel (f).

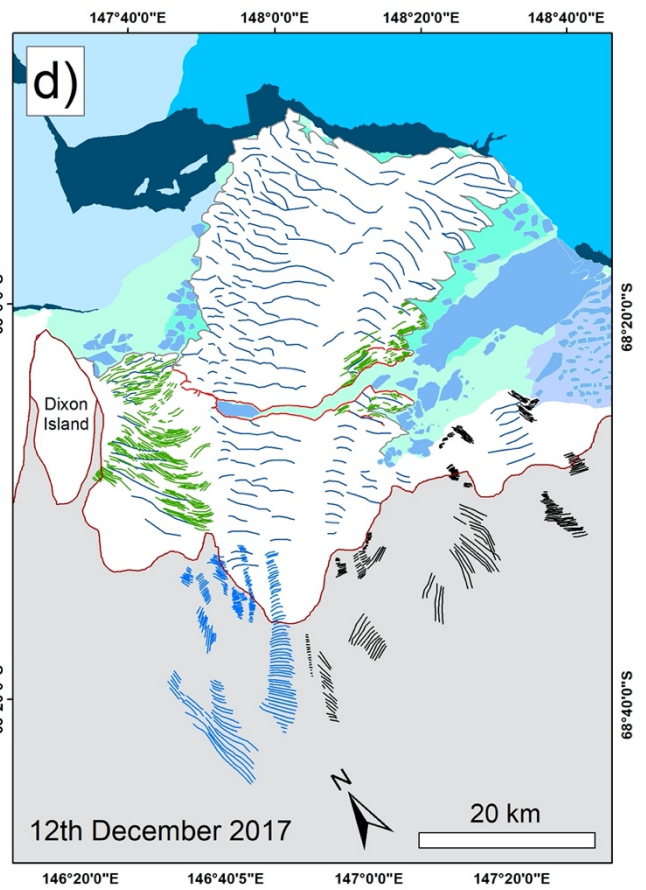
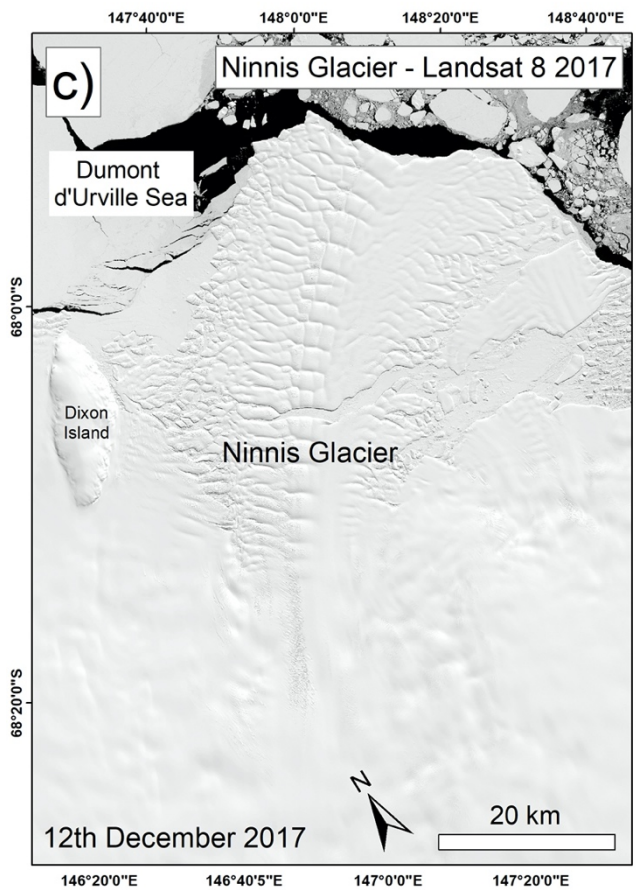
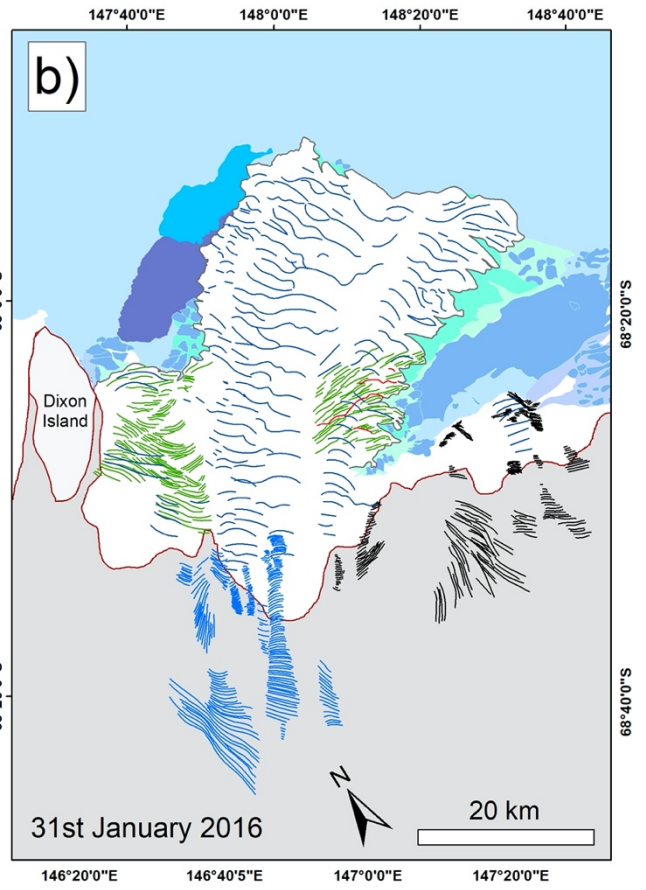
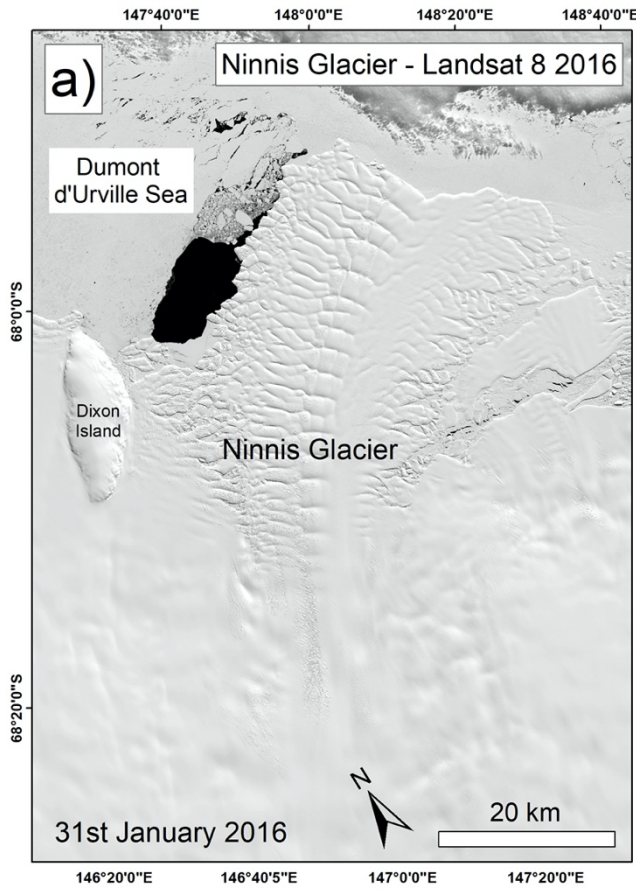
4.3.2. Structural evolution of Ninnis Glacier (pre and post 2018 calving event)

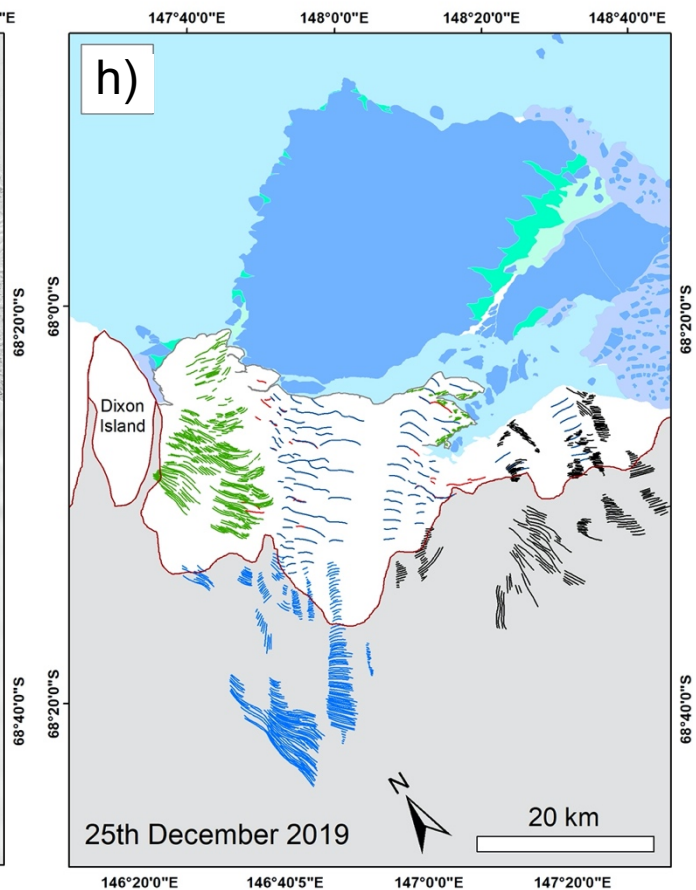
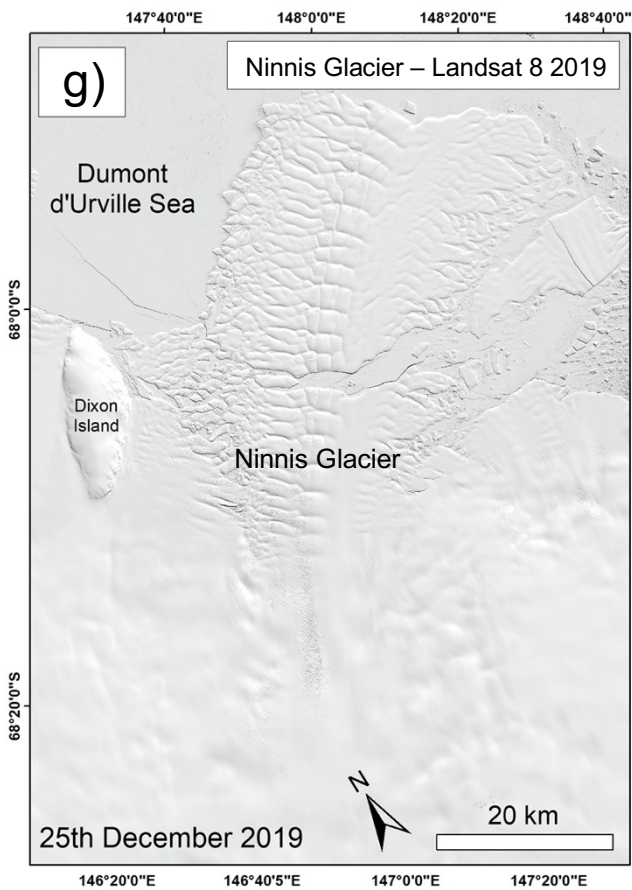
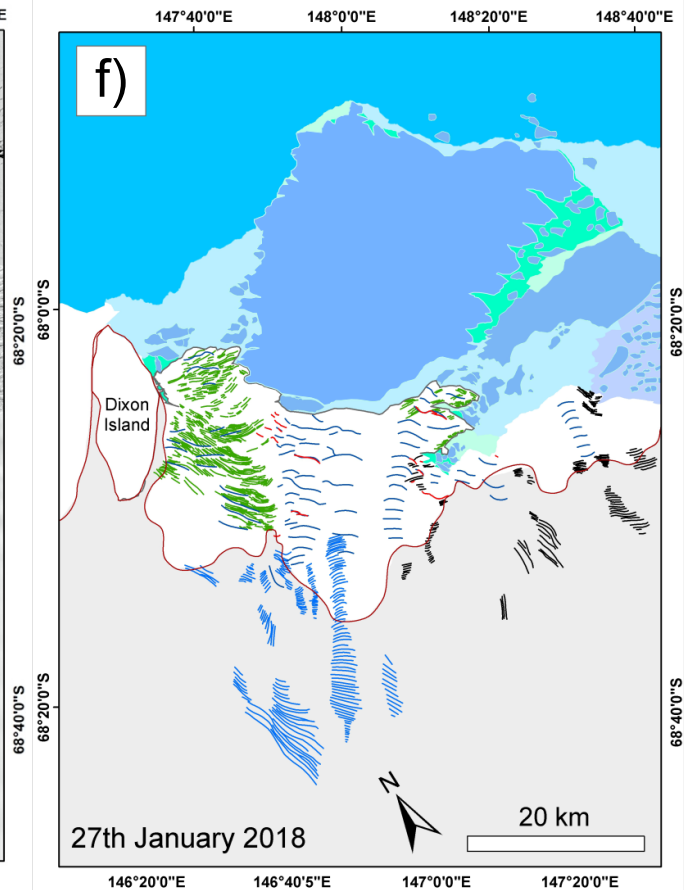
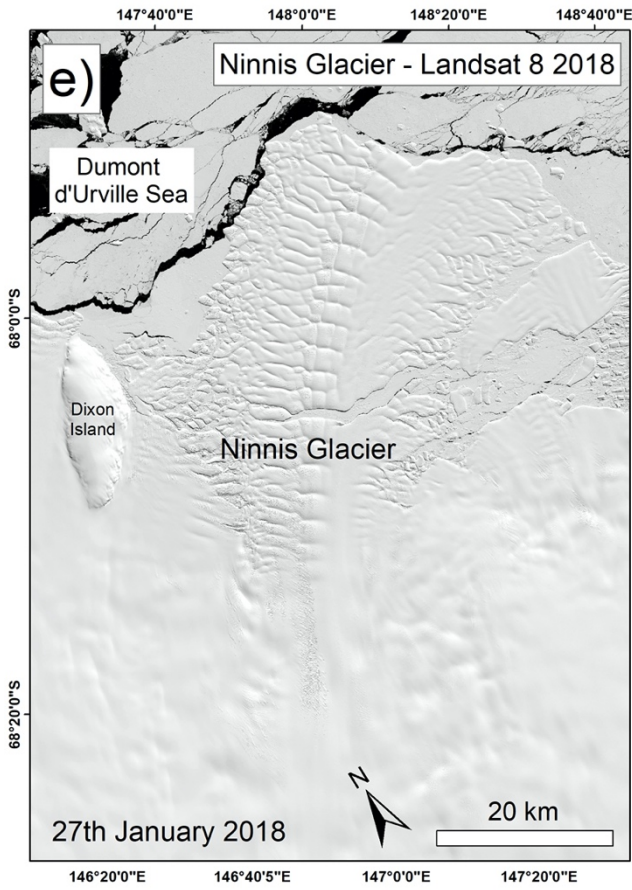
Structural changes on Ninnis' tongue before, during and after the January 2018 calving event are shown in Figure 4.11. In the 2016 Landsat image, two years prior to calving, Ninnis consisted of very few crevasses up-ice of the 1992 grounding line. Rather, it was dominated by a cluster of splaying and transverse (extensional) crevasses (Crevasse Zone 1) (Figure 4.11a;b). An array of splaying crevasses have been mapped to the east of Crevasse Zone 1 (mapped as other crevasses) which are randomly distributed within even smaller clusters, illustrating some structural discontinuities up-ice of the grounding line (Figure 4.11). Down-ice of the grounding line the length and distribution of extensional crevassing decreased, with a noticeable transition towards large transverse fracture traces. Fractures were identical to those mapped between 1989 and 1997 with the largest fractures distributed along Ninnis' central flow unit before spreading across the entire tongue as smaller fractures (Figure 4.10; 4.11). Fractures mapped in 2016 and 2017 were superimposed by chaotic crevassing predominantly on the eastern and western seaboard of Ninnis' ice tongue in areas of heavy shear (Crevasse Zone 2) (Figure 4.11a-d).

In 2016 an isolated crack resembling a rift opening was observed in the exact same area as the rift system monitored across the previous calving cycle and was superimposed with intense crevassing (Figure 4.10; 4.11a;b; 4.12a). However, there are distinct differences between the rifts formed in 2016 and 1989. Firstly, the long and thin morphology of the 2016 rift opened several kilometers in-ice, whereas the 1989 rift was wider and formed along the western seaboard of Ninnis' ice tongue. Secondly, there is no noteworthy increase in rift width or pronounced tongue rotation, as observed between 1989 and 1997 (Figure 4.10). Finally, the timing between rift opening and completion (2016-2018) for the most recent calving event in January 2018 was 7-years shorter compared to the previous calving cycle (1989-1998) (Figure 4.10; 4.11a-d; 4.12). Between 2016 and 2017 there was no discernible change in the size and extent of all mapped crevasses up-ice from the grounding line. Yet, downstream, there is a reduction in crevasse extent along the eastern sector of crevasse zone 2. This coincides with the opening and propagation of the central rift (Figure 4.11c;d). Following its opening, no notable changes in fracture traces and crevassing in the western sector of zone 2 were detected, except for one smaller rift which extended towards the central rift at a negligible rate (2 km a^{-1}) (Figure 4.11c;d; Figure 4.12). During its evolution between December 2016 and December 2017, sea ice remained enclosed within the rift near an area of extensive MYLI along the eastern side Ninnis' ice tongue, which has constrained an assemblage of calved icebergs since 2009 (Figure 4.11c;d).

By the 27th of January 2018, a pathway is observed in which the main rift conjoined with the much smaller western rift (Figure 4.11e;f). Although the gap between each side of the rift is extremely small (<35 m) relative to the width of the rift opening (4.7 km), there is a clear route to delineate a new terminus position and subsequent detachment of a large (~811 km²) tabular iceberg (Figure 4.7). This provided a visual indicator of the most recent calving event at Ninnis in January 2018 (Figure 4.7; 4.11e;f). The tabular iceberg remained in direct contact with the ice tongue until the 25th of December 2019 when it became fully detached and by the 16th of January 2020, the eastern side of the iceberg started to rotate away from the newly formed terminus (Figure 4.11i;j). Following detachment of the tabular iceberg there were no recorded changes in the size and extent of crevassing up-ice and down-ice of the grounding line (Figure 4.11e;j)

Overall, structural glaciological maps of Ninnis Glacier between 2016 and 2020 have revealed clear differences in crevasse morphology both up-ice and down-ice of the grounding line (Figure 4.11). Crevasse Zone 1 refers to the mapped area of splaying and transverse crevasses up-ice of the grounding line which saw no discernible changes in their size and extent between 2016 and 2020. Down-ice of the grounding line, the size of crevasses in Zone 2 reduced in size and extent across all years (2016-2020), transitioning to large transverse fracture traces distributed evenly across Ninnis' ice tongue. These are identical to those mapped prior to the 1998 calving event (1989-1997) which remained consistent in their size and extent between 2016 and 2020 (Figure 4.10; 4.11). Finally, the most notable structural changes at Ninnis took place between 2016 and 2018 across Crevasse Zone 2, located in areas of heavy fracturing at the eastern and western shear zones. The eastern sector of Crevasse Zone 2 saw the rapid development of a central rift which propagated towards the west of Crevasse Zone 2, leading to the eventual detachment of a large (~ 811 km²) tabular iceberg (Figure 4.7; 4.11e-f). Rift development also saw the reduction of crevassing on the east of Crevasse Zone 2, but crevassing remained consistent to the west within an area of heavy shear adjacent to its pinning point at Dixon Island (mapped as ice rises in Figures 4.11a-j).





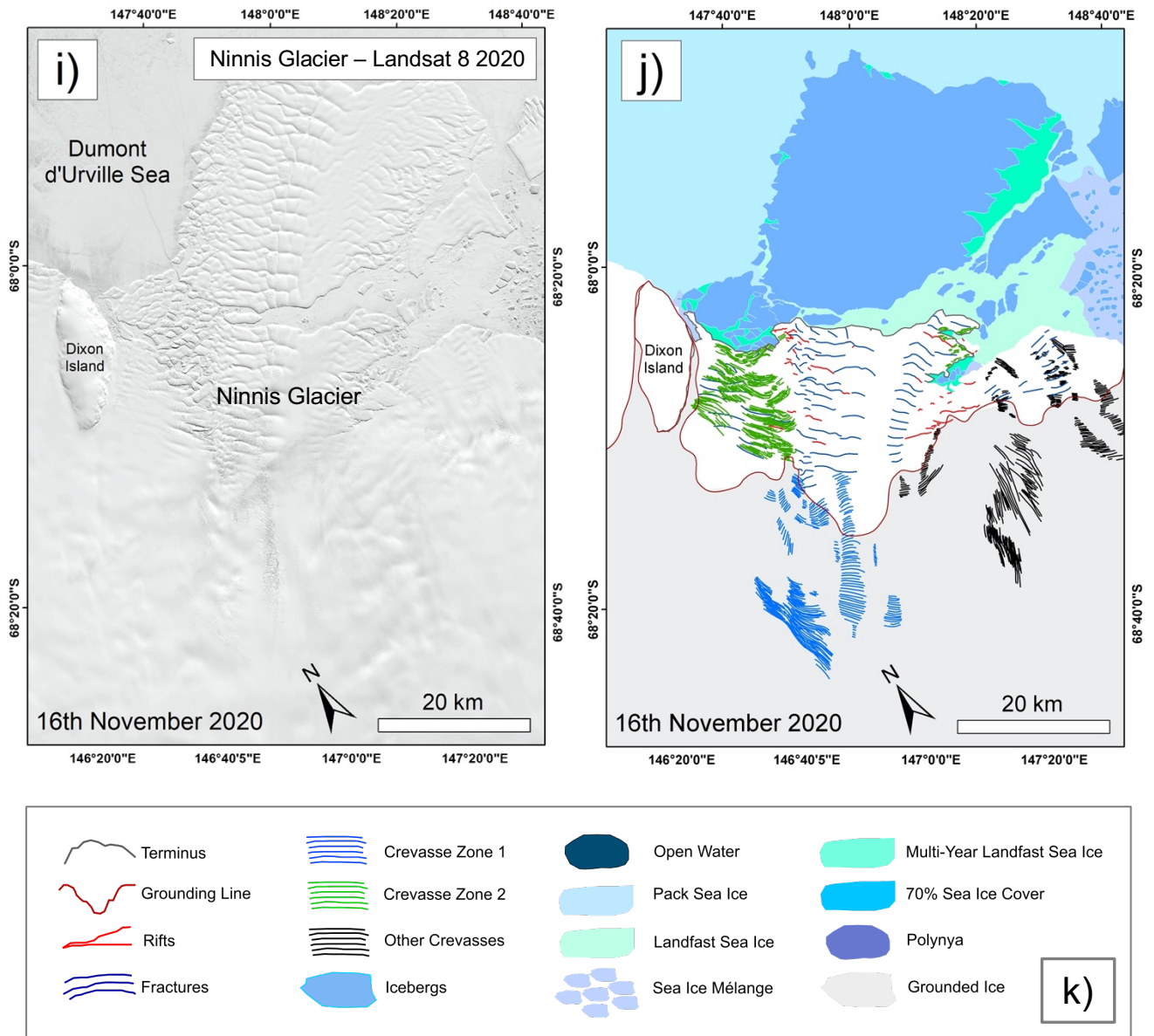


Figure 4.11: Maps detailing short-term changes in structural glaciological and spatial features observed across Ninnis Glacier between 31st January 2016 (a-b) and 16th November 2020 (i-j). Refer to legend in panel (k). Note the rapid (24-month) time-frame between rift opening (panels a-b) and calving in January 2018 (panels e-f).

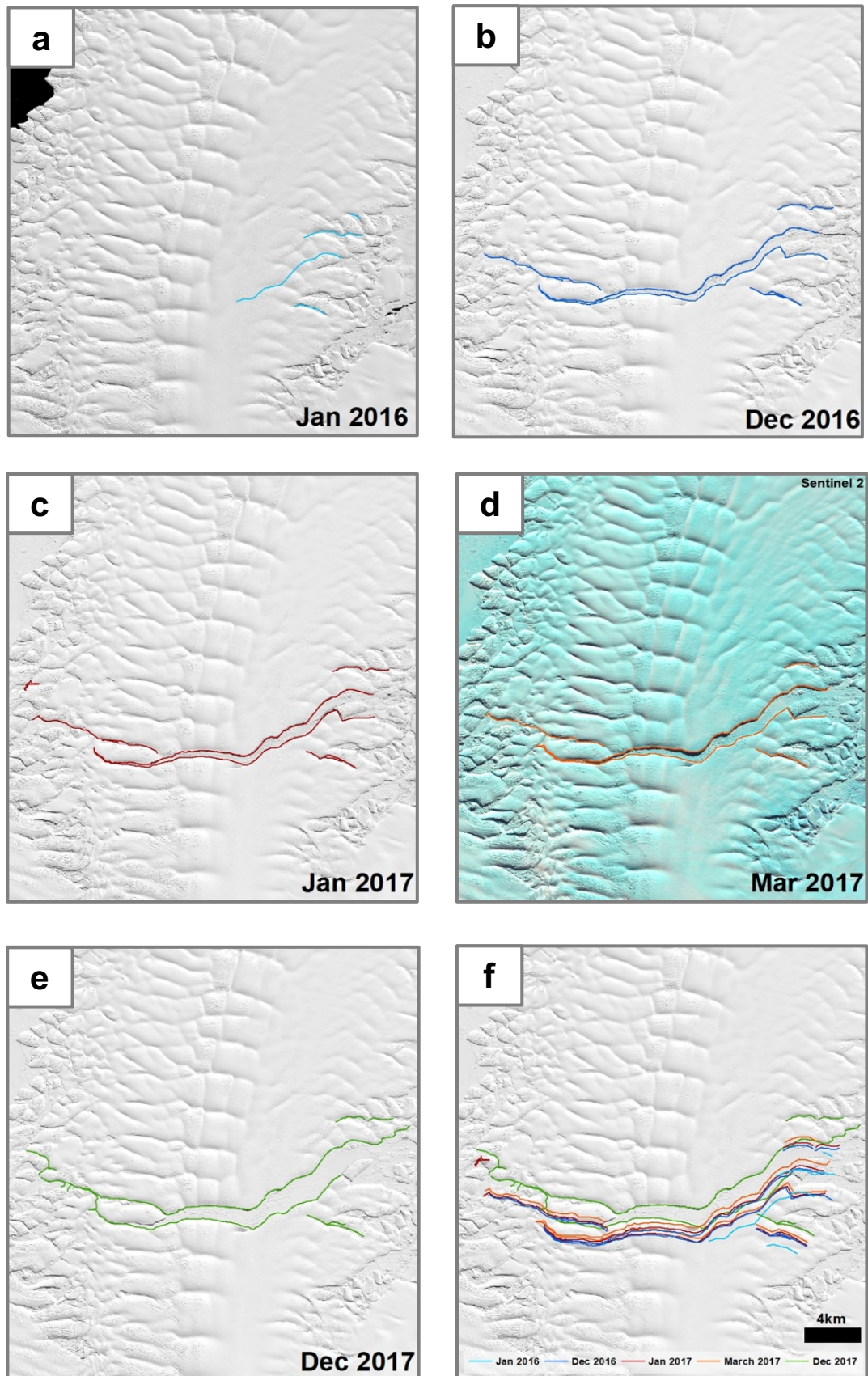


Figure 4.12: Maps depicting the evolution of the central rift system at Ninnis Glacier (January 2017 – December 2017) (a-e). shapefiles in panels (a-e) are overlain in panel (f).

4.3.3. Extent and distribution of sea ice offshore of Ninnis Glacier (2016-2020)

Changes in the extent and distribution of sea ice types before, during and after the January 2018 calving event are illustrated in Figure 4.11. Landsat 8 images for January 27th 2016 and December 12th 2017 revealed a transition from small scale sea ice break-up to more extensive break-up of pack ice, revealing vast exposures of open water at the terminus (Figure 4.11a-d). In January 2016, the south-west of Ninnis' tongue was exposed to a large 30 km² polynya and an area of <70 % sea ice cover adjacent to the polynya (Figure 4.11a;b). By December 12th 2017, this area of the tongue was sealed by Landfast sea ice, linked to the polynya formation a year prior, which is known to form sea ice along the George V Land coastline (Kusahara et al., 2011). At the terminus, open water exposures were observed (Figure 4.11c;d), whereas extensive landfast sea ice enclosed the central rift system and sealed the western side of the ice tongue where the polynya exposure was mapped on January 27th 2016 (Figure 4.11a;b; 4.13).

In the January 27th 2018 Landsat 8 image, sea ice surrounding both sides of the tabular iceberg formed from the 2018 calving event appeared generally less consolidated compared to that in 2017 (Figure 4.11e;f). In the south-eastern sector of Ninnis' tongue, small exposures of open water were observed directly offshore of the iceberg and the newly formed terminus. The same was observed within the area of the former rift, showing that sea ice concentrations were generally lower in the build-up to calving. Between December 25th 2019 and November 16th 2020, George V Land was surrounded by high concentrations of pack ice which engulfed the north and western sectors of the tabular iceberg (Figure 4.11g-j). Directly in front of the newly formed terminus there is a marked transition from less-consolidated pack ice to landfast sea ice between the 2019 and 2020 images (Figure 4.11g-j). This coincides with a 1.2 km a⁻¹ re-advance between 2019 and 2020, which was 0.2 km a⁻¹ slower than the re-advance rate immediately after the 1998 calving event (1998-1999) (Table 4.1).

Overall, in the build-up to the 2018 calving event (2016-2017) there is a general reduction in consolidated sea ice proximal to the terminus, although evidence of polynya formation in 2016 facilitated the growth of landfast sea ice attached to Ninnis' southwestern tongue. Between 2017 and 2018 there is an evident transition from landfast sea ice to less consolidated pack ice enclosing the area of the central rift system. When calving took place in January 2018, both the terminus and the former rift system saw a break-up in Landfast sea ice. However, during a slower terminus re-advance relative to the 1998 event, both the newly formed terminus and tabular iceberg were sealed by extensive pack ice.

4.4. Ice velocity measurements

4.4.1. MEaSURES annual velocity changes (2006-2011)

To determine whether the minor 2008 calving event triggered a significant velocity response, as hypothesised by Rignot et al. (2019), mean velocity trends were analysed between 2006 and 2011. Throughout this 5-year observation period, there was no evidence of high magnitude ice flow accelerations across all sectors of Ninnis Glacier (Table 4.3; 4.4) (Figure 4.13; 4.14; 4.15). In the build-up to the localised calving event on Ninnis' western tongue (2006-2007) velocities extracted from Flowline 1 show a 4.7 % deceleration up-ice of the grounding line (Table 4.3; Figure 4.13). A further 6.2 % deceleration followed between 2008 and 2009, corresponding with the immediate period after the minor calving event (Table 4.3). Although up-ice grounding line velocities increased by 5 % between the periods 2008-2009 and 2010-2011, mean velocities were still 8.6 % slower than 2006 and 2007 mean values.

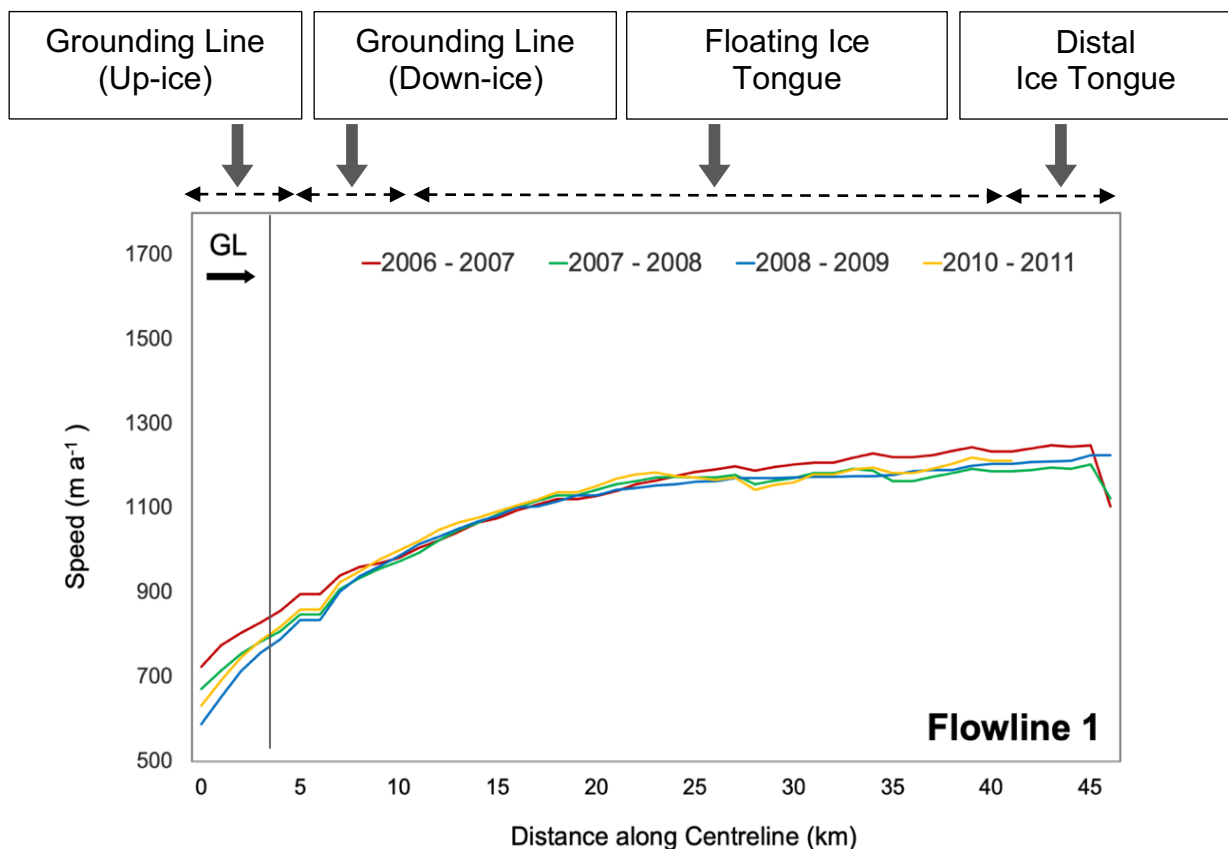


Figure 4.13: Time-series of annual velocity changes (2006 and 2011) at Ninnis Glacier extracted along Flowline 1 shown in Figure 3.4. Vertical grey line resembles the 1992 MEaSURES grounding line.

Overall, mean velocities extracted from Flowline 1 decelerated by 7.8 % up-ice of the grounding line between 2006 and 2011 (Table 4.3). During the same period there was negligible velocity change down-ice of the grounding line (+1.9 %) and across Ninnis' floating (-0.7 %) and distal (>0 %) ice tongue (Table 4.3; 4.4).

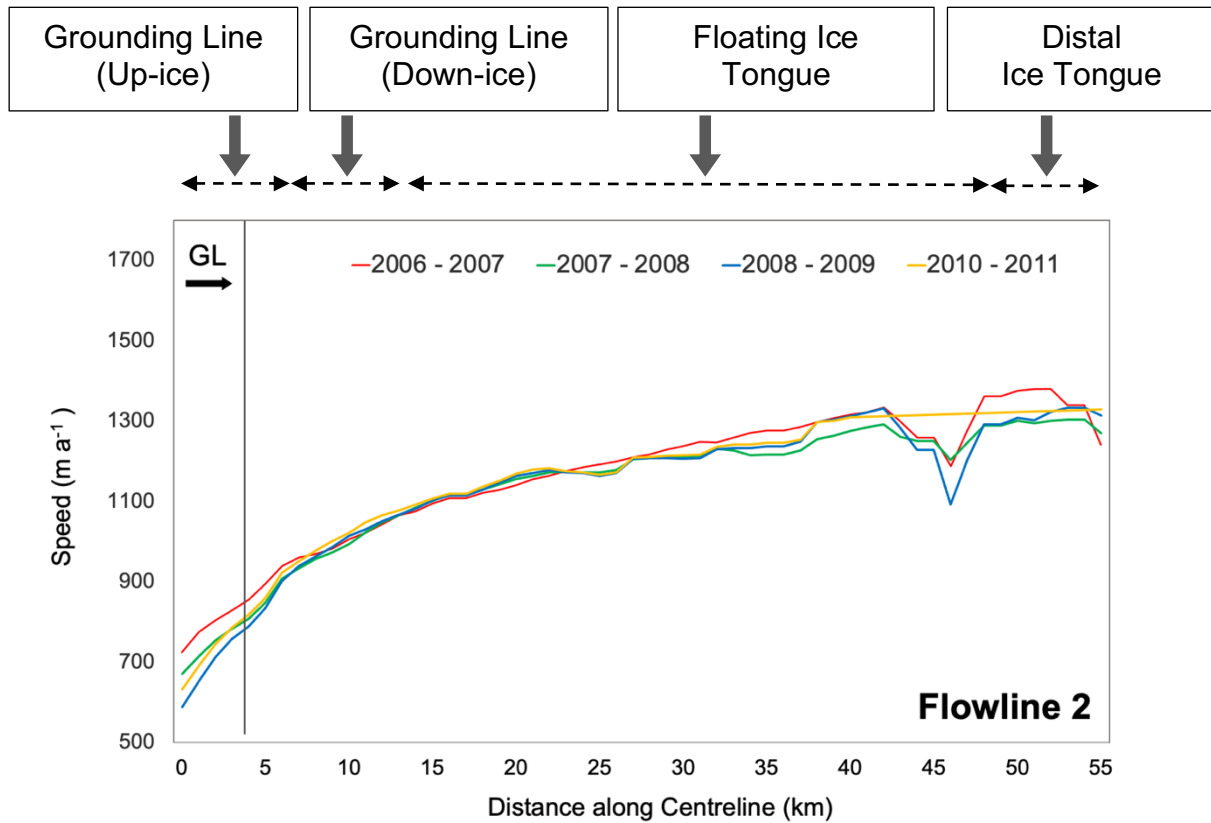


Figure 4.14: Time-series of annual velocity changes (2006 and 2011) at Ninnis Glacier extracted along Flowline 2 shown in Figure 3.4. Vertical grey line resembles the 1992 MEaSURES grounding line. Note the loss of pixel coverage between 40 km and 55 km along Flowline 2 in the 2010-2011 mosaic.

Velocities extracted from Flowline 2 display similar trends to that recorded on Flowline 1, with negligible changes in ice flow velocity recorded across all sectors at Ninnis Glacier during the 5-year observational period (Table 4.4). Between 2006 and 2011 there was a negligible deceleration in velocity on Ninnis' floating ice tongue (-1.5 %), corresponding with the localised area of the ice tongue where minor localised calving took place (Table 4.4) (Figure 4.6; 4.14; 4.15). Although velocities recorded on Flowline 2 are of higher magnitude compared to Flowline 1 (Figure 4.13; 4.14; 4.15), there is no evidence of a short-term speed-up between 2006 and 2011.

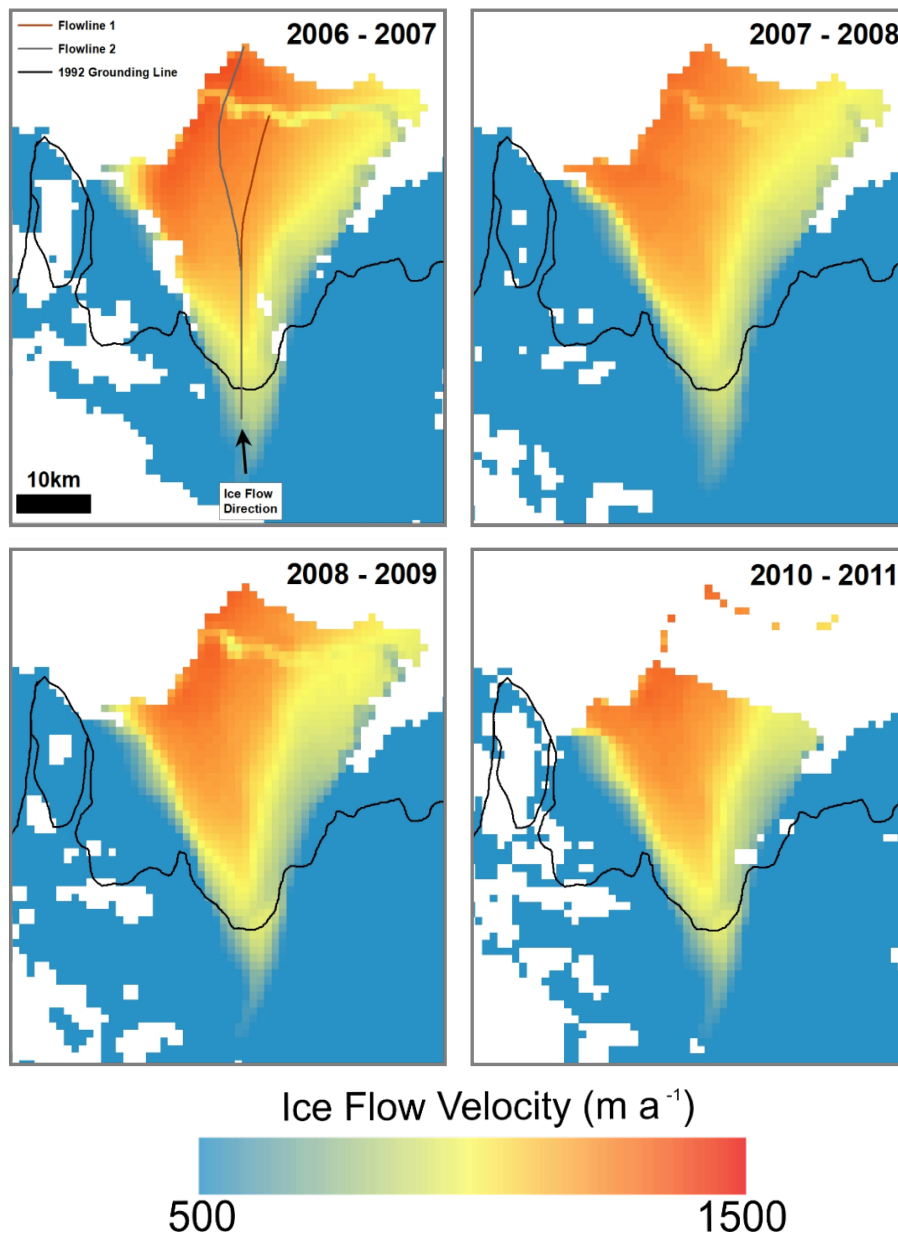


Figure 4.15: Maps of annual velocity (m a^{-1}) at Ninnis Glacier between 2006 and 2011 extracted from the MEaSURES mosaics along Flowline 1 (Red line) and Flowline 2 (Grey line) (a-d). Maps are overlain with 1992 MEaSURES grounding line (Rignot et al., 2011).

Table 4.3: Summary of mean velocities (m a^{-1}) recorded on the respective sectors Ninnis Glacier between 2006 and 2011 from Flowline 1 (Figure 3.4). The % change column represents the change in velocity between each successive mosaic as a percentage and the total percentage change throughout the observational period.

Flowline 1	Grounding Line (Down-Ice)		Grounding Line (Down-Ice)		Floating Ice Tongue		Distal Ice Tongue	
	Mean velocity (m a^{-1})	% Change	Mean velocity (m a^{-1})	% Change	Mean velocity (m a^{-1})	% Change	Mean velocity (m a^{-1})	% Change
2006 - 2007	798.3		932.5		1158.4		1218.1	
2007 - 2008	746.8	-4.7	899.3	-3.6	1141	-1.5	1181.7	-3
2008 - 2009	700.5	-6.2	895.2	-0.5	1140.6	>0	1217.2	3
2010 - 2011	735.4	5	915	2.2	1150.2	-2	NO DATA	
	Overall % Change	-7.8	Overall % Change	1.9	Overall % Change	-0.7	Overall % Change	>0

Table 4.4: Summary of mean velocities (m a^{-1}) recorded on the respective sectors Ninnis Glacier between 2006 and 2011 from Flowline 2 (Figure 3.4). The % change column represents the change in velocity between each successive mosaic as a percentage and the total percentage change throughout the observational period.

Flowline 2	Grounding Line (Up-Ice)		Grounding Line (Down-Ice)		Floating Ice Tongue		Distal Ice Tongue	
	Mean velocity (m a^{-1})	% Change	Mean velocity (m a^{-1})	% Change	Mean velocity (m a^{-1})	% Change	Mean velocity (m a^{-1})	% Change
2006 - 2007	798.3		950.1		1198.9		1325	
2007 - 2008	746.8	-4.7	924.3	-2.7	1182	1.4	1280.6	-3.4
2008 - 2009	700.5	-6.2	925.6	-0.1	1189.8	0.7	1280.1	>0
2010 - 2011	735.4	5	943.2	1.9	1181.3	-0.7	1330	3.9
	Overall % Change	-7.8	Overall % Change	-0.7	Overall % Change	-1.5	Overall % Change	0.4

4.4.2. ITS_LIVE annual velocity changes (2013-2018)

To determine whether Ninnis exhibited a velocity response in the build-up to calving in January 2018, mean velocities from ITS_LIVE mosaics between 2013 and 2018 were analysed. Overall, the 5-year time-series exhibits spatial variability in the magnitude of velocity fluctuations (Table 4.5) (Figure 4.16; 4.17). There is no discernible change in velocities both 5 km up-ice and down-ice of the grounding line across the observational period (+ 0.6 % and +0.4 %), with maximum flow speeds as low as 875.9 m a⁻¹ in 2007 (Table 4.5). This trend is maintained as far as 15 km down-ice of the grounding line, where there is only a 1.3 % difference in recorded velocities between 2013 and 2018. Between 2013 and 2015, at a period where Ninnis' ice front was advancing at a mean rate of 1.5 km a⁻¹, velocities were uniform from 22 km down-ice of the flowline until the end of pixel coverage on the distal part of the tongue. Across this portion of the flowline, mean maximum velocities were quantified at 1,239 m a⁻¹ between 2013 and 2015 (Table 4.5) (Figure 4.16; 4.17).

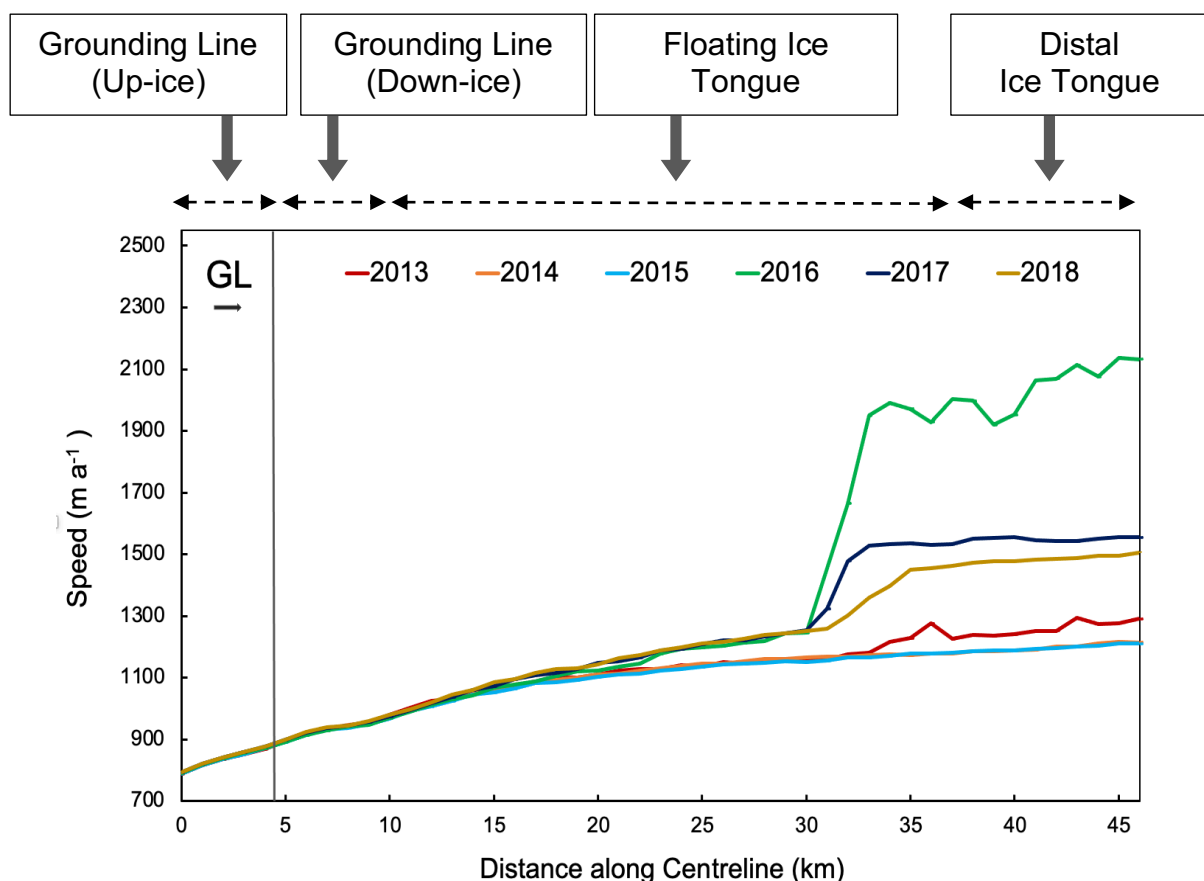


Figure 4.16: Time-series of annual velocity changes (2013-2018) at Ninnis Glacier extracted along Flowline 1 starting upstream of the grounding line (GL) and finishing on the distal portion of the Ninnis tongue where pixel coverage ends. Vertical grey line resembles the location of the 1992 MEaSURES grounding line shapefile intersecting with Flowline 1.

Table 4.5: Summary of mean velocities (m a^{-1}) and percentage change (%) between each ITS_LIVE mosaic. Velocities were recorded from Flowline 1 (See Figure 3.4) for each respective sector of Ninnis Glacier between 2013 and 2018.

ITS_LIVE Mosaics	Grounding Line (Up-Ice)		Grounding Line (Down-Ice)	
	Mean velocity (m a^{-1})	% Change	Mean velocity (m a^{-1})	% Change
2013	832.4		929.7	
2014	835.8	-0.4	929.5	>0
2015	833.1	-0.3	925.1	0.5
2016	834.6	0.2	924.9	>0
2017	838.2	0.4	931.8	0.7
2018	837.7	>0	933.8	0.2
	Overall % Change	0.6	Overall % Change	0.4

ITS_LIVE Mosaics	Floating Ice		Distal Tongue	
	Mean velocity (m a^{-1})	% Change	Mean velocity (m a^{-1})	% Change
2013	1140.1		1277.3	
2014	1124.8	-1.3	1209	-5.3
2015	1119.4	-0.5	1277.3	0.4
2016	1388.5	19.4	2105.3	74.8
2017	1265.6	-8.9	1549.6	-35.9
2018	1234.5	-2.5	1493.8	-3.6
	Overall % Change	8.3	Overall % Change	17

The greatest magnitudes of velocity change were recorded on the floating and distal portions of Ninnis Glacier, with +19.4 and +74.8 % accelerations between 2015 and 2016, respectively. During this period, velocities as high as $2,137 \text{ m a}^{-1}$ were recorded on the distal portion of Ninnis' tongue, representing the fastest ice flow speed observed throughout the 5-year time series (Figure 4.16; 4.17). However, this does not reflect the true velocity of Ninnis' floating ice tongue as it corresponds with the period in which its central rift rapidly opened and propagated in 2016, in the build-up to the January 2018 calving event (Figure 4.17d). Rather, velocities in excess of $2,100 \text{ m a}^{-1}$ on Ninnis' ice tongue reflect the rates of ice tongue rotation in response to rift propagation.

Between 2016 and 2017 ice flow velocities across the floating ice and distal sectors of the flowline decelerated by -8.9 % and -35.9 %; and a further -2.5 % and -3.6 % deceleration between 2017 and 2018. However, mean velocities between 2016 and 2018 across the same portions of the flowline were still markedly faster than the 2013 mean, with an overall +8.3 % and +17 % acceleration across the 5-year observational period (Table 4.5). This shows a contrasting behaviour between velocities recorded near the terminus and up-ice and down-ice of the grounding line.

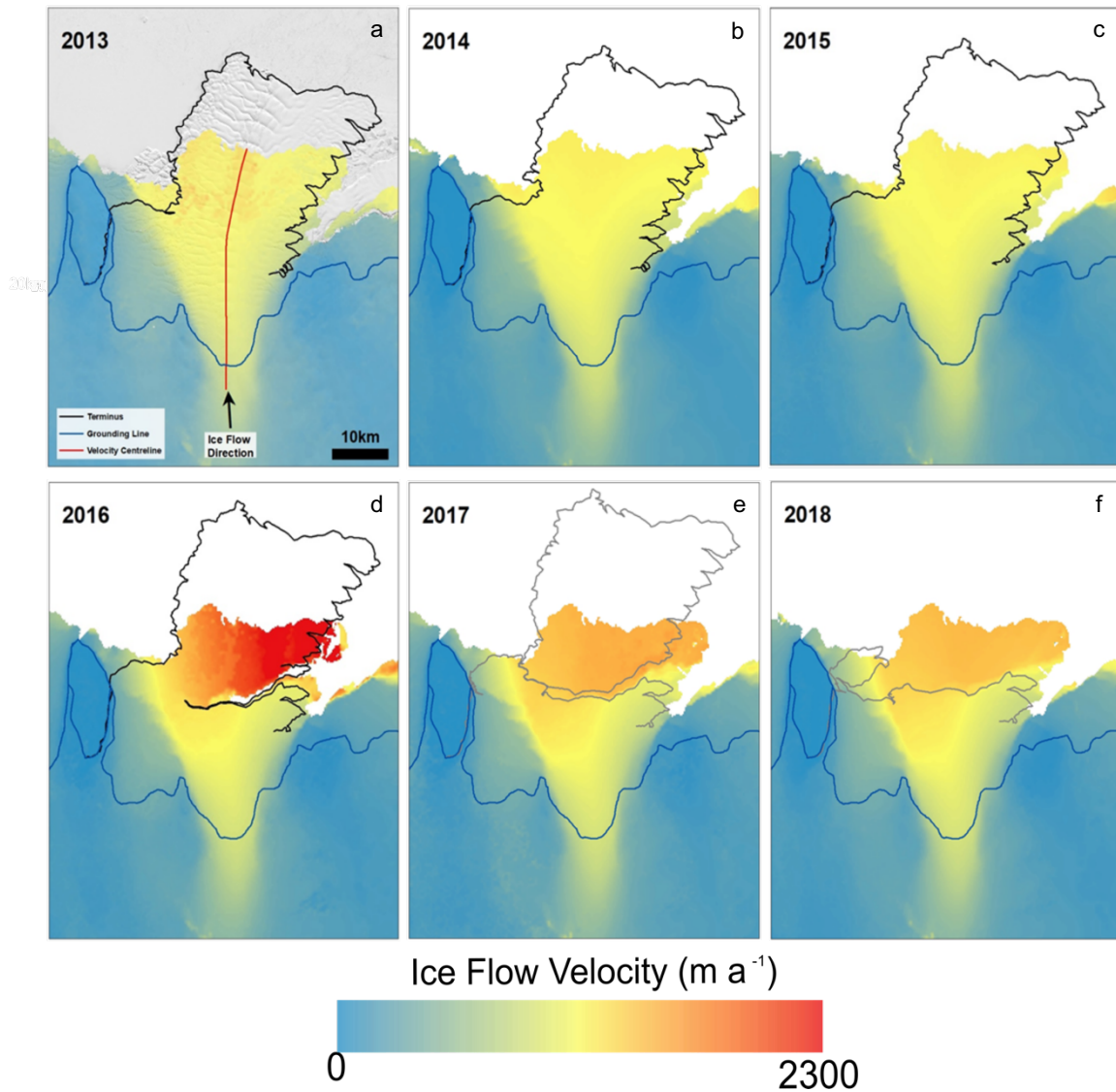


Figure 4.17: Maps of annual velocity (m a^{-1}) at Ninnis Glacier between 2013 (a) and 2018 (f) extracted from the ITS_LIVE mosaics along the red flowline (Flowline 1) shown in panel a. Each panel depicts the digitised terminus for that given year and is overlain with the 1992 MEaSURES grounding line dataset (Rignot et al., 2011).

4.4.3. Sentinel-2 sub-annual velocity mosaics (2018-2021)

Mean velocities from sub-annual Sentinel-1 imagery between January 2018 and June 2021 were analysed to ascertain whether Ninnis Glacier experienced a significant dynamical response following the January 2018 calving event. Overall, the 4-year velocity time-series displays a pervasive slow-down across all sectors of Ninnis Glacier between January 2018 and June 2021 (Figure 4.18a; 4.19) (Table 4.6). Velocities both 5 km up-ice and down-ice of the grounding line reduced at negligible rates (-2.1 % and -1.4 %) across the three-year observational period, displaying no rapid high magnitude accelerations (Table 4.6). This

occurred during a 1.26 km a^{-1} ice frontal re-advance after the 2018 calving event (2018-2021) (Table 4.1). Following observed tabular iceberg detachment in January 2018, recorded mean velocities were in excess of 1.5 km a^{-1} , but underwent an overall -18.7 % decrease between January 2018 and June 2021 (Figure 4.19) (Table 4.6). The largest acceleration took place on the distal tongue between December 2018 and March 2020 (+6.6 %), recording the fastest mean velocities across the entire time-series in March 2020 ($1,581 \text{ m a}^{-1}$) (Figure 4.18a) (Table 4.6). However, this acceleration was short-lived and velocities on the distal portion of Ninnis tongue decelerated by 10 % in November 2020, reaching velocities within 3.9 % of December 2018 mean values.

Overall, the dynamical response of Ninnis Glacier following a major tabular calving event in January 2018 is marked by a pervasive deceleration in ice flow velocity between 2018 and 2021. This is reflected in mean annual velocities quantified from Sentinel-1 mosaics between 2018 and 2021 displaying a slow-down on Ninnis' floating ice (-7 %) and distal ice tongue (-12.3 %) (Figure 4.18b) (Table 4.7). By 2021, mean annual velocities across all sectors of Ninnis Glacier reached within 0.4 %, 0.9 %, 2.9 % and 3.2 % of the 2015 mean from the ITS_LIVE velocity time-series.

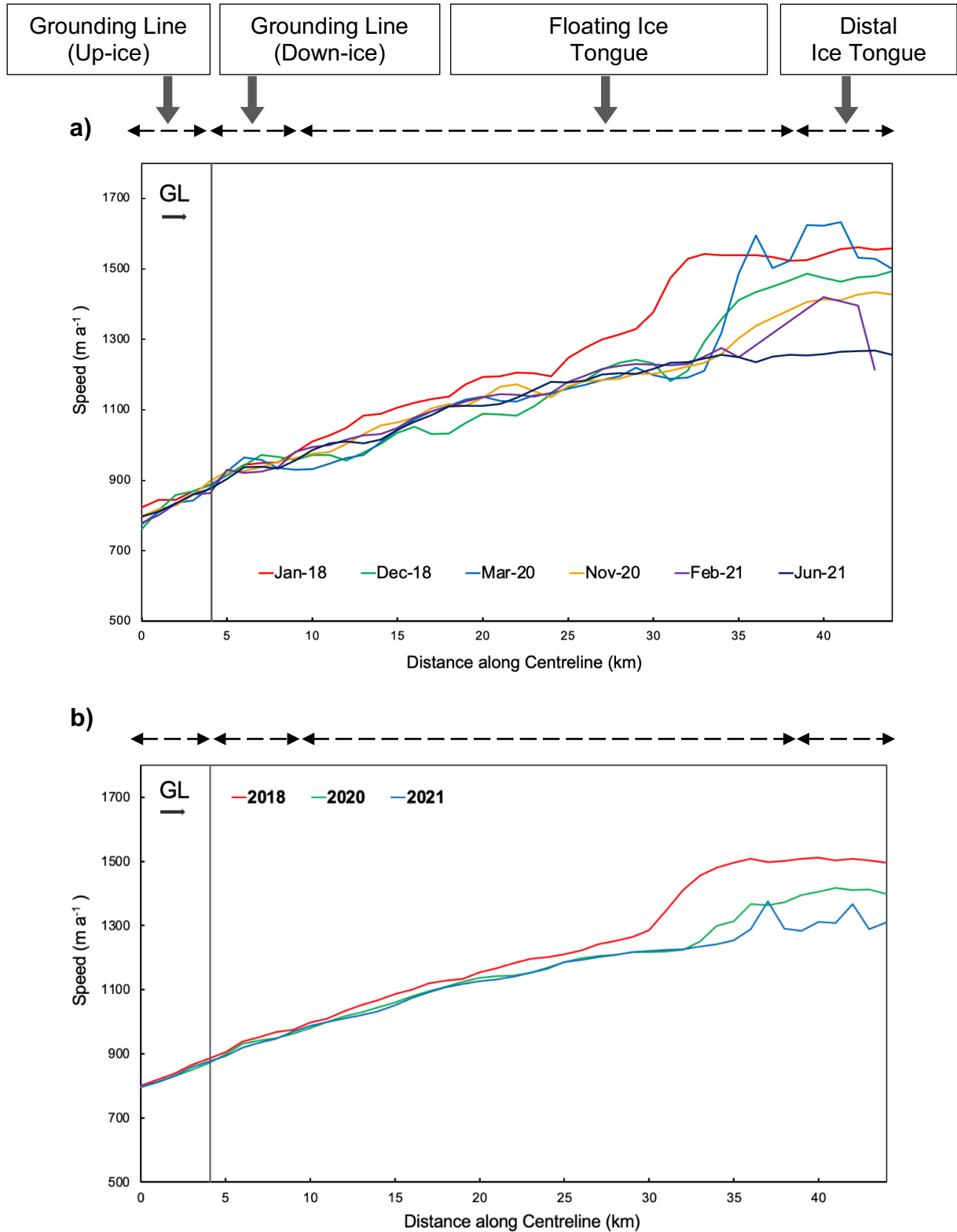


Figure 4.18: Time-series of mean monthly (a) and annual (b) velocity changes (January 2018-June 2021) at Ninnis Glacier between the start of the centreline upstream of the grounding line (GL) and the distal portion of the Ninnis tongue where pixel coverage ends. Vertical grey line resembles the GL.

Table 4.6: Summary table of mean monthly velocities (m a^{-1}) recorded on the respective sectors of Ninnis Glacier between January 2018 and June 2021 from the Sentinel-1A sub-annual velocity mosaics. The % change column represents the change in velocity between each successive mosaic as a percentage and the total change throughout the observational period.

	Grounding Line (Up-Ice)		Grounding Line (Down-Ice)		Floating Ice		Distal Tongue	
	Mean velocity (m a^{-1})	% Change	Mean velocity (m a^{-1})	% Change	Mean velocity (m a^{-1})	% Change	Mean velocity (m a^{-1})	% Change
Jan-18	853.6		947.3		1283.7		1554.2	
Dec-18	838.8	-1.7	950.5	-0.3	1172.6	-8.7	1477.6	-4.9
Mar-20	829.1	-1.2	942.6	-0.8	1179.4	0.6	1581.7	6.6
Nov-20	840.8	1.4	940.7	-0.2	1170.8	-0.7	1422.7	-10
Jan-21	840.5	>0	936.6	-0.4	1153.3	-1.5	1358.8	-4.7
Jun-21	835.4	-0.6	933.7	-0.3	1151.3	-0.2	1262.8	-7
	Overall % Change	-2.1	Overall % Change	-1.4	Overall % Change	-10.3	Overall % Change	-18.7

Table 4.7: Summary table of mean annual velocities (m a^{-1}) recorded on the respective sectors of Ninnis Glacier between 2018 and 2021 from the Sentinel-1A sub-annual velocity mosaics. The % change column represents the change in velocity between each successive mosaic as a percentage and the total change throughout the observational period.

Sentinel-1 Mosaics	Grounding Line (Up-Ice)		Grounding Line (Down-Ice)		Floating Ice		Distal Tongue	
	Mean velocity (m a^{-1})	% Change	Mean velocity (m a^{-1})	% Change	Mean velocity (m a^{-1})	% Change	Mean velocity (m a^{-1})	% Change
2018	841.4		946.7		1239.1		1504.1	
2020	831.1	-1.2	936.7	-1.0	1169.7	-5.6	1408.6	-6.3
2021	836.4	0.6	933.3	-0.4	1152.4	-1.5	1318.6	-6.4
	Overall % Change	-0.6	Overall % Change	-1.4	Overall % Change	-7	Overall % Change	-12.3

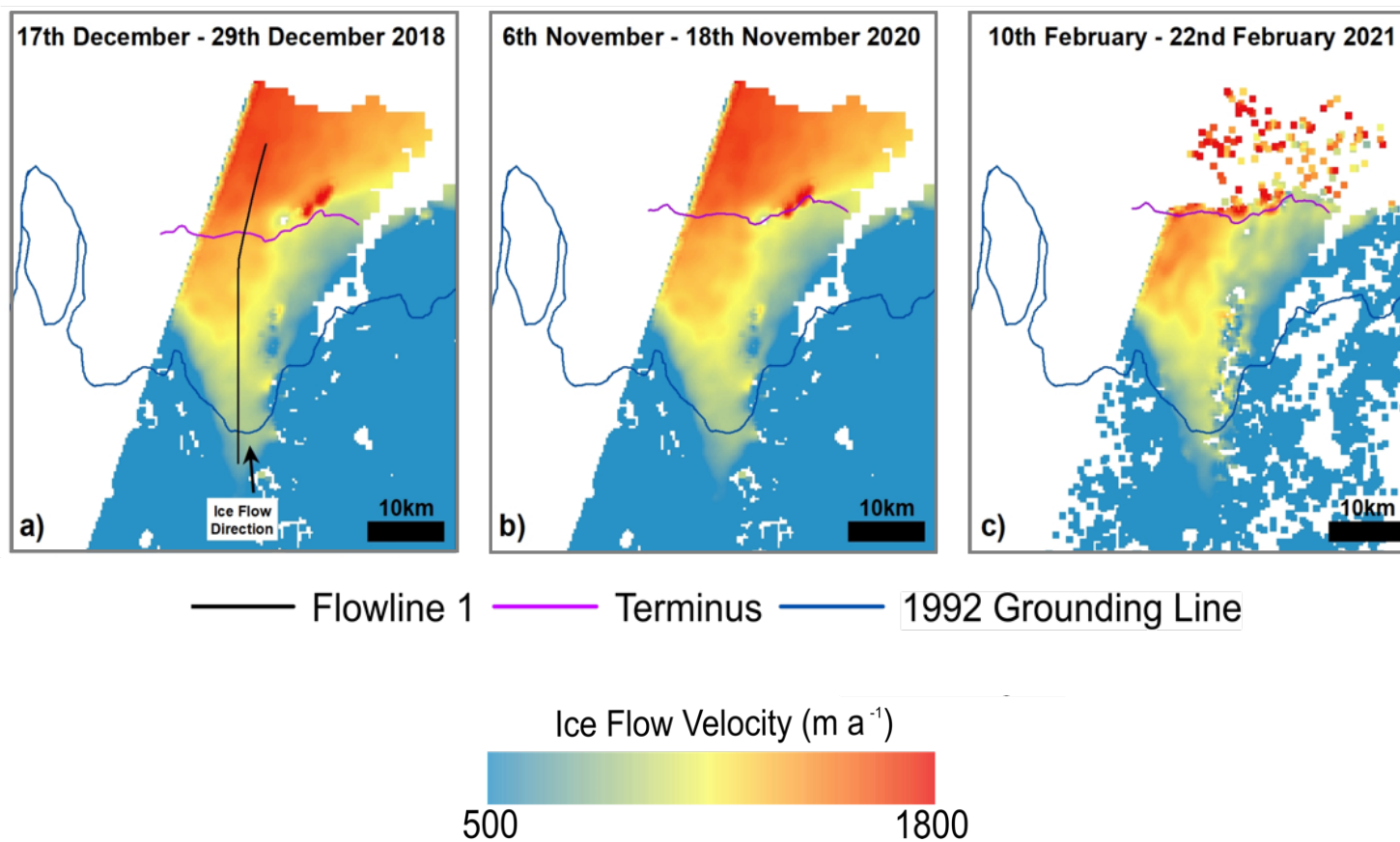


Figure 4.19: Generated maps of mean velocity (m a^{-1}) at Ninnis Glacier for December 2018 (a), November 2020 (b) and February 2021 (c) extracted from the Sentinel-1A sub-annual velocity mosaics along the black flowline shown in panel a. Each panel depicts the digitised terminus for that given year and is overlain with the 1992 MEaSURES grounding line dataset (Rignot et al., 2011).

Chapter 5: Discussion

5.1. The timing of major calving events at Ninnis Glacier

5.1.1. Revising the purported 1980-1982 calving event

Large image gaps prior to 1989 restricted the precise timing of the earliest calving events from being constrained, meaning that the timing of these calving events is still open to debate. Previous studies estimated calving events in the early 1950s and between 1980 and 1982 (Wendler et al., 1996; Frezzotti et al., 1998), based on interpretations of iceberg drift from past field expeditions (Anderson et al., 1980).

Detailed analysis of the 1974 Landsat MSS image has provided sufficient evidence to suggest that a major calving event took place sometime in the early 1970s (1972-1974). In 1974, Ninnis Glacier was subject to intense shearing near its pinning point at Dixon Island which enabled a new terminus position to be delineated amongst a widespread assemblage of small-sized icebergs and shear-induced fractures (Figure 5.1). The extent of shearing observed at Ninnis in 1974 resulted in a loss of its ice tongue's structural integrity as Ninnis' ice tongue ungrounded from its pinning point near Dixon Island (Figure 5.1), similar to that of the Thwaites Glacier Tongue between 2000 and 2018 (Miles et al., 2020). This may have been caused by exceedingly high strain rates exerted on Ninnis' western ice tongue alongside Dixon Island, generating stresses which resulted in the southward propagation of fractures which conjoined with its central rift (Figure 5.1) (Rignot et al., 2006). The generated stresses that were sufficient to resist glacier flow were then lost from intense shearing and partial unpinning of a large section of Ninnis' southwestern ice tongue (Figure 5.1) (Rignot et al., 2006). This triggered the detachment of small icebergs proximal to Ninnis' central flow unit which became enclosed with MYLI within the western shear zone.

Detailed inspection of the 1974 Landsat image allowed MYLI to be easily distinguished from Ninnis' floating ice due to the assemblage of calved blocks which were sealed within the western shear zone (Figure 5.1). As the mapping criteria defines the terminus as the boundary separating floating ice from calved material and sea ice, a clear route was mapped within this zone of intense shearing and fracturing for a new terminus position to be delineated in 1974 (Figure 5.1). This provides evidence for the detachment of a large ~1,450 km² tabular iceberg and hence the first recorded calving event of the 58-year time-series.

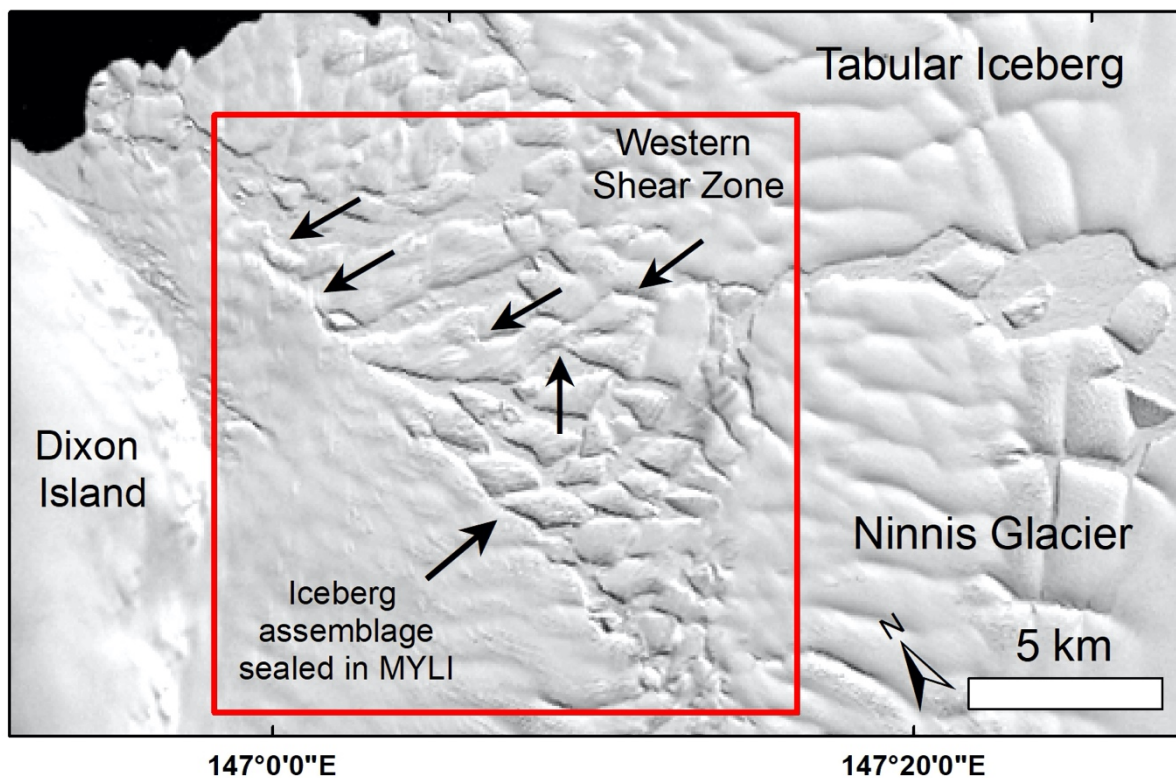


Figure 5.1. Mapped 1974 Landsat MSS image of the Western Shear Zone (red extent indicator) at Ninnis Glacier. Note the completion of a major transverse rift, delineated using the arrows which depict sections of iceberg detachment and the boundaries between floating ice and the newly formed tabular iceberg. Also note the assemblage of small, calved icebergs enclosed in MYLI.

It is possible that calved material sealed by a thick layer of MYLI was previously mapped as consolidated ice in previous observations (Frezzotti et al., 1998; Anderson et al., 1980), particularly as thick lenses of MYLI are known to persist along Ninnis' coastline for several years (Massom, 2003). Subsequently, previous observations failed to account for areas of MYLI which concealed rift completion and acted to curtail iceberg drift (Frezzotti et al., 1998; Massom, 2003). In 1974, Ninnis' western seaboard was free of sea ice, whilst the eastern side was surrounded by extensive sea ice (Fig. 4.2). It is likely that MYLI formed from the east within the former central rift system, whereas a loss of sea ice to the west would have reduced ice tongue buttressing, leading to further rotation, rift propagation and its eventual completion (Figure 4.3) (Banwell et al., 2017; Arthur et al., 2021).

Considering large image gaps in the build-up to 1974, the precise timing of iceberg detachment early in the record is still unknown. Speculating about this is challenging due to the high

concentrations of MYLI sealed within the western shear zone where the new terminus was delineated (Figure 4.3; 4.4; 5.1). This is further complicated as MYLI is known to remain sealed to newly formed icebergs at Ninnis for up to 18 months after calving (Massom, 2003). Therefore, this study estimates that rift completion and iceberg detachment caused by the weakened western shear margin may have occurred 18-months prior to the January 1974 image (in 1972). The '1980s' calving event described by Frezzotti et al. (1998), therefore, probably occurred much earlier (sometime between 1972 and 1974), with previous studies constraining the calving event during the iceberg's drift path from the true terminus once released from sea ice (Anderson et al., 1980; Wendler et al., 1996; Frezzotti et al., 1998). The revised calving date suggested in this thesis (1972-1974) would also mean that the duration between the 1972-1974 calving event and the 1998 event (~24 years) is very similar to the most recent event between 1998 and 2018 (~20 years). This suggests that Ninnis experiences a naturally occurring cycle of advance, terminated by large-scale calving events culminating the removal of large tabular icebergs.

5.1.2. Extrapolating Ninnis' maximum position prior to the early 1970s calving event

Satellite data gaps between 1963 and 1974 also restricted terminus positions from being delineated in the build-up to the 1972-1974 calving event. To estimate Ninnis' maximum extent prior to calving, a terminus position was extrapolated from the distal portion of the tabular iceberg which was partially visible despite extensive cloud cover in the 1974 Landsat MSS image (Figure 4.3;4.4). Based on the knowledge that the tabular iceberg was measured 32 km down-ice of the 1974 margin, this extrapolated position represents Ninnis' most advanced terminus position observed throughout the time series.

Tabular iceberg detachment is estimated to have occurred sometime between 1972 and 1974, meaning that Ninnis' maximum extent prior to calving may have been anytime between 1971 and 1973. There is significantly larger uncertainty relative to other terminus positions in the time-series, owing to minor iceberg drift and rotation which may have taken place following detachment. Yet, the presence of extensive MYLI proximal to the newly formed terminus and iceberg likely means that the iceberg has remained in a relatively similar position since calving. This means that the extrapolated 1971-1973 terminus position may provide a reasonable indication of Ninnis' potential maximum offshore extent prior to calving in the early 1970s.

5.1.3. Revising the purported January 2000 calving event

A major calving event at Ninnis was previously suggested to have taken place in January 2000 by Massom (2003). Despite acknowledging rift completion and subsequent tabular iceberg

detachment in June 1998, the calving event was described as occurring 19 months later following the iceberg's release from landfast sea ice (Massom, 2003). By employing the mapping criteria in this thesis, the revised timing of calving has been placed in June 1998, based on evidence detailing the completion of Ninnis' central rift system and subsequent detachment of an 810 km² tabular iceberg (Figure 4.5; 5.2).

Overall, detailed analysis of satellite images has resulted in revisions to the timing of purported calving events, previously estimated between 1980 and 1982 and in January 2000 (Frezzotti et al., 1998; Massom, 2003). The criteria employed in this study defines calving events based on iceberg detachment of the tongue following rift completion rather than the point in which the iceberg begins to drift from the terminus. Therefore, it is estimated that Ninnis calved in the early 1970s (1972-1974) and in June 1998. The same criteria were applied across recent Landsat and Sentinel-2 imagery, constraining the next major calving event in January 2018.

5.2. A periodic calving cycle at Ninnis

The time series of terminus position change at Ninnis is indicative of a predictable, multi-decadal calving cycle, owing to its cyclical patterns of advance and calving at a 20 to 25-year periodicity across the 58-year observation period. These were recorded between 1972-74, in 1998 and in 2018. The two most recent calving cycles are characterised by (re-)advance phases which extended to relatively similar locations (within 5-8 km of each other), before rift completion triggered large-scale calving events and formed new terminus positions. The newly retreated terminus positions are also mapped as relatively consistent across the time-series, approximately 28, 29 and 25 km downstream of Ninnis' grounding line position in 1992 (Figure 4.1; 5.2).

Despite their cyclical nature, there is some variability between each respective calving cycle. Notably, there is an 18.6 km difference in the maximum ice front extent immediately before the early 1970s (1972-1974) and 1998 calving events (Figure 5.2). Between the two calving events there was an 86 % reduction in tabular iceberg surface area (~1,450 to 780 km²) (Figure 5.2a;b), confirming similar observations of Frezzotti et al. (1998) and Massom (2003). However, there is only a ~4 % difference in tabular iceberg size between the 1998 and 2018 events (~780 and ~811km²) (Figure 5.2b;c). This suggests similarities between the two most recent calving events, reinforced by their maximum and newly formed terminus positions being within 7 and 4 km of each other, respectively (Figure 4.1; 4.2).

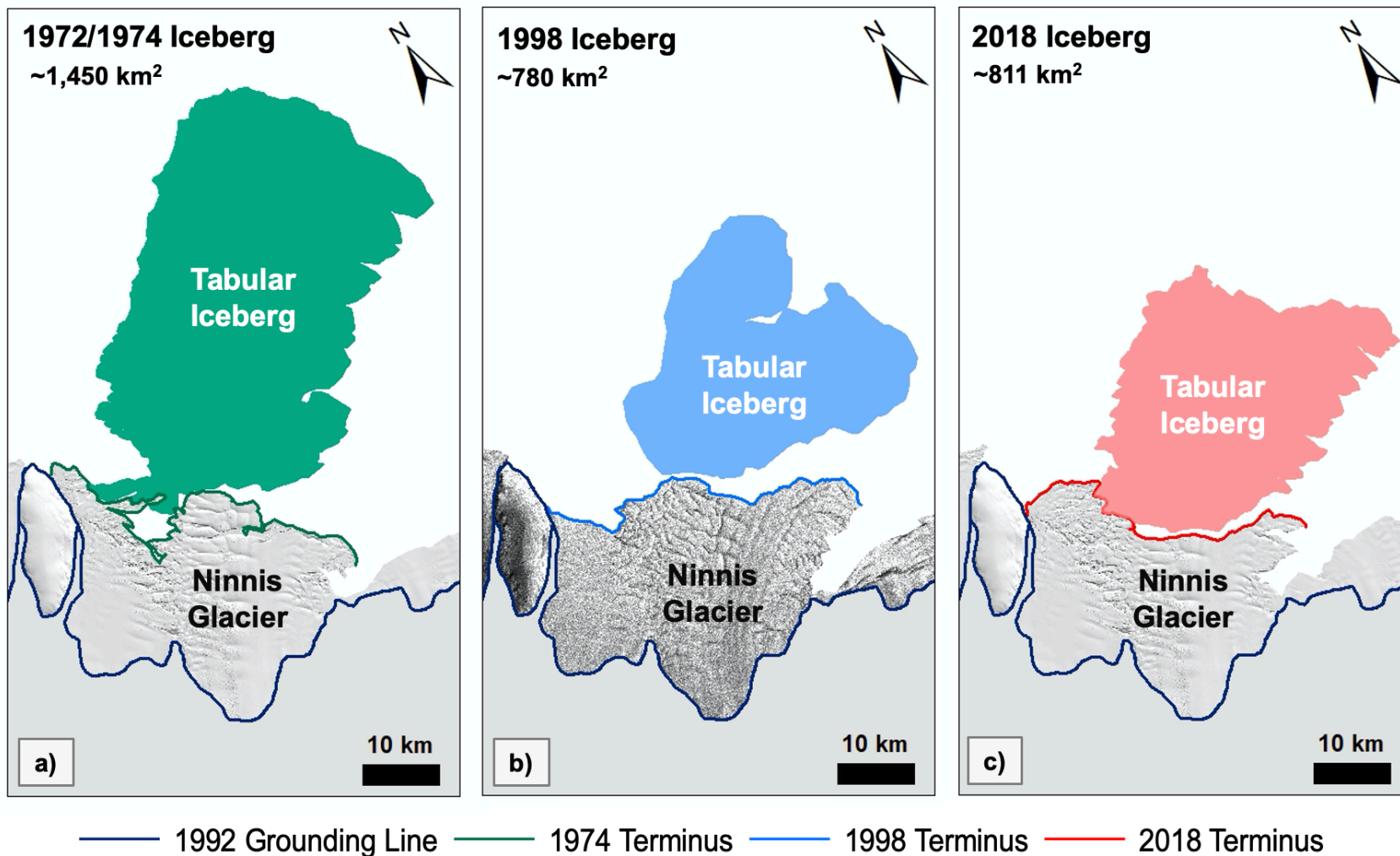
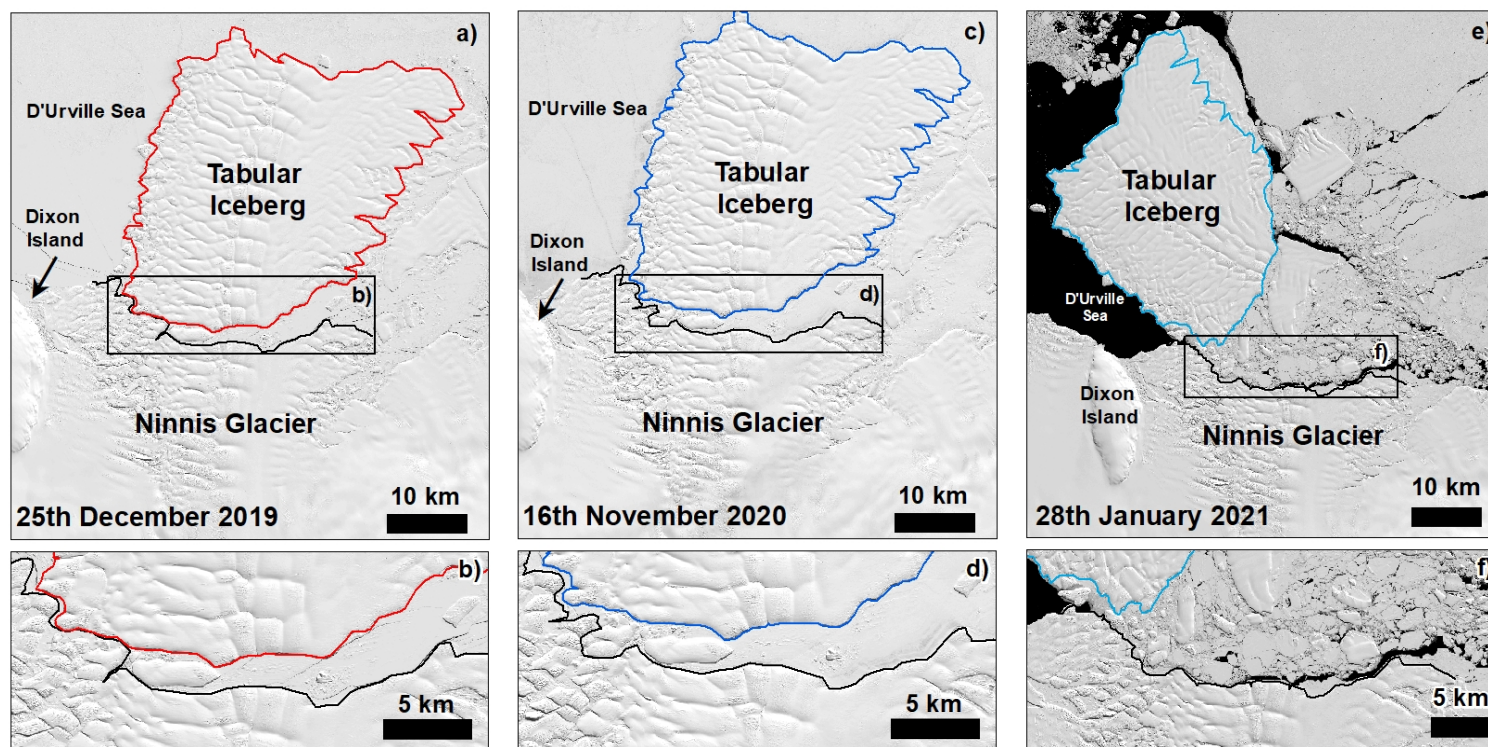


Figure 5.2: Visualisation of the differences in size tabular icebergs formed following the 1972/1974 (a), 1998 (b) and 2018 (c) calving events. Maps are overlain with the 1992 MEASUREs grounding line dataset and newly formed terminus positions.

The lack of imagery prior to 1963 also restricts the delineation of Ninnis' earlier terminus positions and more historic calving events. However, it has been estimated that Ninnis' tongue was at a similar position in 1913 compared to 1973 (Wendler et al., 1996; Frezzotti et al., 1998), punctuated by a major calving event in the 1950s which led to the detachment of a 1480 km^2 tabular iceberg (Frezzotti et al., 1998). This suggests that Ninnis has been undergoing a periodic cycle of consistent advance punctuated by large-scale calving events every 20-25 years: in the early 1950s, between 1971 and 1974, in 1998 and in 2018. Considering the large tabular icebergs produced following the 1950s ($1,480 \text{ km}^2$) and early 1970s ($1,450 \text{ km}^2$) calving events, it is possible that iceberg removal triggered a high magnitude increase in velocity, similar to that of the Cook West Glacier (Miles et al., 2018). As these icebergs were much larger than those produced following the 1998 and 2018 calving events, it is likely that ice flow velocity in the early 1950s and 1970s was much faster compared to post-1998 and post-2018 velocities.

During each re-advance phase, there is no evidence of major changes in ice tongue configuration to suggest that Ninnis has experienced irregular (non-cyclical) calving patterns, as experienced in the Amundsen Sea sector (Joughin et al., 2014; Favier et al., 2014; Miles et al., 2020) and the Brunt Ice Shelf in West Antarctica (Gudmundsson et al., 2017). This is supported by consistent average post-calving ice-front re-advance rates between 1974 and 1984 ($\sim 1.04 \text{ km a}^{-1}$) and between 1998 and 2000 ($\sim 1.46 \text{ km a}^{-1}$). However, the rate of re-advance rate immediately after the 2018 calving event is slightly slower than the previous two calving cycles ($\sim 0.67 \text{ m a}^{-1}$).

Monitoring of sub-annual terminus positions between March 2018 and March 2021 revealed no evidence of additional calving to account for the slower re-advance of the ice front relative to post-1998 calving re-advance. Rather, the negligible 0.02 km and 0.01 km retreats may be a result of terminus digitisation errors (Table 4.1; 4.2). Therefore, the slower recorded re-advance rates are attributed to the longevity of high sea ice concentrations proximal to the terminus and the newly formed tabular iceberg, which buttressed the re-advancing ice front (Figure 4.11e-j; Figure 5.3). Sea ice reduction is known to increase ice shelf vulnerability via ocean swell-induced flexure to the point of eventual break-up or disintegration (Massom et al., 2018). Notable examples include the catastrophic disintegration of the Larsen A, Larsen B and Wilkins ice shelves (Rott et al., 1996; Scambos et al., 2009; Padman et al. 2012; Massom et al., 2018). Thus, landfast sea ice buttressed Ninnis' advancing ice tongue and prohibited further rifting and calving in rheologically weaker areas of floating ice, as observed at neighbouring Mertz Glacier (Massom et al., 2010). This accounts for the slightly slower re-advance rate following the 2018 calving event (Table 4.2).



2019 Iceberg
 2020 Iceberg
 2021 Iceberg
 Terminus

Figure 5.3: Map depicting the positioning of the newly formed tabular iceberg following the 2018 calving event in 2019 (a-b), 2020 (c-d) and 2021 (e-f). Note the western portion of the tabular iceberg in 2019 and 2020 which remained proximal to the re-advancing terminus. By 2021 the tabular iceberg was released from Landfast sea ice extent, which persisted proximal to the newly formed terminus between 2018 and 2020 and started drifting towards the Ninnis Bank.

Additional buttressing can also be attributed directly to the tabular iceberg which remained in direct contact with the western side of the Ninnis terminus until January 2021 when sea ice proximal to the terminus broke-up and the tabular iceberg drifted away from the terminus (Figure 5.3a;b). This corresponded with, and may have enabled, a faster estimated rate of advance between November 2020 and January 2021 (1.3 km a^{-1}) compared to that between November 2019 and November 2020 (1.18 km a^{-1}) (Table 4.1) (Figure 4.8; 4.9; 5.3c). In contrast, the slower post-2018 calving re-advance may relate to the 2018 iceberg which calved closer to the grounding line than previous events (Figure 4.1; 5.2). This resulted in less freely-floating, unrestricted ice tongue area, and thus a greater proportion of the ice shelf is being influenced by resistive stresses at the grounding line (Sergienko and Wingham, 2019). Therefore, the slower re-advance may be a consequence of the remaining portion of the ice tongue being held back by the grounding zone, causing less ice to flow out of its embayment. This is supported with ice flow speed profiles 5 km up-ice and down-ice of the grounding line which are notably slower relative to the floating ice tongue (Table 4.6; 4.7). As floating ice shelves and tongues undergo destabilisation and acceleration from reduced resistive stresses at the grounding line, the slower re-advance reflects high resistive stresses and low driving and basal shear stresses at the grounding line (Hill et al., 2021). Therefore, Ninnis calved into a slower moving portion of ice in 2018 compared to previous calving events.

Although it is too early to speculate whether this slower re-advance is also indicative of external forcing contributing to changes in dynamics at Ninnis, future observations would help examine the rate of advance during periods of sea ice break-up and could be compared with previous calving cycles (See Arthur et al. (2021) and Miles et al. (2016)).

The style of calving events are similar across three cycles at Ninnis. These are characterised by large tabular iceberg detachment, iceberg drift from the newly formed terminus and eventual grounding on the Ninnis Bank where it often becomes enclosed by sea ice for several months (Massom, 2003). This differs to observations of disintegration-type calving events which have taken place on major Antarctic ice shelves, such as the Larsen A and B, Wilkins and Wordie Ice Shelves, and on outlet glaciers in Porpoise Bay, East Antarctica (Doake and Vaughan, 1991; Rott et al., 1996; Miles et al., 2017; Massom et al., 2018). These disintegration-type calving events have been attributed to both surface melt-induced hydrofracture and ocean forcing, which leads to increased flexure and eventual loss of ice (Banwell et al., 2019). Given Ninnis' observed periodic cycle of tabular calving events, it is highly unlikely that calving events are modulated by warmer-than-usual austral summers or intense ocean swell-induced flexure, as recorded elsewhere in Antarctica (Rignot et al., 2004; Miles et al., 2017; Massom et al.,

2018; Arthur et al., 2021). This reflects recent studies that have reported low thermal forcing temperatures in the coastal waters near Ninnis (Adusumilli et al., 2020), low mean surface melt rates (Trusel et al., 2013), negligible thinning of grounded ice (Schröder et al., 2019) and negligible retreat of Ninnis' grounding line (Konrad et al., 2018).

To summarise, Ninnis Glacier appears to undergo a 'natural' calving cycle with a 20-25 year periodicity modulated by rifting and reinforced by no discernible changes in crevassing across both grounded and floating portions of Ninnis Glacier. Based upon this assumption, it is predicted that the next calving event will occur sometime between 2038 and 2043.

5.3. The significance of structural glaciological changes at Ninnis Glacier

5.3.1. Linking structural glaciology to the 1998 and 2018 calving events

Satellite images between 1989 and 1997 reveal the precursors for the 1998 Ninnis calving event in the form of a central rift system emanating halfway up the eastern side of its tongue (Figure 4.10). On the western side of the ice tongue, surface fractures up to 1 km propagate eastwards at rates of up to 2 km a^{-1} prior to calving, eventually joining the central rift system. A loss of sea ice, which enclosed the rift between 1989 and 1991, was observed across the time-series. However, because there was no imagery at sub-annual resolution, it was impossible to elucidate whether sea ice reduction within the central rift accelerated their propagation in the build-up to complete detachment, as observed at the Brunt-Stancomb, George VI and Voyeykov ice shelves (Khazendar et al., 2009; Holt et al., 2013; Arthur et al., 2021). Fracture traces also remain consistent across the tongue between 1989 and 1997, although poor pixel resolution of SAR imagery restricted detailed mapping of changes in the size and extent of crevassing between the build-up to the 1998 calving event (between 1989 and 1997) (Figure 4.10).

In the build-up to the 2018 calving event (January 2016 – January 2018), a central rift system has been mapped in a similar location as the 1989-1997 rift (Figure 4.12). Although this initially suggests a natural rifting cycle in a pre-determined location, there are notable differences in the central rift systems mapped in build-up to the 1998 and 2018 calving events. For example, the time elapsing between rift formation and completions of propagation in the build-up to the 2018 calving is 7 years faster than that before the 1998 calving event. Furthermore, there are notable differences in morphology between the two rift systems (Figure 4.10; 4.12). The 1989-1997 rift formed along the eastern side of Ninnis' ice tongue, whereas the 2016-2018 rift formed a single large crack several kilometers from the edge of the ice tongue. However, evidence of

fracture traces superimposed with chaotic crevassing at the location in which both rifts initiated show that that this portion of the ice tongue was preconditioned to shearing and opening (Figure 4.10a; 4.11a;b; 4.12a) (Lhermitte et al., 2020).

Following the opening of the rift there was a reduction in the extent of crevassing in eastern sector of crevasse zone 1, suggesting that Ninnis' extensional flow regime and high strain rates contributed to both crevasse opening and rift opening (Figure 4.11a-f). Rift opening coincided with the largest acceleration in mean velocities on Ninnis' distal ice tongue ($+ 74.8 \text{ m a}^{-1}$) across the ITS_LIVE time series (Figure 4.16; 4.17). Moreover, at the location of rift opening, mean 2016 ice flow velocities were 51.6 % faster than those recorded on the Floating Ice portion of Flowline 1 (Table 4.5). This shows that major fluctuations in ice flow velocity coinciding with rift opening are not reflective of Ninnis' true velocity. Rather, they indicate positive feedback between structural weakening and ice flow velocity, as observed on the Twaites Ice Tongue between 2000 and 2018 (Miles et al., 2020).

Between 2016 and 2020, negligible changes in crevassing both up-ice and immediately down-ice of the grounding line show that the most discernible structural changes were restricted to a central rift system (Figure 4.11; 4.12). Furthermore, a lack of change in the size and extent of crevassing and fracturing between 2018 and 2020 suggests that Ninnis did not retreat into any dynamically important sectors of its ice tongue which would have reinforced further structural weakening (Fürst et al., 2016). Therefore, it is highly likely that in 2018 Ninnis Glacier calved into a section of "passive" ice shelf, which has no dynamical implications in response to its removal. This is due to its threshold in ice shelf buttressing not being exceeded (Fürst et al., 2016). In contrast, the loss of dynamically important ice has previously been observed at neighbouring Cook Glacier following a calving event between 1963 and 1974, culminating a doubling in velocity (Miles et al., 2017). Moreover, ice shelves in the Amundsen and Bellingshausen seas have almost no remaining sectors of passive ice, inferring that further ice shelf recession would result in major dynamical changes (Fürst et al., 2016).

The style of Ninnis' calving cycle terminated by large tabular iceberg detachment following rift development is analogous to that of neighbouring Mertz Glacier. In the build-up to a major calving event in February 2010, Mertz was subjected to cross-cutting rift formation emanating from the eastern and western sides of its ice tongue (Lescarmontier et al., 2015). However, the calving event was completed due to collision of the B9B iceberg, which calved from the Ross Ice Shelf in 1987 (Young et al., 2010). The formation of the eastern and western rifts in the early 1990s and in 2002 reveal that Mertz' calving dynamics culminated a prolonged period of rifting and that calving did not take place in the form of sudden disintegration such as the Brunt

Ice Shelf and the Thwaites Glacier Tongue (De Rydt et al., 2019; Miles et al., 2020). Previous calving events at Mertz are unknown but are postulated to have occurred between 1912 and 1958, therefore also suggesting a quasi-natural calving cycle (Giles, 2017).

5.3.2. Causes of rifting and calving at Ninnis Glacier

Various studies have investigated the mechanisms behind rift opening on ice tongues, most notably from Legresy et al. (2004) who attributed rift formation to tidal current circulation at Mertz Glacier. Similarly, Lescarmontier et al. (2015) used GPS data to deduce that rift opening on Mertz' floating ice tongue was mechanically driven by ocean swell vibrations. Therefore, considering Ninnis' similar bathymetric configuration to Mertz, near the George V Basin (Domack and Anderson, 1985), it is highly probable that Ninnis is exposed to similar oceanographic swell forcing in the build-up to rift opening. Additionally, it is postulated that rifting at Mertz is initiated at its margins following an exit from its fjord where ice is rheologically weaker and already superimposed with heavy crevassing and fracturing (Khazendar et al., 2007; Macgregor et al., 2012). As Ninnis follows a similar flow pattern, particularly on the eastern side of its ice tongue where there are no observed pinning points, the opening of Ninnis' central rift can also be attributed to increased susceptibility to tidal-induced flexure on unconstrained ice. This may have occurred once the tongue extended beyond a hinge zone, which is typically located down-ice of the grounding line (Lescarmontier et al., 2015). This predisposes the eastern side of the Ninnis ice tongue to tidal-induced rifting, whereas the western tongue is not as vulnerable owing to its pinning point with Dixon Island. This may explain why major rift systems only form on the eastern side of the tongue and in the exact down-ice location across two calving cycles.

It is also postulated that Mertz' calving cycle is naturally forced by shallow bed topography and shoals which modulate ice tongue advance and flow by either grounding or deflecting the advancing ice tongue, leading to initiation of major rifts and smaller, more localised sideways displacements (Massom et al., 2015; Wang et al., 2016). Therefore, more work is needed to investigate the bathymetric setting local to the rift zone on Ninnis and thus determine whether their openings are modulated by topography. This can be achieved by analysing sub-annual changes in horizontal (x-directional) ice velocity vectors following the point of contact of grounding to detect any deflection in ice flow and increased strain (Massom et al., 2015).

Finally, no water-filled crevasses or supraglacial lake systems, similar to that observed elsewhere in East Antarctica (Kingslake et al., 2017; Langley et al., 2016; Lenaerts et al., 2017; Stokes et al., 2019; Arthur et al., 2020;2021), were detected on Ninnis' floating tongue. As Ninnis experiences negligible surface melt fluxes (Trusel et al., 2013; Johnson et al., 2021), it

is extremely unlikely that surface melt-induced hydrofracture played any role in the opening of fractures or crevasses.

5.3.3. Controls on the timing of rifting and calving at Ninnis Glacier

Rifting processes observed in the same pre-determined position across two calving cycles (1989-1997 and 2016-2018) suggest that Ninnis is undergoing a periodic rifting cycle. However, it is important to note that the timing between rift opening and completion is variable and difficult to elucidate. For instance, the factors determining the timing of widening and propagation of rift systems for fast-flowing Antarctic outlet glaciers and ice streams are dependent on the localised stress regimes active at the time of opening, impacting their interaction with ocean swell and currents (Lescarmonnier et al., 2015). These processes leading up to rifting are non-linear and respond to evolving stress regimes induced by these tides (King et al., 2017). This means that no two rifting events are alike, whereby forecasting the speed of propagation and the precise timing of calving from the point of rift opening is impossible to accurately constrain. Mertz is a primary example of this, whereby a sudden change in stresses following collision from the B9B iceberg in February 2010 led to complete detachment (Massom et al., 2015).

This non-linear process may explain the 7-year difference in time elapsing between opening and completion across the two most recent calving cycles. It is likely that the next calving cycle may be modulated by identical processes of rifting. However, simulations of ocean water temperature are required to determine whether changes in local oceanographic conditions may lead to non-cyclical patterns of rift formation (Köhl, 2020).

5.4. Linking velocity fluctuations to calving at Ninnis

5.4.1. The 2008 minor break-up event

Between January 2007 and January 2008 a small 30 km² iceberg and a large assemblage of smaller icebergs calved from Ninnis' western ice tongue (Figure 4.6). It is likely that this small-scale localised calving event refers to a purported event by Rignot et al. (2019), whereby Ninnis accelerated following the break-up of its tongue in 2008. However, there were no direct observations suggesting when this acceleration took place, nor did the study suggest the magnitude of both the break-up and acceleration. Overall, the scale of calving was comparably smaller than large tabular iceberg calving events in the early 1970s, 1998 and 2018, so it cannot be treated as a period of important dynamical loss unless it triggered an acceleration. To determine Ninnis' dynamical response before, during and after the small-scale calving event in 2007, velocity mosaics between 2006-2011 were analysed (Section 4.4.1).

Analysis of short-term velocity trends revealed no evidence of a widespread speed-up before, during or after the small-scale calving (Table 4.3; 4.4) (Figure 4.13; 4.14; 4.15). The 6.2 % deceleration up-ice of the grounding line between 2008 and 2009, coinciding with the aftermath of the break-up event, confirms that ice calved from the tongue was 'passive' and did not exert changes in buttressing of inland ice (Fürst et al., 2016). Therefore, a reduction in longitudinal tensile stresses upon removal of the sections of ice likely initiated the deceleration. Negligible velocity changes have previously been recorded, both on West Antarctic and East Antarctic outlet glaciers, following periods of ice mass loss of greater magnitude than the purported break-up event by Rignot et al., (2019). Notably the Thwaites Glacier Tongue, which saw no significant changes in ice flow speed following a 75 km retreat phase, with the same occurring at the Voyeykov Ice Shelf following its disaggregation in 2007 (Miles et al., 2020; Arthur et al., 2021).

It is possible that Ninnis accelerated between 2009 and 2010 where there was a loss of pixel coverage, as it coincided with a 33.3 % increase in terminus advance rate. However, an overall 7.8 % deceleration (2006-2011) up-ice at the grounding line suggests that any acceleration between 2009 and 2010 would have been either short-lived or most likely not exceeded the 2006-2007 mean values. Velocity magnitudes on Flowline 1 and Flowline 2 exhibited negligible change on the floating ice tongue and distal portion between 2006 and 2011, showing that the localised calving event did not trigger a significant dynamical response on floating ice and near the terminus.

It is likely that higher velocity magnitudes on Flowline 2 reflect higher strain rates generated on the western ice tongue as it passed through its pinning point at Dixon Island, leading to positive feedbacks of acceleration reinforced by structural weakening (Rignot et al., 2006; MacGregor et al. 2012). Higher velocity magnitudes on Flowline 2 may also relate to the partial ungrounding of Ninnis' ice tongue from its pinning point in the shear zone to the west of Ninnis Glacier before 2008 (Figure 5.1). Ungrounding of glacier tongues and ice shelves from their pinning points are known to reinforce velocity acceleration when undergoing simultaneous ice thinning and grounding line retreat (Miles et al., 2021). However, altimetry surveys revealed thickening of Ninnis' floating ice between 2003 and 2008 (Pritchard et al., 2012). It is therefore unlikely that Ninnis was pre-disposed to positive feedbacks of velocity increase following the unpinning and break-up of its ice tongue (Rignot et al., 2006).

Overall, the localised calving between January 2007 and January 2008 on Ninnis' western tongue was minor in scale and did not trigger a pervasive acceleration. This suggests that the purported event by Rignot et al. (2019) did not constitute a noteworthy period of dynamical loss

as previously suggested. However, it is important to consider a potential velocity response following large-scale tabular icebergs at Ninnis.

5.4.2. Velocities before (2013-2018) and after (2018-2021) the 2018 calving event

Prior to the 2018 calving event (2013-2018), Ninnis underwent negligible change in velocity up-ice (+0.6 %) and down-ice (+0.4 %) of the grounding line, whilst the highest magnitude changes occurred on Ninnis' distal ice tongue between 2015 and 2016. However, the sudden +74.8 % acceleration in ice flow coincides with the rapid formation and propagation of its central rift system and does not reflect the true velocity of Ninnis' ice tongue (Figure 4.16; 4.17d) (Table 9). This led to rotation of the tongue at rates of velocity in excess of $2,100 \text{ m a}^{-1}$ (Table 4.5; Figure 4.16; 4.17). As this acceleration took place whilst grounding line velocities showed no simultaneous speed-up, heavy rifting of Ninnis' ice tongue clearly took place in a sector of 'passive ice' (Fürst et al., 2016). This suggests that ice which underwent rifting between 2016 and 2018 did not provide an important buttressing effect on inland ice (Fürst et al., 2016). Similar behaviour has been observed on the former Mertz Glacier Tongue, whereby ice flow velocities jumped from 700 to $2,400 \text{ m a}^{-1}$ when its rift opened in 2000 (Legresy et al., 2014). This was linked to modulation of ice flow velocity from the direction of tidal currents and the lateral drag exerted from the walls of its fjord, suggesting that changes in velocity on the tongue at Mertz and Ninnis are indicative of rift openings alone (Legresy et al., 2014). Given the low surface melt fluxes, negligible grounding line migration between 2010 and 2018 and low thermal forcing temperatures reported at Ninnis (Trusel et al. 2013; Konrad et al., 2018; Adusumilli et al., 2020), the 2016 acceleration cannot be attributed to external forcing factors.

Ninnis' distal tongue decelerated by 35.9 % between 2016 and 2017 and a further 3.6 % between 2017 and 2018, whilst grounding line velocities underwent negligible change within the same time period. This indicates that the 2016 acceleration did not trigger a speed-up of the advancing terminus in the build-up to calving, rather it reflected rapid change in the structural integrity of the ice tongue (Legresy et al., 2014). However, further analysis was still required to examine short-term velocity trends in the years following calving.

Analysis of sub-annual velocity mosaics from the Sentinel-2A satellite reveal an overall trend of deceleration across both grounded and floating portions of Ninnis Glacier between 2018 and 2020, immediately after the calving event. Negligible changes in velocity upstream of the grounding line shows that the calving of Ninnis' tongue in 2018 did not result in the loss of any dynamically important ice and that the tongue was uncoupled from grounded ice (Fürst et al., 2016). This is typical behaviour for large East Antarctic outlet glaciers that undergo natural

calving cycles (Giles, 2017; Miles et al., 2018; Rignot et al., 2019). While a major calving event of the Cook West Ice Shelf between 1963 and 1973 led to the retreat into a dynamically important sector of its embayment (Fürst et al., 2016; Miles et al., 2018), negligible change in grounding line position between 2010 and 2018 and stabilisation of its re-advancing ice shelf did not suggest susceptibility to MISI (Pattyn, 2018; Konrad et al., 2018). As Ninnis' grounding line also underwent negligible migration between 2010 and 2018, the overall reduction in velocity on grounded ice does not infer any imminent susceptibility to MISI or further grounding line retreat (Pattyn, 2018; Konrad et al., 2018; Morlighem et al., 2020). However, further work is needed to examine rates of ice surface elevation change on Ninnis' ice tongue to determine whether thinning may trigger future grounding line retreat, as observed at Totten Glacier between 1996 and 2013 (Li et al., 2015). Further work should also carefully monitor the future state of Ninnis' ice tongue and whether future calving events form new terminus positions further up ice, as observed at Cook Glacier (Miles et al., 2018).

The only noticeable acceleration took place in March 2020 (+ 6.6 %) on the distal portion of the flowline. However, this corresponded with further rotation of the tabular iceberg between January 2019 and November 2020 (Fig.5.2a;b). Before this, sea ice proximal to the newly formed terminus provided a buttressing effect on the re-advancing ice front and suppressed ice flow velocities between 2018 and 2019 (Figure 5.2a;b; 5.3) (Schlemm and Levermann, 2021). However, the tabular iceberg detached from the re-advancing terminus and began drifting towards the Ninnis Bank following the break-up of protective sea ice in January 2021 (Fig. 5.2c). This coincides with a near complete loss of pixel coverage from the Sentinel 2-A satellite in February 2021 (Fig.5.2c; 4.20c). Despite this loss of sea ice, pervasive deceleration at Ninnis persisted between November 2020 and June 2021.

Although Ninnis has been identified as a sector of risk, owing to its topographical configuration analogous to Thwaites and Pine Island Glaciers in West Antarctica (Rignot et al., 2019), there is no evidence to suggest instability in the immediate future. Further work is essential to observe its future changes in terminus position, structural glaciology and velocity over its current calving cycle.

5.5. A review of recent observations of Ninnis Glacier by Cheng et al. (2021)

This section reviews a recently published paper by Cheng et al. (2021) which presented long-term remote sensing observations of Ninnis Glacier's calving cycle over the last 60 years. This paper was published after this thesis was initially drafted and after the data analysis had been completed. The study combined satellite and aerial imagery with historical field measurements

to produce a long-term time-series of terminus position change between 1963 and 2021, in other words, it had aims very similar to that of this thesis. Notwithstanding this, there are some key discrepancies between their work and the work presented in this thesis, which is discussed below.

Terminus position mapping from Cheng et al. (2021) indicated that Ninnis experienced three major calving events (1980-1982, 1998 and 2018), each culminating the propagation of a central rift system and tabular iceberg detachment upon their completion (Figure 5.4). The rifts identified across two calving cycles (1989-1998) and (2016-2018) formed in a pre-determined location, similar to observations made in this thesis (Figure 5.4). This was attributed to continuous advection of Ninnis' ice tongue and long-term tidal currents (Cheng et al., 2021).

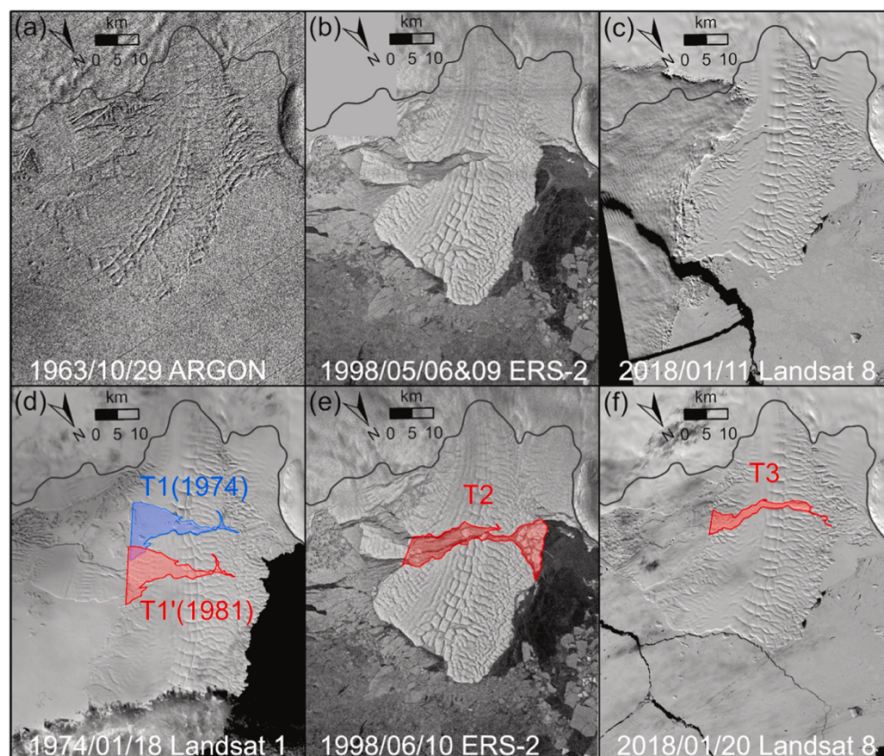


Figure 5.4: Time-series of area change at Ninnis Glacier between 1963 and 2018. Note the calving events between 1980 and 1982, in 1998 and 2018 (from Cheng et al., 2021).

The time-series of calving events presented by Cheng et al. (2021) also points towards an acceleration of its calving cycle over time, with the first cycle taking place over a ~23-year time period and the last two calving cycles averaging ~18.5 years (Figure 5.5). The first calving event, between 1980 and 1982, was estimated from analysis of satellite imagery and field

observations made from the 1979 Deep Freeze Expedition (Anderson et al., 1980; Frezzotti et al., 1998). Additionally, they suggest the up-ice location of Ninnis' central rift system during the 2016-2018 calving cycle was located closer to the grounding line compared to that of the 1989-1998 calving cycle (Figure 5.4).

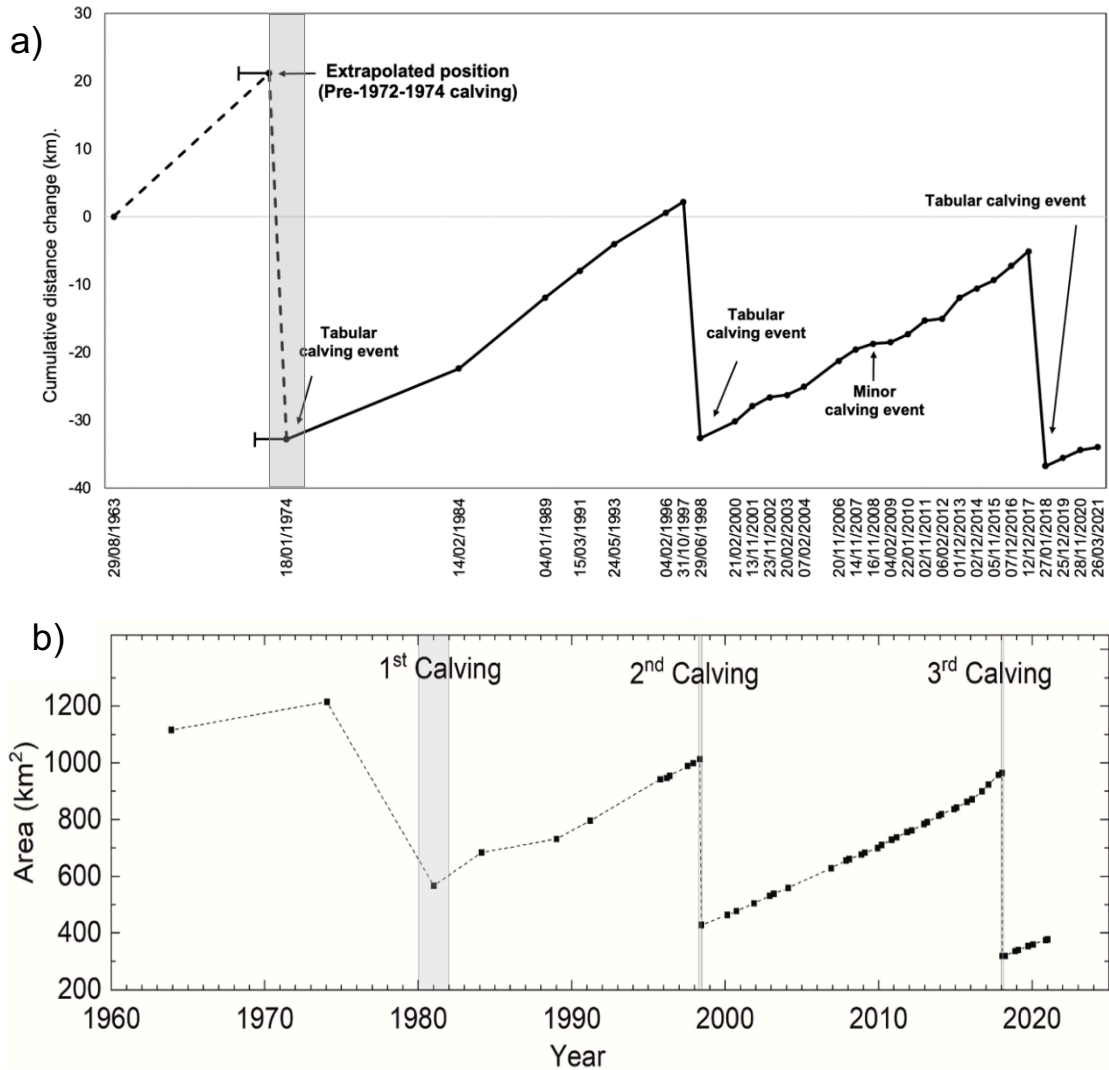


Figure 5.5: Reconstruction of Ninnis Glacier's calving cycle between 1963 and 2021. Panel a depicts the time-series of terminus position change (1963-2021) presented in this thesis (Figure 4.2). Panel b depicts the time-series of area (km²) change (1963-2021) at Ninnis Glacier presented by Cheng et al. (2021). Note the differences in the proposed timing of the first calving event between panels a and b.

This thesis agrees with Cheng et al.'s results which stated that the 2016-2018 rift position was closer to the grounding line relative to that in 1989-1998, whilst also acknowledging significant differences in time elapsing between rift formation and completion across the two calving cycles. However, some of the key conclusions presented in Cheng et al. (2021) differ to those proposed in this thesis. Notably the conclusion that Ninnis' cycle has accelerated over time. The validity of this conclusions hangs on the timing of the first calving event described in their study (1980-1982), which was based entirely on prior estimations made by Frezzotti et al. (1998). No detailed observations were made by either Frezzotti et al. (1998) or by Cheng et al. (2021) to accurately constrain this calving event. Instead, the Frezzotti et al., (1998) work relies on a report from a ship survey that skirted the region, but which did not enter the rift areas (Anderson et al., 1980), meaning that the timing of the first calving cycle is not well constrained in any of those previous studies. Analysis of the 1974 Landsat MSS image by Cheng et al. (2021) described a large portion of its heavily rifted ice tongue still attached to Ninnis' central flow unit, representing Ninnis' most advanced position in the time-series. However, that study did not account for the complex glaciological and sea ice conditions present at western shear zone in 1974.

Detailed assessment of the 1974 Landsat image presented in this thesis delineated a new terminus position amongst intense crevassing, rifting and amalgamations of small, calved icebergs enclosed in MYLI (Figure 4.3; 4.4; 5.1). It is likely that extensive MYLI present within the rift was mapped as consolidated ice by Cheng et al. (2021), meaning that Ninnis' ice tongue remained attached to the true terminus in 1974. Although the timing of the second (June 1998) and third (January 2018) calving events agree with findings presented in this thesis, disagreements on the timing of the first calving event have resulted in clear differences when describing the periodicity between calving events (Figure 5.5) (~18.5-23 years by Cheng et al. (2021) and 20-25 years in this study). This is important when considering whether Ninnis has been subject to an acceleration in its calving cycle and whether external forcing factors have evolved and caused a difference in its most recent calving cycle. However, detailed analysis presented in this thesis strongly suggests that Ninnis Glacier has undergone a 20–25-year calving cycle (Figure 5.5).

Both this thesis and the study by Cheng et al. (2021) acknowledges the need for more observations on the evolution of Ninnis' ice tongue, oceanographic conditions local to Ninnis, up-to-date records of ice surface elevation change, and future sea ice concentrations. This will provide valuable data in determining if Ninnis is in fact currently responding to external forcing.

5.6. Limitations.

There are several limitations associated with the methods employed in this study, which are briefly discussed here.

5.6.1. Availability of satellite imagery (1963-1984).

This study analysed a substantial number of satellite and aerial Images between 1963 and 2021. However, only two images were available during the first calving cycle at Ninnis Glacier. Additional imagery would have been valuable in quantifying inter-annual cumulative terminus position change in the build-up to the 1970s calving event, whilst also observing the time elapsing between opening and completion. Observations of terminus position change at neighbouring Mertz Glacier obtained a historical map from 1914 and oblique aerial imagery taken in 1947 during 'Operation Highjump' to extend the time-series further back in time (Giles, 2017). However, no aerial sorties were ever made over Ninnis Glacier during Operation Highjump.

Large time-series gaps could not be accounted for between the 1974 Landsat TM and 1984 Soyuz KATE images. This would have provided critical evidence for determining the timing of the first calving event, estimated between 1980 and 1982 in previous studies (Frezzotti et al., 1998), but dated to between 1972 and 1974 in this thesis. Images in the early 1980s would have enabled spatial analysis surrounding Ninnis glacier to determine whether previous observations described the 1980-1982 calving event during after its release from sea ice.

5.6.2. Structural glaciological analysis of the second calving cycle.

A lack of extensive Landsat image coverage between 1989 and 2000 restricted detailed mapping of changes in the size and extent of crevasse zones before, during and after the 1998 calving event. Although two Landsat images (1989; 1991) and four SAR images (1993; 1996; 1997; 1998) were obtained during this time period, poor pixel coverage from the SAR impeded accurate delineation of crevasses. Availability of Landsat imagery during this time-period would have provided suitable pixel resolution for extensive structural glaciological and spatial mapping at Ninnis Glacier, producing detailed comparisons of maps between two calving cycles.

5.6.3. Secondary datasets.

Due to the time-frame of the project and significant disruption due to the Covid-19 pandemic, this thesis was restricted to performing terminus, structural glaciological and velocity mapping at Ninnis Glacier, so the detailed analysis of secondary datasets was beyond the scope of the project. However, as a natural 20-25 year calving cycle was suggested, the need for detailed analysis of secondary datasets would not have been necessary. This thesis contributed to current knowledge of recent East Antarctic outlet glacier behaviour by presenting a long-term time-series of terminus position change and structural glaciological maps which detailed the timing and styles of calving events.

5.7. Further research.

An obvious avenue for further work would be to analyse available secondary datasets such as surface elevation change and surface melt fluxes. This might provide indications of any thinning in the region and how that might relate to the ice tongue evolution and calving cycle. However, detailed analysis of available data was beyond the scope of a 1-year investigation. This provides scope for future studies to reduce key gaps in knowledge surrounding recent change at Ninnis Glacier.

5.7.1. Strain rates

Continuation of this research can be performed by calculating horizontal and longitudinal strain rates at Ninnis Glacier using the Global Land Ice Velocity Extraction from Landsat 8 (GoLIVE) (Fahnestock et al., 2016; Scambos et al., 2016). As the rates of calving for floating ice tongues are modulated by strain rates from ice flow (Alley et al., 2018; De Rydt et al., 2018), this would enable a greater understanding behind the dynamical processes which took place on the Ninnis' tongue in the build-up to calving.

5.7.2. Grounding line data

This research would have benefitted significantly from additional data depicting grounding line position at Ninnis Glacier, providing a long-term time-series of grounding line migration to correlate with available figures in the literature (Konrad et al., 2018). Additional grounding line positions can be delineated from the REMA DEM (Howat et al.,

2018), interferometric synthetic-aperture radar (InSAR) data (Mohajerani et al., 2021) and by detecting the grounding line inflexion point in Landsat imagery (Christie et al., 2016); but all these methods are subject to uncertainty and tend to have slightly different results. Therefore, a consistent method for long-term observation may be helpful to understand how ice tongue changes may influence any movement of the grounding line.

5.7.3. Sea ice

Detailed analysis of sea ice concentrations offshore of Ninnis Glacier would allow direct comparisons to be observed with changes in terminus position and ice flow velocity (Arthur et al., 2021). Average daily and monthly anomalies from the Advanced Microwave Scanning Radiometer – EOS (AMSR-E) and AMSR-2 provide an ideal dataset for examining whether the break-up of sea ice triggered the 2018 calving event.

5.7.4. Ocean circulation

The scope to investigate the local influences of ocean temperature on terminus position change at Ninnis was well beyond that of a one-year investigation due to the complexity of obtaining data on surface and sub-surface ocean temperatures. However, oceanographic profiles of temperature and salinity would provide valuable data for warm water transport underneath Ninnis and ascertain whether basal melt from mCDW intrusion contributed to the 2018 calving event (Rintoul et al., 2019).

5.7.5. Numerical Modelling

Finally, this study would benefit from sensitivity analysis to assess potential dynamical response to changes in the extent of Ninnis' ice tongue. For example, using the *Úa* flow model, previous studies have simulated singular, and a combination of, scenarios (e.g., ice shelf thinning, grounding line retreat, ungrounding of pinning points and ice shelf/tongue removal) to estimate whether calving may trigger a widespread velocity response (Hill et al., 2021; Miles et al., 2021). It could also be used to test the sensitivity of Ninnis Glacier to calving events that might retreat closer to the grounding line, as has been performed at Petermann Glacier, Greenland (Hill et al., 2021). Considering the large size of Ninnis' catchment and the location of its grounding line atop a retrograde slope, we need improved datasets detailing Ninnis' subglacial bed topography. This will help to reduce uncertainties when simulating grounding line retreat and provide insights into its susceptibility to Marine Ice Sheet Instability and future contribution to global mean SLR (Morlighem et al., 2020).

Chapter 6: Conclusions

This study has presented up-to-date remote sensing observations at Ninnis Glacier, East Antarctica. Ninnis was considered a target glacier urgently requiring new observations, owing to its large catchment actively draining the Wilkes Subglacial Basin (WSB) and with a grounding line located atop a retrograde bed slope (Mengel and Levermann, 2014; Rignot et al., 2019; Morlighem et al., 2020). Therefore, observations detailing its recent behaviour were necessary to determine whether Ninnis had undergone any significant change or might be susceptible to future Marine Ice Sheet Instability (Pattyn, 2018; Morlighem et al., 2020). This study combined terminus position mapping, structural glaciological mapping and analysis of ice flow velocities at Ninnis Glacier.

Terminus mapping results captured three major calving events which took place between 1972 and 1974, in 1998, and in 2018. The timing of the first calving event, estimated to have taken place between 1980 and 1982 by Frezzotti et al. (1998), was revised to the early 1970s based on detailed analysis of a 1974 Landsat image. This study therefore concludes that Ninnis is currently undergoing a naturally occurring calving cycle, with each event occurring at a periodicity of 20-25 years. Each event culminated in the detachment of large tabular icebergs and formed new up-ice terminus positions that were 28, 29 and 25 km downstream of the 1992 grounding line, respectively. In addition, a localised calving event took place on the western portion of Ninnis' tongue between January 2007 and January 2008. This is believed to be the event described by Rignot et al., (2018), whereby Ninnis underwent an acceleration following the break-up of its tongue in 2008. However, no direct observations were presented by Rignot et al. (2018) to support this, and no evidence of localised acceleration was found in this thesis. Overall, this event was significantly smaller compared to large-scale tabular calving events, reinforced with ice flow velocity profiles on Ninnis' grounded and floating ice which showed no discernible changes between 2006 and 2011.

Structural analysis captured the precursors to cyclical tabular calving events at Ninnis in the form of a transverse rift system on Ninnis' ice tongue which formed in almost identical locations across two calving cycles (1989-1997 and 2016-2018). Furthermore, extensive mapping of crevasse zones revealed no changes up-ice of the grounding line between 2016 and 2020, with the largest changes in crevassing taking place on Ninnis' tongue in response to rift formation. This shows that Ninnis did not undergo any significant dynamical changes in response to the 2018 calving event. In addition, ice flow velocities analysed before and during the 2018 calving event also revealed no significant changes upstream of the grounding line. The largest velocity fluctuation (+74 %) took place on the distal tongue between 2015 and 2016. However, this

acceleration does not represent the true velocity of Ninnis' ice tongue as it corresponded with rotation of Ninnis' ice tongue following the rapid opening and widening of its central rift in the build-up to the January 2018 calving event. Velocity analysis following the 2018 calving event (2018-2021) revealed an overall trend of deceleration across all sectors of Ninnis Glacier. The notable decelerations down-ice of the grounding line indicated that the large-scale tabular calving event in 2018 did not result in loss of dynamically important ice and, rather a loss of 'passive ice' (Fürst et al., 2016). The post-2018 calving event deceleration therefore demonstrates that Ninnis' ice tongue did not exert a significant buttressing effect on inland ice. Considering Ninnis' grounding line positioning near a retrograde slope (Mengel and Levermann, 2014; Rignot et al., 2019; Morlighem et al., 2020), this provides important evidence that Ninnis is not yet susceptible to MISI (Pattyn, 2018).

It is crucial that further observations are carried out at Ninnis Glacier to establish any future changes in dynamics, particularly to consolidate observations and modelling results presented in this thesis and recently by Cheng et al. (2021). Future observations should focus on identifying changes such as rapid velocity fluctuations of inland ice, slowed rates of re-advance and evidence of non-cyclical calving events. In addition, ice flow models can be used to assess the sensitivity of Ninnis' ice tongue to future calving events and whether this may induce a major dynamical response, such as increases in velocity, grounding line retreat, loss of grounded ice (Hill et al., 2021).

Overall, observations in this study conclude that Ninnis Glacier has remained stable between 1963 and 2021, undergoing no discernible dynamical changes indicative of external forcing factors (e.g., ocean currents or surface melt) (Pritchard et al., 2012; Trusel et al., 2012; Depoorter et al., 2013; Adusumilli et al., 2020). However, suggestions for further work outlined in section 5.8 can be used as a framework for increasing our understanding of forcing factors at Ninnis Glacier and potential changes in the ocean-climate system that may trigger future changes in its long-term dynamics. Considering the role of Ninnis Glacier in draining the Wilkes Subglacial Basin (WSB), this is also important for understanding how Ninnis will respond to future ocean-climate changes and its potential contribution to global mean sea level rise (Mengel and Levermann, 2014).

References:

- Adusumilli, S., Fricker, H.A., Medley, B., Padman, L., Siegfried, M.R. (2020) 'Interannual variations in meltwater input to the Southern Ocean from the Antarctic ice shelves'. *Nature*, 13(9), 616-620.
- Aitken, A.R.A., Roberts, J.L., Ommen, T.D. van, Young, D.A., Gолledge, N.R., Greenbaum, J.S., Blankenship, D.D. and Siegert, M.J. (2016) 'Repeated large-scale retreat and advance of Totten Glacier indicated by inland bed erosion', *Nature*, 533(7603), pp. 385–389.
- Alley, K.E., Scambos, T.A., Siegfried, M.R. and Fricker, H.A. (2016) 'Impacts of warm water on Antarctic ice shelf stability through basal channel formation', *Nature Geoscience*, 9(4), pp. 290–293.
- Amundson, J.M., Fahnestock, M., Truffer, M., Brown, J., Lüthi, M.P. and Motyka, R.J. (2010) 'Ice mélange dynamics and implications for terminus stability, Jakobshavn Isbræ, Greenland', *Journal of Geophysical Research: Earth Surface*, 115(F1).
- Anderson, J.B., Balshaw, K., Domack, E. and Kurtz, D. (1980) 'Observations of Sediment-laden Icebergs in Antarctic Waters: Implications to Glacial Erosion and Transport'. *Journal of Glaciology*, 25(93), pp. 387-396
- Arthur, J.F., Stokes, C.R., Jamieson, S.S.R., Carr, J.R. and Leeson, A.A. (2020) 'Distribution and seasonal evolution of supraglacial lakes on Shackleton Ice Shelf, East Antarctica', *The Cryosphere*, 14(11), pp. 4103–4120.
- Arthur, J.F., Stokes, C.R., Jamieson, S.S.R., Miles, B.W.J., Carr, J.R. and Leeson, A.A. (2021) 'The triggers of the disaggregation of Voyeykov Ice Shelf (2007), Wilkes Land, East Antarctica, and its subsequent evolution', *Journal of Glaciology*, 67(265), pp. 933–951.
- Bamber J., Westaway, R.M., Marzeion, B. and Wouters, B (2018) 'The land ice contribution to sea level during the satellite era'. *Environmental Research Letters*, 13(6), 1-21
- Bamber, J.L., Westaway, R.M., Marzeion, B. and Wouters, B. (2018) 'The land ice contribution to sea level during the satellite era', *Environmental Research Letters*, 13(6), p. 063008.
- Banwell, A.F., MacAyeal, D.R. and Sergienko, O.V. (2013) 'Breakup of the Larsen B Ice Shelf triggered by chain reaction drainage of supraglacial lakes', *Geophysical Research Letters*, 40(22), pp. 5872–5876.
- Banwell, A.F., Willis, I.C., Macdonald, G.J., Goodsell, B. and MacAyeal, D.R. (2019) 'Direct measurements of ice-shelf flexure caused by surface meltwater ponding and drainage', *Nature Communications*, 10(1), p. 730.
- Bindoff, N.L., Rosenberg, M.A. and Warner, M.J. (2000) 'On the circulation and water masses over the Antarctic continental slope and rise between 80 and 150°E', *Deep Sea Research Part II: Topical Studies in Oceanography*, 47(12–13), pp. 2299–2326.
- Bindschadler, R., Vornberger, P., Fleming, A., Fox, A., Mullins, J., Binnie, D., Paulsen, S.J., Granneman, B. and Gorodetzky, D. (2008) 'The Landsat Image Mosaic of Antarctica', *Remote Sensing of Environment*, 112(12), pp. 4214–4226.

- Bolch, T., Yao, T., Kang, S., Buchroithner, M.F., Scherer, D., Maussion, F., Huintjes, E. and Schneider, C. (2010) 'A glacier inventory for the western Nyainqentanglha Range and the Nam Co Basin, Tibet, and glacier changes 1976–2009', *The Cryosphere*, 4(3), pp. 419–433.
- Brancato, V., Rignot, E., Milillo, P., Morlighem, M., Mouginot, J., An, L., Scheuchl, B., Jeong, S., Rizzoli, P., Bueso Bello, J.L. and Prats-Iraola, P. (2020) 'Grounding Line Retreat of Denman Glacier, East Antarctica, Measured With COSMO-SkyMed Radar Interferometry Data', *Geophysical Research Letters*, 47(7), p. e2019GL086291.
- Cape, M.R., Vernet, M., Skvarca, P., Marinsek, S., Scambos, T. and Domack, E. (2015) 'Foehn winds link climate-driven warming to ice shelf evolution in Antarctica', *Journal of Geophysical Research: Atmospheres*, 120(21), p. 11,037–11,057.
- Cheng, Y., Xia, M., Qiao, G., Li, Y., Hai, G. and Lv, D. (2021) 'Calving cycle of Ninnis Glacier over the last 60 years', *International Journal of Applied Earth Observation and Geoinformation*, 105, p. 102612.
- Christie, F.D.W., Bingham, R.G., Gourmelen, N., Tett, S.F.B. and Muto, A. (2016) 'Four-decade record of pervasive grounding line retreat along the Bellingshausen margin of West Antarctica', *Geophysical Research Letters*, 43(11), pp. 5741–5749. doi:10.1002/2016GL068972.
- Church, J.A., Clark, P.U., Caenave, A., Gregory, J.M., Jevrejeva, S., Levermann, A., Merrifield, M.A., Milne, G.A., Nerem, R.S., Nunn, P.D., Payne, A.J., Pfeffer, W.T., Stammer, D., Unnikrishnan, A.S. (2013) 'Sea Level Change'. In: Stocker, T.F., Qin, D., Plattner, G.K., Tignor, M., Allen, S.K., Boschung, J., Nauels, A., Xia, Y., Bex, V. and Midgley, P.M (eds) *Climate Change 2013: The Physical Science Basis. Contribution of Working Group I to the Fifth Assessment Report of the Intergovernmental Panel on Climate Change*. Cambridge, United Kingdom and New York, NY, USA: Cambridge University Press, 1137–1215.
- Cook, A.J., Fox, A.J., Vaughan, D.G. and Ferrigno, J.G. (2005) 'Retreating Glacier Fronts on the Antarctic Peninsula over the Past Half-Century', *Science*, 308(5721), pp. 541–544.
- Cook, A.J., Holland, P.R., Meredith, M.P., Murray, T., Luckman, A. and Vaughan, D.G. (2016) 'Ocean forcing of glacier retreat in the western Antarctic Peninsula', *Science*, 353(6296), pp. 283–286.
- Cook, C.P., van de Fliert, T., Williams, T., Hemming, S.R., Iwai, M., Kobayashi, M., Jimenez-Espejo, F.J., Escutia, C., González, J.J., Khim, B.-K., McKay, R.M., Passchier, S., Bohaty, S.M., Riesselman, C.R., Tauxe, L., Sugisaki, S., Galindo, A.L., Patterson, M.O., Sangiorgi, F., Pierce, E.L., Brinkhuis, H., Klaus, A., Fehr, A., Bendle, J.A.P., Bijl, P.K., Carr, S.A., Dunbar, R.B., Flores, J.A., Hayden, T.G., Katsuki, K., Kong, G.S., Nakai, M., Olney, M.P., Pekar, S.F., Pross, J., Röhl, U., Sakai, T., Shrivastava, P.K., Stickley, C.E., Tuo, S., Welsh, K. and Yamane, M. (2013) 'Dynamic behaviour of the East Antarctic ice sheet during Pliocene warmth', *Nature Geoscience*, 6(9), pp. 765–769.
- De Rydt, J., Gudmundsson, G.H., Nagler, T. and Wuite, J. (2019) 'Calving cycle of the Brunt Ice Shelf, Antarctica, driven by changes in ice shelf geometry', *The Cryosphere*, 13(10), pp. 2771–2787.
- De Rydt, J., Gudmundsson, G.H., Nagler, T., Wuite, J. and King, E.C. (2018) 'Recent rift formation and impact on the structural integrity of the Brunt Ice Shelf, East Antarctica', *The Cryosphere*, 12(2), pp. 505–520.

- DeBeer, C.M. and Sharp, M.J. (2009) 'Topographic influences on recent changes of very small glaciers in the Monashee Mountains, British Columbia, Canada', *Journal of Glaciology*, 55(192), pp. 691–700.
- DeConto, R.M. and Pollard, D. (2016) 'Contribution of Antarctica to past and future sea-level rise', *Nature*, 531(7596), pp. 591–597.
- DeConto, R.M., Pollard, D., Alley, R.B., Velicogna, I., Gasson, E., Gomez, N., Sadai, S., Condrón, A., Gilford, D.M., Ashe, E.L., Kopp, R.E., Li, D. and Dutton, A. (2021) 'The Paris Climate Agreement and future sea-level rise from Antarctica', *Nature*, 593(7857), pp. 83–89.
- Dell, R.L., Banwell, A.F., Willis, I.C., Arnold, N.S., Halberstadt, A.R.W., Chudley, T.R. and Pritchard, H.D. (2021) 'Supervised classification of slush and ponded water on Antarctic ice shelves using Landsat 8 imagery', *Journal of Glaciology*, pp. 1–14.
- Depoorter, M.A., Bamber, J.L., Griggs, J.A., Lenaerts, J.T.M., Ligtenberg, S.R.M., van den Broeke, M.R. and Moholdt, G. (2013) 'Calving fluxes and basal melt rates of Antarctic ice shelves', *Nature*, 502(7469), pp. 89–92.
- Dinniman, M.S., Klinck, J.M. and Smith, W.O. (2003) 'Cross-shelf exchange in a model of the Ross Sea circulation and biogeochemistry', *Deep Sea Research Part II: Topical Studies in Oceanography*, 50(22–26), pp. 3103–3120.
- Dinniman, M.S., Klinck, J.M. and Hofmann, E.E. (2012) 'Sensitivity of Circumpolar Deep Water Transport and Ice Shelf Basal Melt along the West Antarctic Peninsula to Changes in the Winds', *Journal of Climate*, 25(14), pp. 4799–4816.
- Doake, C.S.M. and Vaughan, D.G. (1991) 'Rapid disintegration of the Wordie Ice Shelf in response to atmospheric warming', *Nature*, 350(6316), pp. 328–330.
- Domack, E.W. and Anderson, J.B. (1983). 'Marine geology of the George V continental margin: combined results of Deep Freeze 79 and the 1911-14 Australian Expedition', in Oliver, R.L. and Jago, J.B., (eds) *Antarctic earth science*. Cambridge: Cambridge University Press, pp.402-406.
- Dow, C.F., Lee, W.S., Greenbaum, J.S., Greene, C.A., Blankenship, D.D., Poinar, K., Forrest, A.L., Young, D.A. and Zappa, C.J. (no date) 'Basal channels drive active surface hydrology and transverse ice shelf fracture', *Science Advances*, 4(6), p. eaao7212.
- Fahnestock, M., Scambos, T., Moon, T., Gardner, A., Haran, T. and Klinger, M. (2016) 'Rapid large-area mapping of ice flow using Landsat 8', *Remote Sensing of Environment*, 185, pp. 84–94. doi:10.1016/j.rse.2015.11.023.
- Favier, L., Durand, G., Cornford, S.L., Gudmundsson, G.H., Gagliardini, O., Gillet-Chaulet, F., Zwinger, T., Payne, A.J. and Le Brocq, A.M. (2014) 'Retreat of Pine Island Glacier controlled by marine ice sheet instability'. *Nature*, 4(2), 117-121.
- Flament, T. and Rémy, F. (2012) 'Dynamic thinning of Antarctic glaciers from along-track repeat radar altimetry', *Journal of Glaciology*, 58(211), pp. 830–840.
- Fraser, A.D., Massom, R.A., Michael, K.J., Galton-Fenzi, B.K. and Lieser, J.L. (2012) 'East Antarctic Landfast Sea Ice Distribution and Variability, 2000–08', *Journal of Climate*, 25(4), pp. 1137–1156.

- Fretwell, P., Pritchard, H.D., Vaughan, D.G., Bamber, J.L., Barrand, N.E., Bell, R., Bianchi, C., Bingham, R.G., Blankenship, D.D., Casassa, G., Catania, G., Callens, D., Conway, H., Cook, A.J., Corr, H.F.J., Damaske, D., Damm, V., Ferraccioli, F., Forsberg, R., Fujita, S., Gim, Y., Gogineni, P., Griggs, P., Hindmarsh, R.C.A., Holmund, P., Holt, J.W., Jacobel, R.W., Jenkins, A., Jokat, W., Jordan, T., King, E.C., Kohler, J., Krabill, W., Riger-Kusk, M., Langle, K.A., Leitchenkov, G., Leuschen, C., Luyendyk, B.P., Matsuoka, K., Mouginit, J., Nitsche, F.O., Nogi, Y., Nost, O.A., Popov, S.V., Rignot, E., Rippin, D.M., Rivera, A., Roberts, J., Ross, N., Siegert, M.J., Smith, A.M., Steinhage, D., Studinger, M., Sun, B., Tinto, B.K., Wlech, B.C., Wilson, D., Young, D.A., Xiangbin, C. and Zirizzotti, A. (2013) 'Bedmap2: Improved ice bed, surface and thickness datasets for Antarctica'. *The Cryosphere*, 7(1), 375-393.
- Frezzotti, M. and Mabin, M.C.G. (1994) '20th century behaviour of Drygalski Ice Tongue, Ross Sea, Antarctica', *Annals of Glaciology*, 20, pp. 397-400.
- Frezzotti, M., Cimbelli, A. and Ferrigno, J.G. (1998) 'Ice-front change and iceberg behaviour along Oates and George V Coasts, Antarctica, 1912-96'. *Annals of Glaciology*, 27, 643-650.
- Frezzotti, M., Cimbelli, A. and Ferrigno, J.G. (1998) 'Ice-front change and iceberg behaviour along Oates and George V Coasts, Antarctica, 1912-96', *Annals of Glaciology*, 27, pp. 643-650.
- Fukuda, T., Sugiyama, S., Sawagaki, T. and Nakamura, K. (2014) 'Recent variations in the terminus position, ice velocity and surface elevation of Langhovde Glacier, East Antarctica', *Antarctic Science*, 26(6), pp. 636-645.
- Fürst, J.J., Durand, G., Gillet-Chaulet, F., Tavad, L., Rankl, M., Braun, M. and Gagliardini, O. (2016) 'The safety band of Antarctic ice shelves', *Nature Climate Change*, 6(5), pp. 479-482.
- Giles, A.B. (2017) 'The Mertz Glacier Tongue, East Antarctica. Changes in the past 100 years and its cyclic nature - Past, present and future', *Remote Sensing of Environment*, 191, pp. 30-37.
- Giles, A.B., Massom, R.A. and Lytle, V.I. (2008) 'Fast-ice distribution in East Antarctica during 1997 and 1999 determined using RADARSAT data', *Journal of Geophysical Research: Oceans*, 113(C2).
- Giles, A.B., Massom, R.A. and Warner, R.C. (2009) 'A method for sub-pixel scale feature-tracking using Radarsat images applied to the Mertz Glacier Tongue, East Antarctica', *Remote Sensing of Environment*, 113(8), pp. 1691-1699.
- Glasser, N.F. and Gudmundsson, G.H. (2012) 'Longitudinal surface structures (flowstripes) on Antarctic glaciers', *The Cryosphere*, 6(2), pp. 383-391.
- Glasser, N.F. and Scambos, T.A. (2008) 'A structural glaciological analysis of the 2002 Larsen B ice-shelf collapse', *Journal of Glaciology*, 54(184), pp. 3-16.
- Glasser, N.F., Scambos, T.A., Bohlander, J., Truffer, M., Pettit, E. and Davies, B.J. (2011) 'From ice-shelf tributary to tidewater glacier: continued rapid recession, acceleration and thinning of Röhss Glacier following the 1995 collapse of the Prince Gustav Ice Shelf, Antarctic Peninsula', *Journal of Glaciology*, 57(203), pp. 397-406.
- Golledge, N.R., Kowalewski, D.E., Naish, T.R., Levy, R.H., Fogwill, C.J. and Gasson, E.G.W. (2015) 'The multi-millennial Antarctic commitment to future sea-level rise', *Nature*, 526(7573), pp. 421-425.
- Golledge, N.R., Levy, R.H., McKay, R.M. and Naish, T.R. (2017) 'East Antarctic ice sheet most vulnerable to Weddell Sea warming', *Geophysical Research Letters*, 44(5), pp. 2343-2351.

- Greenbaum, J.S., Blankenship, Young, D.A., Richter, T.G., Roberts, J.L., Aitken, A.R.A., Legresy, B., Schröder, D.M., Warner, R.C., Van Ommen, T.D., Siegert, M.J. (2015) 'Ocean access to a cavity beneath Totten Glacier in East Antarctica'. *Nature*, 8, 294-298.
- Gudmundsson, G.H., Rydt, J.D. and Nagler, T. (2017) 'Five decades of strong temporal variability in the flow of Brunt Ice Shelf, Antarctica', *Journal of Glaciology*, 63(237), pp. 164–175.
- Gwyther, D., Galton-Fenzi, B., Hunter, J., Roberts, J. (2014) 'Simulated melt rates for the Totten and Dalton ice shelves'. *Ocean Science*, 10(3), 267-279.
- Gwyther, D.E., O'Kane, T.J., Galton-Fenzi, B.K., Monselesan, D.P. and Greenbaum, J.S. (2018) 'Intrinsic processes drive variability in basal melting of the Totten Glacier Ice Shelf', *Nature Communications*, 9(1), p. 3141
- Hanna, E., Navarro, F.J., Pattyn, F., Domingues, C.M., Fettweis, X., Ivins, E.R., Nicholls, R.J., Ritz, C., Smith, B., Tulaczyk, S., Whitehouse, P.L. and Zwally, H.J. (2013) 'Ice-sheet mass balance and climate change', *Nature*, 498(7452), pp. 51–59.
- Hill, E.A., Gudmundsson, G.H., Carr, J.R., Stokes, C.R. and King, H.M. (2021) 'Twenty-first century response of Petermann Glacier, northwest Greenland to ice shelf loss', *Journal of Glaciology*, 67(261), pp. 147–157.
- Hogg, A.E. and Gudmundsson, G.H. (2017) 'Impacts of the Larsen-C Ice Shelf calving event', *Nature Climate Change*, 7(8), pp. 540–542.
- Holt, T.O., Glasser, N.F., Quincey, D.J. and Siegfried, M.R. (2013) 'Speedup and fracturing of George VI Ice Shelf, Antarctic Peninsula', *The Cryosphere*, 7(3), pp. 797–816.
- Holt, T. and Glasser, N.F. (2022) 'Changes in area, flow speed and structure of southwest Antarctic Peninsula ice shelves in the 21st century', *Journal of Glaciology*, pp. 1–19.
- Howat, I.M., Porter, C., Smith, B.E., Noh, M.-J. and Morin, P. (2019) 'The Reference Elevation Model of Antarctica', *The Cryosphere*, 13(2), pp. 665–674.
- Indrigo, C., Dow, C.F., Greenbaum, J.S. and Morlighem, M. (2021) 'Drygalski Ice Tongue stability influenced by rift formation and ice morphology', *Journal of Glaciology*, 67(262), pp. 243–252.
- Jacobs, S.S., Jenkins, A., Giulivi, C.F. and Dutrieux, P. (2011) 'Stronger ocean circulation and increased melting under Pine Island Glacier ice shelf', *Nature Geoscience*, 4(8), pp. 519–523.
- Jennings, S.J.A. and Hambrey, M.J. (2021) 'Structures and Deformation in Glaciers and Ice Sheets', *Reviews of Geophysics*, 59(3), p. e2021RG000743.
- Johnson, A., Hock, R. and Fahnestock, M. (2021) 'Spatial variability and regional trends of Antarctic ice shelf surface melt duration over 1979–2020 derived from passive microwave data', *Journal of Glaciology*, pp. 1–14.
- Joughin, I., Smith, B.E. and Medley, B. (2014) 'Marine Ice Sheet Collapse Potentially Under Way for the Thwaites Glacier Basin, West Antarctica', *Science*, 344(6185), pp. 735–738.
- Khazendar, A., Rignot, E. and Larour, E. (2009) 'Roles of marine ice, rheology, and fracture in the flow and stability of the Brunt/Stancomb-Wills Ice Shelf', *Journal of Geophysical Research: Earth Surface*, 114(F4).

- King, M.A., Bingham, R.J., Moore, P., Whitehouse, P.L., Bentley, M.J. and Milne, G.A. (2012) 'Lower satellite-gravimetry estimates of Antarctic sea-level contribution', *Nature*, 491(7425), pp. 586–589.
- King, M.A., Murray, T. and Smith, A.M. (2010) 'Non-linear responses of Rutford Ice Stream, Antarctica, to semi-diurnal and diurnal tidal forcing', *Journal of Glaciology*, 56(195), pp. 167–176.
- Kingslake, J., Ely, J.C., Das, I. and Bell, R.E. (2017) 'Widespread movement of meltwater onto and across Antarctic ice shelves', *Nature*, 544(7650), pp. 349–352.
- Köhl, A. (2020) 'Evaluating the GECCO3 1948–2018 ocean synthesis – a configuration for initializing the MPI-ESM climate model', *Quarterly Journal of the Royal Meteorological Society*, 146(730), pp. 2250–2273.
- Konrad, H., Shepherd, A., Gilbert, L., Hogg, A.E., McMillan, M., Muir, A. and Slater, T. (2018) 'Net retreat of Antarctic glacier grounding lines', *Nature Geoscience*, 11(4), pp. 258–262.
- Kusahara, K., Hasumi, H. and Williams, G.D. (2011) 'Impact of the Mertz Glacier Tongue calving on dense water formation and export', *Nature Communications*, 2(1), p. 159.
- Langley, E.S., Leeson, A.A., Stokes, C.R. and Jamieson, S.S.R. (2016) 'Seasonal evolution of supraglacial lakes on an East Antarctic outlet glacier', *Geophysical Research Letters*, 43(16), pp. 8563–8571.
- Lea, J.M. (2018) 'The Google Earth Engine Digitisation Tool (GEEDiT) and the Margin change Quantification Tool (MaQiT) – simple tools for the rapid mapping and quantification of changing Earth surface margins', *Earth Surface Dynamics*, 6(3), pp. 551–561.
- Legresy, B., Wendt, A., Tabacco, I.E., Remy, F. and Dietrich, R. (2004) 'Influence of tides and tidal current on Mertz Glacier, Antarctica'. *Journal of Glaciology*, 50(170), pp. 427–435.
- Lenaerts, J.T.M., Lhermitte, S., Drews, R., Ligtenberg, S.R.M., Berger, S., Helm, V., Smeets, C.J.P.P., Broeke, M.R. van den, van de Berg, W.J., van Meijgaard, E., Eijkelboom, M., Eisen, O. and Pattyn, F. (2017) 'Meltwater produced by wind–albedo interaction stored in an East Antarctic ice shelf', *Nature Climate Change*, 7(1), pp. 58–62.
- Lescarmontier, L., Legresy, B., Young, N.W., Coleman, R., Testut, L., Mayet, C. and Lacroix, P. (2015) 'Rifting processes and ice-flow modulation observed on Mertz Glacier, East Antarctica', *Journal of Glaciology*, 61(230), pp. 1183–1193.
- Lhermitte, S., Sun, S., Shuman, C., Wouters, B., Pattyn, F., Wuite, J., Berthier, E. and Nagler, T. (2020) 'Damage accelerates ice shelf instability and mass loss in Amundsen Sea Embayment', *Proceedings of the National Academy of Sciences*, 117(40), pp. 24735–24741.
- Li, X., Rignot, E., Morlighem, M., Mougintot, J. and Scheuchl, B. (2015) 'Grounding line retreat of Totten Glacier, East Antarctica, 1996 to 2013', *Geophysical Research Letters*, 42(19), pp. 8049–8056.
- Lovell, A.M., Stokes, C.R. and Jamieson, S.S.R. (2017) 'Sub-decadal variations in outlet glacier terminus positions in Victoria Land, Oates Land and George V Land, East Antarctica (1972–2013)'. *Antarctic Science*, 29(5), pp.468–483, 468–483.
- Martin-Español, A., Bamber, J.L. and Zammit-Mangion, A. (2017) 'Constraining the mass balance of East Antarctica'. *Geophysical Research Letters*, 44(9), 4168–4175.

- Martín-Español, A., Zammit-Mangion, A., Clarke, P.J., Flament, T., Helm, V., King, M.A., Luthcke, S.B., Petrie, E., Rémy, F., Schön, N., Wouters, B. and Bamber, J.L. (2016) 'Spatial and temporal Antarctic Ice Sheet mass trends, glacio-isostatic adjustment, and surface processes from a joint inversion of satellite altimeter, gravity, and GPS data', *Journal of Geophysical Research: Earth Surface*, 121(2), pp. 182–200.
- Massom, R. (2003). 'Recent iceberg calving events in the Ninnis Glacier region, East Antarctica'. *Antarctic Science*, 15(2), 303-313.
- Massom, R.A. (2003) 'Recent iceberg calving events in the Ninnis Glacier region, East Antarctica', *Antarctic Science*, 15(2), pp. 303–313.
- Massom, R.A., Giles, A.B., Fricker, H.A., Warner, R.C., Legrésy, B., Hyland, G., Young, N. and Fraser, A.D. (2010) 'Examining the interaction between multi-year landfast sea ice and the Mertz Glacier Tongue, East Antarctica: Another factor in ice sheet stability?', *Journal of Geophysical Research: Oceans*, 115(C12).
- Massom, R.A., Giles, A.B., Warner, R.C., Fricker, H.A., Legrésy, B., Hyland, G., Lescarmontier, L. and Young, N. (2015a) 'External influences on the Mertz Glacier Tongue (East Antarctica) in the decade leading up to its calving in 2010', *Journal of Geophysical Research: Earth Surface*, 120(3), pp. 490–506.
- Massom, R.A., Giles, A.B., Warner, R.C., Fricker, H.A., Legrésy, B., Hyland, G., Lescarmontier, L. and Young, N. (2015b) 'External influences on the Mertz Glacier Tongue (East Antarctica) in the decade leading up to its calving in 2010', *Journal of Geophysical Research: Earth Surface*, 120(3), pp. 490–506.
- Massom, R.A., Hill, K.L., Lytle, V.I., Worby, A.P., Paget, M.J. and Allison, I. (2001) 'Effects of regional fast-ice and iceberg distributions on the behaviour of the Mertz Glacier polynya, East Antarctica', *Annals of Glaciology*, 33, pp. 391–398.
- Massom, R.A., Scambos, T.A., Bennetts, L.G., Reid, P., Squire, V.A. and Stammerjohn, S.E. (2018) 'Antarctic ice shelf disintegration triggered by sea ice loss and ocean swell', *Nature*, 558(7710), pp. 383–389.
- Matsuoka, K., Hindmarsh, R.C.A., Moholdt, G., Bentley, M.J., Pritchard, H.D., Brown, J., Conway, H., Drews, R., Durand, G., Goldberg, D., Hattermann, T., Kingslake, J., Lenaerts, J.T.M., Martín, C., Mulvaney, R., Nicholls, K.W., Pattyn, F., Ross, N., Scambos, T. and Whitehouse, P.L. (2015) 'Antarctic ice rises and rumples: Their properties and significance for ice-sheet dynamics and evolution', *Earth-Science Reviews*, 150, pp. 724–745.
- McMillan, M., Shepherd, A., Sundal, A., Briggs, K., Muir, A., Ridout, A., Hogg, A. and Wingham, D. (2014) 'Increased ice losses from Antarctica detected by CryoSat-2'. *Geophysical Research Letters*, 41(11), 3899-3905.
- Mengel, M., Levermann, A. (2014) 'Ice plug prevents irreversible discharge from East Antarctica'. *Nature*, 4(6), 451-455.
- Meredith, M., Sommerkorn, M., Cassota, S., Derksen, C., Ekaykin, A., Hollowed, A., Kofinas, G., Mackintosh, A., Melbourne-Thomas, J., Muelber, M.M.C., Ottersen, G., Pritchard, H. and Schuur, E.A.G. (2019) Polar Regions. In: Pörtner, H.O., Roberts, D.C., Masson-Delmotte, V., Zhai, P., Tignor, M., Poloczanska, E., Mintenbeck, K., Alegría, A., Nicolai, M., Okem, A., Petzold, J., Rama, B., Weyer, N.M. (eds) *IPCC Special Report on the Ocean and Cryosphere in a Changing Climate*. In press, pp.203-320.

- Miles, B.W.J., Jordan, J.R., Stokes, C.R., Jamieson, S.S.R., Gudmundsson, G.H. and Jenkins, A. (2021) 'Recent acceleration of Denman Glacier (1972–2017), East Antarctica, driven by grounding line retreat and changes in ice tongue configuration', *The Cryosphere*, 15(2), pp. 663–676.
- Miles, B.W.J., Stokes, C.R. and Jamieson, S.S.R (2017) 'Simultaneous disintegration of outlet glaciers in Porpoise Bay (Wilkes Land), East Antarctica, driven by sea ice break-up'. *The Cryosphere*, 11, pp.427-442.
- Miles, B.W.J., Stokes, C.R. and Jamieson, S.S.R. (2016) 'Pan-ice sheet glacier terminus change in East Antarctica reveals sensitivity of Wilkes Land to sea-ice changes'. *Science Advances*, 2(5), pp.1-7.
- Miles, B.W.J., Stokes, C.R. and Jamieson, S.S.R. (2018) 'Velocity increases at Cook Glacier, East Antarctica, linked to ice shelf loss and a subglacial flood event'. *The Cryosphere*, 12, pp.3123-3136.
- Miles, B.W.J., Stokes, C.R., Jenkins, A., Jordan, J.R., Jamieson, S.S.R. and Gudmundsson, G.H. (2020) 'Intermittent structural weakening and acceleration of the Thwaites Glacier Tongue between 2000 and 2018', *Journal of Glaciology*, 66(257), pp. 485–495.
- Miles, B.W.J., Stokes, C.R., Vieli, A. and Cox N.J. (2013) 'Rapid, climate-driven changes in outlet glaciers on the Pacific coast of East Antarctica'. *Nature*, 500, pp.563-567.
- Milillo, P., Rignot, E., Rizzoli, P., Scheuchl, B., Mouginot, J., Bueso-Bello, J. and Prats-Iraola, P. (no date) 'Heterogeneous retreat and ice melt of Thwaites Glacier, West Antarctica', *Science Advances*, 5(1), p. eaau3433.
- Moon, T. and Joughin, I. (2008) 'Changes in ice front position on Greenland's outlet glaciers from 1992 to 2007', *Journal of Geophysical Research: Earth Surface*, 113(F2).
- Morlighem, M., Rignot, E., Binder, T., Blankenship, D., Drews, R., Eagles, G., Eisen, O., Ferraccioli, D., Forsberg, R., Fretwell, P., Goel, V., Greenbaum, J., Gudmundsson, H., Guo, J., Helm, V., Hofstede, C., Howat, I., Humbert, A., Jokat, W. (2020) 'Deep glacial troughs and stabilizing ridges unveiled beneath the margins of the Antarctic ice sheet' *Nature*, 13(2), 132-137.
- Mouginot, J., Rignot, E. and Scheuchl, B. (2014) 'Sustained increase in ice discharge from the Amundsen Sea Embayment, West Antarctica, from 1973 to 2013', *Geophysical Research Letters*, 41(5), pp. 1576–1584.
- Mouginot, J., Rignot, E., Scheuchl, B. (2014) 'Sustained increase in ice discharge from the Amundsen Sea Embayment, West Antarctica from 1973-2013'. *Geophysical Research Letters*, 41(5), 1576-1584.
- Mouginot, J., Rignot, E., Scheuchl, B. and Millan, R. (2017) 'Comprehensive Annual Ice Sheet Velocity Mapping Using Landsat-8, Sentinel-1, and RADARSAT-2 Data', *Remote Sensing*, 9(4), p. 364.
- Parkinson, C.L. and Cavalieri, D.J. (2012) 'Antarctic sea ice variability and trends, 1979-2010', *The Cryosphere*, 6(4), pp. 871–880.
- Pattyn, F. (2018) 'The paradigm shift in Antarctic ice sheet modelling' *Nature Communications*, 9(1), 1-3.

- Pattyn, F. and Morlighem, M. (2020) 'The uncertain future of the Antarctic Ice Sheet' *Science*, 367(6484), 1331-1335.
- Pritchard, H.D., Arthern, R.J., Vaughan, D.G. Edwards, L.A. (2009) 'Extensive dynamic thinning of the Greenland and Antarctic ice sheets'. *Nature*, 461(7266), 971-975.
- Pritchard, H.D., Ligtenberg, S.R.M., Fricker, H.A., Vaughan, D.G., van Den Broeke, M.R. and Padman, L. (2012) 'Antarctic ice-sheet loss driven by basal melting of ice shelves'. *Nature*, 484(7395), 502-505.
- Reese, R., Gudmundsson, G.H., Levermann, A. and Winkelmann, R. (2018) 'The far reach of ice-shelf thinning in Antarctica', *Nature Climate Change*, 8(1), pp. 53–57.
- Rignot, E., Mouginot, J., Scheuchl, B., van den Broeke., van Wessem, M.J. and Morlighem, M. (2019) 'Four decades of Antarctic Ice Sheet Mass Balance from 1979-2017'. *Proceeds of the National Academy of Sciences*, 116(4), pp.1095-1103.
- Rignot, E. (2002) 'Mass balance of East Antarctic glaciers and ice shelves from satellite data', *Annals of Glaciology*, 34, pp. 217–227.
- Rignot, E. (2006) 'Changes in ice dynamics and mass balance of the Antarctic ice sheet', *Philosophical Transactions of the Royal Society A: Mathematical, Physical and Engineering Sciences*, 364(1844), pp. 1637–1655.
- Rignot, E., Bamber, J.L., van den Broeke, M.R., Davis, C., Li, Y., van de Berg, W.J. and van Meijgaard, E. (2008) 'Recent Antarctic ice mass loss from radar interferometry and regional climate modelling', *Nature Geoscience*, 1(2), pp. 106–110.
- Rignot, E., Box, J.E., Burgess, E., Hanna, E. (2008) ' Mass balance of the Greenland ice sheet from 1958 to 2007'. *Geophysical Research Letters*, 35(20) na-na.
- Rignot, E., Casassa, G., Gogineni, P., Krabill, W., Rivera, A. and Thomas, R. (2004) 'Accelerated ice discharge from the Antarctic Peninsula following the collapse of Larsen B ice shelf', *Geophysical Research Letters*, 31(18).
- Rignot, E., Mouginot, J., Morlighem, M., Seroussi, H. and Scheuchl, B. (2014) 'Widespread, rapid grounding line retreat of Pine Island, Thwaites, Smith, and Kohler glaciers, West Antarctica, from 1992 to 2011', *Geophysical Research Letters*, 41(10), pp. 3502–3509.
- Rignot, E., Mouginot, J., Scheuchl, B. (2011) 'Ice Flow of the Antarctic Ice Sheet'. *Science*, 333(6048), 1427-1430.
- Rintoul, S.R., Silvano, A., Pena-Molino, B., van Wijk, E., Rosenberg, M., Greenbaum, J.S. and Blankenship, D.D. (no date) 'Ocean heat drives rapid basal melt of the Totten Ice Shelf', *Science Advances*, 2(12), p. e1601610.
- Rolstad, C., Whillans, I.M., Hagen, J.O. and Isaksson, E. (2000) 'Large-scale force budget of an outlet glacier: Jutulstraumen, Dronning Maud Land, East Antarctica', *Annals of Glaciology*, 30, pp. 35–41.
- Rott, H., Skvarca, P. and Nagler, T. (1996) 'Rapid Collapse of Northern Larsen Ice Shelf, Antarctica', *Science*, 271(5250), pp. 788–792.
- Sergienko, O.V. and Wingham, D.J. (2019) 'Grounding line stability in a regime of low driving and basal stresses', *Journal of Glaciology*, 65(253), pp. 833–849.

- Scambos, T., Fricker, H.A., Liu, C.-C., Bohlander, J., Fastook, J., Sargent, A., Massom, R. and Wu, A.-M. (2009) 'Ice shelf disintegration by plate bending and hydro-fracture: Satellite observations and model results of the 2008 Wilkins ice shelf break-ups', *Earth and Planetary Science Letters*, 280(1), pp. 51–60.
- Scambos, T.A., Bohlander, J.A., Shuman, C.A. and Skvarca, P. (2004) 'Glacier acceleration and thinning after ice shelf collapse in the Larsen B embayment, Antarctica', *Geophysical Research Letters*, 31(18).
- Schlemm, T. and Levermann, A. (2021) 'A simple parametrization of mélange buttressing for calving glaciers', *The Cryosphere*, 15(2), pp. 531–545.
- Schoof, C. (2007) 'Marine ice-sheet dynamics. Part1. The case of rapid sliding'. *Journal of Fluid Mechanics*, 573, 27-55
- Schröder, L., Horwath, M., Dietrich, R., Helm, V., Ligtenberg, S. (2019) 'Four decades of Antarctica surface elevation changes from multi-mission satellite altimetry'. *The Cryosphere*, 13(2), 427-449.
- Schröder, L., Horwath, M., Dietrich, R., Helm, V., van den Broeke, M.R. and Ligtenberg, S.R.M. (2019) 'Four decades of Antarctic surface elevation changes from multi-mission satellite altimetry', *The Cryosphere*, 13(2), pp. 427–449.
- Seroussi, H., Nakayama, Y., Larour, E., Menemenlis, D., Morlighem, M., Rignot, E. and Khazendar, A. (2017) 'Continued retreat of Thwaites Glacier, West Antarctica, controlled by bed topography and ocean circulation', *Geophysical Research Letters*, 44(12), pp. 6191–6199.
- Shepherd, A., Ivins, E., Rignot, E., Smith, B., van den Broeke, M., The IMBIE team, *et al.* (2018) 'Mass balance of the Antarctic Ice Sheet from 1992 to 2017', *Nature*, 558(7709), pp. 219–222.
- Shepherd, A., Ivins, E.R., Geruo, A., Barletta, V.R., Bentley, M.J., Bettadpur, S., Briggs, K.H., Bromwich, D.H., Forsberg, R., Galin, N., Horwath, M., Jacobs, S., Joughin, I., King, M.A., Lenaerts, J.T.M., Li, J., Lightenberg, S.R.M., Luckman, A., Luthcke, S.B., McMillan, M., Meister, R., Milne, G., Mouginot, J., Muir, A., Nicolas, J.P., Paden, J., Payne, A.J., Pritchard, H., Rignot, E., Rott, H., Sandberg Sørensen, L., Scambos, T.A., Scheuchl, B., Schrama, E.J.O., Smith, B., Sundal, A.V., van Angelen, J.H., van de Berg, W.J., van den Broeke, M.R., Vaughan, D.G., Velicogna, I., Wahr, J., Whitehouse, P.L., Wingham, D.J., Yi, D., Young, D. and Zwally, J.H. (2012) 'A Reconciled Estimate of Ice-Sheet Mass Balance', *Science*, 338(6111), pp.1182-1189.
- Siegert, M., Atkinson, A., Banwell, A., Brandon, M., Convey, P., Davies, B., Downie, R., Edwards, T., Hubbard, B., Marshall, G., Rogelj, J., Rumble, J., Stroeve, J. and Vaughan, D. (2019) 'The Antarctic Peninsula Under a 1.5°C Global Warming Scenario', *Frontiers in Environmental Science*, 7(102).
- Smith, B., Fricker, H.A., Gardner, A.L., Medley, B., Nilsson, J., Paolo, F.S., Holschuh, N., Adusimilli, S., Brunt, K., Csatho, B., Harbeck, K., Markus, T., Neumann, T., Siegfried, M.R. and Zwally, J.H. (2020) 'Pervasive ice sheet mass loss reflects competing ocean and atmosphere processes'. *Science*, 368(6496), 1239-1242.
- Spence, P., Griffies, S.M., England, M.H., Hogg, A.McC., Saenko, O.A. and Jourdain, N.C. (2014) 'Rapid subsurface warming and circulation changes of Antarctic coastal waters by poleward shifting winds', *Geophysical Research Letters*, 41(13), pp. 4601–4610.

- Spergel, J.J., Kingslake, J., Creyts, T., Wessem, M. van and Fricker, H.A. (2021) 'Surface meltwater drainage and ponding on Amery Ice Shelf, East Antarctica, 1973–2019', *Journal of Glaciology*, 67(266), pp. 985–998.
- Stearns, L.A., Smith, B.E. and Hamilton, G.S. (2008) 'Increased flow speed on a large East Antarctic outlet glacier caused by subglacial floods'. *Nature*, 1, pp. 827–831.
- Steig, E.J., Ding, Q., Battisti, D.S. and Jenkins, A. (2012) 'Tropical forcing of Circumpolar Deep Water Inflow and outlet glacier thinning in the Amundsen Sea Embayment, West Antarctica', *Annals of Glaciology*, 53(60), pp. 19–28.
- Stewart, A.L. and Thompson, A.F. (2015) 'Eddy-mediated transport of warm Circumpolar Deep Water across the Antarctic Shelf Break', *Geophysical Research Letters*, 42(2), pp. 432–440.
- Stokes, C.R., Gurney, S.D., Shahgedanova, M. and Popovnin, V. (2006) 'Late-20th-century changes in glacier extent in the Caucasus Mountains, Russia/Georgia', *Journal of Glaciology*, 52(176), pp. 99–109.
- Stokes, C.R., Sanderson, J.E., Miles, B.W.J., Jamieson, S.S.R. and Leeson, A.A. (2019) 'Widespread distribution of supraglacial lakes around the margin of the East Antarctic Ice Sheet', *Scientific Reports*, 9(1), p. 13823.
- Stroeve, J. and Notz, D. (2018) 'Changing state of Arctic sea ice across all seasons', *Environmental Research Letters*, 13(10), p. 103001.
- Sutter, J., Eisen, O., Werner, M., Grosfeld, K., Kleiner, T. and Fischer, H. (2020) 'Limited Retreat of the Wilkes Basin Ice Sheet During the Last Interglacial', *Geophysical Research Letters*, 47(13), p. e2020GL088131.
- Tamura, T., Ohshima, K.I. and Nihashi, S. (2008) 'Mapping of sea ice production for Antarctic coastal polynyas', *Geophysical Research Letters*, 35(7).
- Trusel, L.D., Frey, K.E., Das, S.B., Munneke, P.K. and van den Broeke, M.R. (2013) 'Satellite-based estimates of Antarctic surface meltwater fluxes', *Geophysical Research Letters*, 40(23), pp. 6148–6153.
- Tuckett, P.A., Ely, J.C., Sole, A.J., Livingstone, S.J., Davison, B.J., Melchior van Wessem, J. and Howard, J. (2019) 'Rapid accelerations of Antarctic Peninsula outlet glaciers driven by surface melt', *Nature Communications*, 10(1), p. 4311.
- Turton, J.V., Kirchgaessner, A., Ross, A.N. and King, J.C. (2018) 'The spatial distribution and temporal variability of föhn winds over the Larsen C ice shelf, Antarctica', *Quarterly Journal of the Royal Meteorological Society*, 144(713), pp. 1169–1178.
- USGS, 2013. SLC-off products: Background. http://landsat.usgs.gov/products_slcutoffbackground.php.
- Velicogna, I., Sutterley, T.C. and van den Broeke, M.R. (2014) 'Regional acceleration in ice mass loss from Greenland and Antarctica using GRACE time-variable gravity data', *Geophysical Research Letters*, 41(22), pp. 8130–8137.
- Vieli, A., Payne, A.J., Shepherd, A. and Du, Z. (2007) 'Causes of pre-collapse changes of the Larsen B ice shelf: Numerical modelling and assimilation of satellite observations', *Earth and Planetary Science Letters*, 259(3), pp. 297–306.

- Walker, D.P., Brandon, M.A., Jenkins, A., Allen, J.T., Dowdeswell, J.A. and Evans, J. (2007) 'Oceanic heat transport onto the Amundsen Sea shelf through a submarine glacial trough', *Geophysical Research Letters*, 34(2).
- Wang, Y., Ding, M., Wessem, J.M. van, Schlosser, E., Altnau, S., Broeke, M.R. van den, Lenaerts, J.T.M., Thomas, E.R., Isaksson, E., Wang, J. and Sun, W. (2016) 'A Comparison of Antarctic Ice Sheet Surface Mass Balance from Atmospheric Climate Models and In Situ Observations', *Journal of Climate*, 29(14), pp. 5317–5337.
- Weertman, J. (1974). 'Stability of the Junction of an Ice Sheet and an Ice Shelf'. *Journal of Glaciology*, 13 (67), 3-11.
- Wendler, G., Ahlnäs, K. and Lingle, C.S. (1996) 'On Mertz and Ninnis Glaciers, East Antarctica', *Journal of Glaciology*, 42(142), pp. 447–453.
- Wendler, G., Ahlnäs, K., & Lingle, C. (1996). 'On Mertz and Ninnis Glaciers, East Antarctica'. *Journal of Glaciology*, 42 (142), 447-453.
- Wilson, D.J., Bertram, R.A., Needham, E.F., van de Fliedrt, T., Welsh, K.J., McKay, R.M., Mazumder, A., Riesselman, C.R., Jimenez-Espejo, F.J. and Escutia, C. (2018) 'Ice loss from the East Antarctic Ice Sheet during late Pleistocene interglacials', *Nature*, 561(7723), pp. 383–386.
- Winter, K., Hill, E.A., Gudmundsson, G.H. and Woodward, J. (2020) 'Subglacial topography and ice flux along the English Coast of Palmer Land, Antarctic Peninsula', *Earth System Science Data*, 12(4), pp. 3453–3467.
- Yoon, S.-T., Lee, W.S., Stevens, C., Jendersie, S., Nam, S., Yun, S., Hwang, C.Y., Jang, G.I. and Lee, J. (2020) 'Variability in high-salinity shelf water production in the Terra Nova Bay polynya, Antarctica', *Ocean Science*, 16(2), pp. 373–388.
- Young, D.A., Wright, A.P., Roberts, J.L., Warner, R.C., Young, N.W., Greenbaum, J.S., Schroeder, D.M., Holt, J.W., Sugden, D.E., Blankenship, D.D., van Ommen, T.D. and Siegert, M.J. (2011) 'A dynamic early East Antarctic Ice Sheet suggested by ice-covered fjord landscapes', *Nature*, 474(7349), pp. 72–75.
- Zwally, H.J., Giovinetto, M.B., Li, J., Cornejo, H.G., Beckley, M.A., Brenner, A.C., Saba, J.L. and Yi, D. (2005) 'Mass changes of the Greenland and Antarctic ice sheets and shelves and contributions to sea-level rise: 1992–2002', *Journal of Glaciology*, 51(175), pp. 509–527.
- Zwally, H.J., Li, J., Robbins, J.W., Saba, J.L., Yi, D. and Brenner, A.C. (2015) 'Mass gains of the Antarctic ice sheet exceed losses', *Journal of Glaciology*, 61(230), pp. 1019–1036.

Appendix A: Satellite Image IDs

1) Complete list of all satellite image IDs included in the Ninnis terminus time series.

Argon KH-5:

- DS09059A051MC079_a.TIF (1963).

Landsat 1-5 Multi Spectral Scanner (MSS):

- LM01_L1GS_084108_19740118_20180426_01_T2_B7.TIF (1974).

Soyuz KATE:

- Soyuz-84-1.img

Landsat 4-5 Thematic Mapper (TM):

- LT05_L1GS_080108_19890104_20170204_01_T2_B2.TIF (1989).
- LT05_L1GS_080108_19910315_20170127_01_T2_B1.TIF (1991).

ERS-1 Synthetic Aperture Radar (SAR):

- E1_23836_STD_F625.jpg (1996/02/04)

ERS-2 Synthetic Aperture Radar (SAR):

- E2_16688_STD_F625.jpg (1998/06/29)

RADARSAT Antarctic Mapping Project (RAMP) Mosaic:

- Amm125_v2_200m.tif (1997)

Landsat Image Mosaic Antarctica (LIMA):

- 00000-20080314-144756363.jp2

Landsat 7 Enhanced Thematic Mapper Plus (ETM+):

- LE07_L1GT_079108_20000221_20170213_01_T2_B8.TIF (2000).
- LE07_L1GT_080108_20011113_20170202_01_T2_B8.TIF (2001).
- LE07_L1GT_081108_20021123_20170127_01_T2_B8.TIF (2002).
- LE07_L1GT_080108_20030220_20170126_01_T2_B8.TIF (2003).
- LE07_L1GT_080108_20040207_20170122_01_T2_B8.TIF (2004).
- LE07_L1GT_079108_20061120_20170107_01_T2_B8.TIF (2006).
- LE07_L1GT_080108_20071114_20161231_01_T2_B8.TIF (2007).
- LE07_L1GT_080108_20081116_20161224_01_T2_B8.TIF (2008).
- LE07_L1GT_080108_20090204_20161222_01_T2_B8.TIF (2009).
- LE07_L1GT_080108_20100122_20161215_01_T2_B8.TIF (2010).
- LE07_L1GT_079108_20111102_20161205_01_T2_B8.TIF (2011).
- LE07_L1GT_079108_20120206_20161203_01_T2_B8.TIF (2012).

Landsat 8 Operational Land Imager (OLI):

- LC08_L1GT_079108_20131201_20170428_01_T2_B8.TIF (2013).
- LC08_L1GT_081108_20141202_20170416_01_T2_B8.TIF (2014).
- LC08_L1GT_079108_20151105_20170402_01_T2_B8.TIF (2015).
- LC08_L1GT_081108_20161207_20170317_01_T2_B8.TIF (2016).
- LC08_L1GT_079108_20171212_20171223_01_T2_B8.TIF (2017).
- LC08_L1GT_079108_20181215_20181227_01_T2_B8.TIF (2018).
- LC08_L1GT_080108_20191225_20200110_01_T2_B8.TIF (2019).

Sentinel 2:

- L1C_T55DEE_A019489_20201128T230340.tif (2020).
- L1C_T55DEE_A020004_20210103T232348.tif (2021).

2) Complete list of all Landsat 8 and Sentinel image IDs included in sub-annual terminus mapping.

Landsat 8:

- 2018-01-27: LE07_L1GT_079108_20080126_20161230_01_T2_B8.TIF
- 2018-02-21: LC08_L1GT_080108_20180221_20180308_01_T2_B8.TIF
- 2018-03-09: LC08_L1GT_080108_20180309_20180320_01_T2_B8.TIF
- 2018-11-20: LC08_L1GT_080108_20181120_20181129_01_T2_B8.TIF
- 2018-12-06: LC08_L1GT_080108_20181206_20181211_01_T2_B8.TIF
- 2018-12-15: LC08_L1GT_079108_20181215_20181227_01_T2_B8.TIF
- 2019-02-01: LC08_L1GT_080108_20191225_20200110_01_T2_B8.TIF
- 2019-12-25: LC08_L1GT_080108_20191225_20200110_01_T2_B8.TIF
- 2020-01-17: LC08_L1GT_081108_20200117_20200128_01_T2_B8.TIF
- 2020-02-18: LC08_L1GT_081108_20200218_20200225_01_T2_B8.TIF
- 2020-11-16: LC08_L1GT_081108_20201116_20210315_01_T2_B8.TIF
- 2021-02-06: LC08_L1GT_079108_20210206_20210305_01_T2_B8.TIF
- 2021-03-04: LC08_L1GT_079108_20210326_20210402_01_T2_B8.TIF
- 2021-03-26: LC08_L1GT_079108_20210326_20210402_01_T2_B8.TIF

Sentinel 2:

- 2020-11-28: L1C_T55DEE_A019489_20201128T230340.TIF
- 2021-01-03: L1C_T55DEE_A020004_20210103T232348.TIF
- 2021-01-13: L1C_T55DEE_A020147_20210113T232349.TIF
- 2021-01-23: L1C_T55DEE_A020290_20210123T232349.TIF

3) Complete list of all Landsat 8 image IDs included in Ninnis structural mapping.

- LC08_L1GT_080108_20160131_20180202_01_T2_B8.TIF (2016).
- LC08_L1GT_079108_20171212_20171223_01_T2_B8.TIF (2017).
- LC08_L1GT_081108_20180127_20180207_01_T2_B8.TIF (2018).
- LC08_L1GT_080108_20191225_20200110_01_T2_B8.TIF (2019).

- LC08_L1GT_081108_20201116_20210315_01_T2_B8.TIF (2020).
- LC08_L1GT_079108_20210326_20210402_01_T2_B8.TIF (2021).

4) Complete list of all Landsat 8 and Sentinel 2 image IDs included in rift mapping (2016-2017).

Sentinel 2:

- L1C_T55DEE_A009164_2017-324T230334.TIF (March 2017).

Landsat 8:

- LC08_L1GT_080108_20160131_20180202_01_T2_B8.TIF (January 2016).
- LC08_L1GT_081108_20161207_20170317_01_T2_B8.TIF (December 2016).
- LC08_L1GT_081108_20170108_20170311_01_T2_B8.TIF (January 2017)
- LC08_L1GT_079108_20171212_20171223_01_T2_B8.TIF (December 2017)

5) Complete list of all Landsat 7 Enhanced Thematic Mapper Plus (ETM+) used to visualise the 2007-2008 minor calving event at Ninnis Glacier.

- LE07_L1GT_080108_20040207_20170122_01_T2_B8.TIF (2004).
- LE07_L1GT_081108_20070105_20170101_01_T2_B8.TIF (2007).
- LE07_L1GT_079108_20080126_20161230_01_T2_B8.TIF (2008).